Research Square

Preprints are preliminary reports that have not undergone peer review. They should not be considered conclusive, used to inform clinical practice, or referenced by the media as validated information.

A Novel ACLY Inhibitor Induces Transcriptional and Metabolic Reprogramming to Overcome Tyrosine kinase inhibitor Resistance in Lymphoma

Nagarajan Pattabiraman
Veracure Biosciences Inc
Cosimo Lobello
Fox Chase Cancer Center
David Rushmore
Fox Chase Cancer Center
Shengchun Wang
Fox Chase Cancer Center
Luca Mologni
University of Milano-Bicocca
Hossein Borghaei
Fox Chase Cancer Center
Kavindra Nath
University of Pennsylvania
Wujuan Zhang
The Wistar Institute
Aaron R. Goldman
The Wistar Institute
Reza Nejati
Fox Chase Cancer Center
Mariusz Wasik
Fox Chase Cancer Center
Johnvesly Basappa
Johnvesly.Basappa@fccc.edu

Fox Chase Cancer Center

Research Article

Keywords: ACLY, tyrosine phosphorylation, lipid metabolism, drug discovery

Posted Date: October 20th, 2026

DOI: https://doi.org/10.21203/rs.3.rs-11120406/v1

License: This work is licensed under a Creative Commons Attribution 4.0 International License.
Read Full License

Additional Declarations: No competing interests reported.

A Novel ACLY Inhibitor Induces Transcriptional and Metabolic Reprogramming to Overcome Tyrosine kinase inhibitor Resistance in Lymphoma

Nagarajan Pattabiraman[1], Cosimo Lobello[2], David Rushmore[2], Shengchun Wang[2], Luca Mologni[3], Hossein Borghaei[2], Kavindra Nath[5], Wujuan Zhang[4], Aaron R. Goldman[4], Reza Nejati[2], Mariusz Wasik[2] and Johnvesly Basappa[2*]

[1]Veracure Biosciences Inc., Gaithersburg, MD

[2]Fox Chase Cancer Center, Philadelphia, PA, USA

[3]Department of Medicine and Surgery, University of Milano-Bicocca, Monza, Italy

[4]Proteomics & Metabolomics Shared Resource, The Wistar Institute, Philadelphia, PA, USA

[5]Department of Radiology, University of Pennsylvania, Philadelphia, PA, USA

Short title: Discovery of novel ACLY inhibitors for cancer therapeutics

Keywords: ACLY, tyrosine phosphorylation, lipid metabolism, drug discovery

*** Correspondence:**

Johnvesly Basappa, Ph.D.

Fox Chase Cancer Center, Philadelphia, PA 19111

Email: Johnvesly.Basappa@fccc.edu

Phone: 215-728-3039

Word count: Abstract 350; Main article: 7522

Number of Figures: Main Figures 1-9; Supplementary Figures 1-7;

Tables: MainTable-1; Supplementary Tabe-1 and 2

ABSTRACT

Background:

Metabolic plasticity contributes to therapeutic resistance in T-cell lymphoma, but the metabolic dependencies underlying tyrosine kinase inhibitor (TKI) resistance remain poorly understood. ATP citrate lyase (ACLY), which converts citrate to cytosolic acetyl-CoA, links glucose metabolism to lipogenesis and acetylation-dependent regulation. We hypothesized that ACLY represents an actionable metabolic vulnerability in lymphoma.

Methods:

Structure-guided drug discovery and biochemical screening were used to identify the novel ACLY inhibitor VCB1. VCB1 was evaluated against recombinant human ACLY and in TKI-sensitive and TKI-resistant lymphoma models. Antitumor activity was assessed by proliferation, cell-cycle analysis, apoptosis, and immunoblotting, followed by integrated transcriptomic, metabolomic, and lipidomic profiling.

Results:

Our xenograft study showed that ACLY dependence in ALK+ALCL. We discovered novel ACLY inhibitor VCB1 directly inhibited recombinant ACLY with μM potency (IC_{50}, 0.9 μM) and strongly suppressed lymphoma cell growth. In ALK inhibitor-sensitive SUPM2, VCB1 showed an IC_{50} of 0.299 μM and retained potency in lorlatinib-resistant SUPM2-LR1000 cells (1.62 μM), whereas BMS-303141 was substantially less active (17.46 and 22.07 μM). VCB1 similarly inhibited BTK inhibitor sensitive and resistant mantle cell lymphoma cell growth (IC_{50}, 0.28 and 0.278 μM), compared with BMS-303141 (30.5 and 37.01 μM). Multi-omics profiling revealed suppression of de novo lipogenesis, including *ACACA, FASN*, and *PPARGC1B*, together with extensive remodeling of triglyceride, phospholipid, cardiolipin, ceramide, and acylcarnitine species and increased expression of fatty-acid oxidation genes. VCB1 activated the integrated stress response (ISR), inducing *ATF4, PPP1R15A, DDIT3, DDIT4* and *SESN2*, while disrupting purine and pyrimidine metabolism and reducing nucleotide biosynthetic genes, including *CAD,*

DHODH, UCK2, and *ATIC*. VCB1 further activated an ACLY–ISR–CHAC1 axis associated with reduced GCLC/GCLM expression, glutathione depletion, and a decreased GSH/GSSG ratio, indicating impaired redox homeostasis. TKI-resistant cells exhibited distinct lipid-metabolic remodeling consistent with metabolic plasticity. VCB1 also altered immune-regulatory programs involving *PDCD1, TIGIT, CD247, CD226, NFATC2*, and inflammatory cytokines. Functionally, VCB1 induced cell cycle arrest and apoptosis.

Conclusions:

ACLY represents an integrated metabolic and signaling vulnerability in lymphoma. VCB1 suppresses lymphoma growth across TKI-sensitive and resistant models by disrupting lipid and nucleotide metabolism, metabolic adaptation and ISR and redox homeostasis supporting ACLY inhibition as a therapeutic strategy for TKI-resistant lymphoma.

65 **Background**

66 The global rise in cardiometabolic disorders, including atherosclerosis, non-alcoholic fatty liver disease
67 (NAFLD), and type 2 diabetes, has intensified efforts to identify therapeutic targets beyond conventional
68 lipid-lowering strategies. ATP-citrate lyase (ACLY) is a cytosolic enzyme that occupies a central position
69 in cellular metabolism by catalyzing the ATP-dependent conversion of citrate into acetyl-CoA and
70 oxaloacetate. As the primary source of cytosolic acetyl-CoA, ACLY supports de novo lipid biosynthesis
71 and histone acetylation, thereby integrating carbohydrate metabolism with lipid synthesis and epigenetic
72 regulation(1-3). ACLY activity is tightly regulated by multiple post-translational modifications, including
73 phosphorylation, acetylation, ubiquitination, and glycosylation. Among these, phosphorylation of serine
74 455 enhances enzymatic activity (4). We previously identified tyrosine 682 phosphorylation of ACLY as
75 a novel regulatory event mediated by oncogenic tyrosine kinases and demonstrated its functional impact on
76 ACLY activity (5, 6). These modifications increase ACLY-dependent acetyl-CoA production, thereby
77 promoting lipid biosynthesis and metabolic reprogramming. Consistently, ACLY overexpression and
78 hyperactivation have been implicated in diverse pathological conditions, including hyperlipidemia (7), non-
79 alcoholic fatty liver disease (NAFLD)(8, 9), and multiple cancers, including lung(10), breast(11),
80 prostate(12), liver(13), pancreatic(14) and colon cancer(15), where enhanced acetyl-CoA metabolism
81 supports tumor growth, survival, and progression.

82 Emerging evidence has established ACLY as a metabolic vulnerability across cancer types. ACLY-derived
83 acetyl-CoA directly fuels histone acetylation, thereby linking cellular metabolism to chromatin remodeling
84 and epigenetic plasticity. This is particularly relevant in hematologic malignancies, which are characterized
85 by profound metabolic and epigenetic rewiring. In murine hematopoietic stem and progenitor cells
86 (HSPCs), pharmacologic inhibition or genetic deletion of ACLY promotes myeloid differentiation (16). In
87 PTEN-deficient T-cell acute lymphoblastic leukemia (T-ALL), ACLY is required for thymocyte
88 transformation and tumor growth (17), while cooperative interactions between ACLY and MYC further
89 drive leukemogenesis (18). In acute myeloid leukemia (AML), ACLY overexpression accelerates disease

progression (19). Moreover, genetic or pharmacologic inhibition of ACLY suppresses tumor growth, induces apoptosis, and enhances therapeutic sensitivity in leukemia and lymphoma models (20). Collectively, these findings position ACLY as both a metabolic regulator and epigenetic modulator with therapeutic relevance in hematologic malignancies.

Despite decades of research, the development of clinically effective ACLY inhibitors has proven challenging. Early-generation inhibitors, including SB-204990 (21, 22), BMS-303141(23), and the recently reported NDI-091143(24), demonstrated potent enzyme inhibition but were limited by poor aqueous solubility, suboptimal oral bioavailability, short in vivo half-lives, and insufficient cellular activity. These pharmacologic shortcomings restricted their translation into effective systemic therapies. Although ACLY has attracted considerable interest as a therapeutic target for hyperlipidemia, cancer, and other metabolic disorders, the discovery of clinically viable inhibitors has been hindered by the predominance of substrate-like compounds targeting conserved catalytic pockets and the limited availability of chemically diverse scaffolds with favorable pharmacological properties(25). The clinical approval of Bempedoic acid by the U.S. Food and Drug Administration provided the first validation of ACLY as a druggable metabolic target in humans as a cholesterol lowering agent (26). Bempedoic acid is a liver-specific pro-drug activated by ACSVL1, an enzyme predominantly expressed in hepatocytes, where it inhibits ACLY and reduces acetyl-CoA production required for cholesterol and lipid biosynthesis (27). More recently, EVT0185 was identified as an ACLY inhibitor that is similarly converted to its active CoA derivative by the liver-enriched enzymes FATP2 and ACSVL1(28). While these compounds demonstrate the therapeutic feasibility of ACLY inhibition, their liver-restricted activation limits broader applications, particularly in oncology, where effective systemic inhibition is necessary to target malignant cells residing in diverse tissues. Despite these advances, most ACLY inhibitors reported to date exhibit limitations related to pharmacokinetic properties, tissue-selective activation, or insufficient cellular activity, underscoring the need for new compounds capable of achieving effective systemic ACLY inhibition in cancer. Such efforts are particularly

114 relevant in hematologic malignancies, where ACLY-mediated metabolic and epigenetic programs
115 contribute to disease progression and therapeutic resistance.

116 Building upon the clinical validation of ACLY inhibition and recent advances in high-resolution ACLY
117 structural biology (29), we employed a structure-based virtual screening strategy to identify novel small-
118 molecule ACLY inhibitors with improved cellular activity. Given the dual role of ACLY in regulating
119 metabolic pathways and acetylation-dependent gene expression, we investigated the biological
120 consequences of ACLY inhibition in ALK-positive anaplastic large cell lymphoma (ALK+ ALCL) models,
121 including both ALK inhibitor sensitive (ALKi-S) and resistant (ALKi-R) cell lines. This work builds upon
122 our earlier discovery that oncogenic NPM-ALK directly phosphorylates ACLY at tyrosine 682, thereby
123 regulating lipid metabolism and promoting ALCL tumorigenesis(6, 30, 31). Subsequent studies established
124 that ACLY Y682 is also a target of Src-family kinases, including LYN, and identified ACLY as a novel
125 signaling effector downstream of the PI3K/PIP2/PIP3/LYN axis in acute myeloid leukemia, linking
126 oncogenic kinase signaling to acetyl-CoA production, lipid biosynthesis, histone acetylation, and leukemic
127 cell growth(32). These findings, together with translational efforts targeting the PI3K/LYN/ACLY
128 signaling network (WO 2020/243063 A1), provided the biological rationale for the development of direct
129 ACLY inhibitors described herein. Our studies provide mechanistic insights into ACLY dependent
130 metabolic regulation and establish a framework for the development of next-generation ACLY targeted
131 therapies for hematologic malignancies.

132 In this study, we build upon the signaling–metabolism axis by identifying and characterizing novel ACLY
133 inhibitors through structure-based virtual screening and evaluating their activity in ALK+ ALCL models
134 with distinct ALKi sensitivity and resistance. Using integrated transcriptomic, metabolomic, and untargeted
135 lipidomic profiling, we define the metabolic and transcriptional consequences of ACLY inhibition and
136 identify stress-response pathways associated with therapeutic response. These findings establish ACLY as
137 an actionable metabolic vulnerability and provide a mechanistic framework for developing next-generation
138 ACLY-targeted strategies for TKI-resistant hematologic malignancies.

Methods and materials

Cell lines:

ALK Inhibitor (ALKi)-Resistant ALCL Cell Lines

ALCL cell lines cultured as described by our group earlier(33, 34). Briefly, SUPM2 parental and ALK inhibitors crizotinib-and lorlatinib resistant SUPM2 cell lines SUPM2 CR03 (resistant up to 300 nM of crizotinib and cultured at that concentration) and ALKi lorlatinib-resistant cell line SUPM2 LR1000 (resistant up to 1000 nM of lorlatinib and cultured at 300 nM of lorlatinib). The cell lines were grown in RPMI medium supplemented with 10% FBS and 1% penicillin/streptomycin in a humidified incubator at 37 °C with 5% CO_2. For the MTT assay the cell lines were culture in were grown in RPMI medium supplemented with 5% FBS and 1% penicillin/streptomycin in a humidified incubator at 37 °C with 5% CO_2Mantle cell lymphoma (MCL) cell lines JeKo-1 and Maver were cultured in RPMI-1640 medium supplemented with 10% fetal bovine serum (FBS) and 1% penicillin/streptomycin (Pen/Strep) in a humidified incubator at 37 °C with 5% CO_2. For the MTT assay the cell lines were culture in were grown in RPMI medium supplemented with 5% FBS and 1% penicillin/streptomycin in a humidified incubator at 37 °C with 5% CO_2.

Reagents and antibodies

Cell Proliferation Reagent WST-1 (Millepore-sigma), CellTiter 96® Non-Radioactive Cell Proliferation Assay (MTT) kit (catalog#G4001) from Promega. HA Pierce IP Lysis Buffer, Halt Protease and Phosphatase Inhibitor, GAPDH (catalog# 60004-1-Ig) from Proteintech, HA-Tag (C29F4) Rabbit (catlog# 3724S), Phospho-ALK (Tyr1604) Antibody (catalog# 3341S), ALK (D5F3®) XP® Rabbit (catalog# 3633S) from Cell Signaling Technology. ACLY antibody from Proteintech.

In-silico structure based ACLY inhibitors screening

161 A five-point 3D pharmacophore model was generated from the adenine nucleoside interactions of ADP
162 bound to human ATP-citrate lyase (ACLY). The model consisted of one hydrogen-bond donor (Don), three
163 hydrogen-bond acceptors (Acc), and one aromatic ring center (Ar). Distance constraints between donor and
164 acceptor features were incorporated to capture the essential binding interactions within the human ACLY–
165 ADP complex. A five-point 3D pharmacophore model was generated based on the adenine nucleoside
166 interactions observed between bound ADP and human ACLY (PDB ID: 3PFF; https//www.rcsb.org). The
167 pharmacophore incorporated the following features: hydrogen bond donor (Don), hydrogen bond acceptor
168 (Acc), aromatic ring center (Ar), and donor/acceptor (Don or Acc) functionalities. Distance constraints were
169 applied between the acceptor, donor, and donor/acceptor features to preserve the spatial arrangement critical
170 for ligand recognition. The NCI database was downloaded in its entirety and filtered prior to screening
171 using the following criteria: molecular weight (MW) < 500 Da, fewer than 8 rotatable bonds, fewer than 5
172 hydrogen bond donors, and fewer than 10 hydrogen bond acceptors. Only compounds represented as a
173 single molecular fragment were retained. Conformational analysis of the filtered compounds was
174 subsequently carried out using the conformational search module in Molecular Operating Environment
175 (MOE) by systematically varying all rotatable single bonds. A conformer database containing only
176 energetically favorable conformations was then generated.

177 Ligand-based silico screening was performed using selected pharmacophore queries derived from the 3D
178 pharmacophore model. Distance constraints between donor, acceptor, and donor/acceptor features were
179 incorporated into the search criteia. The energetically favorable conformers in the NCI database were
180 screened to identify compounds exhibiting greater than 65% feature overlap with the pharmacophore
181 model.

182 **RNA extraction, library preparation and sequencing**

183 Total RNA was isolated using the RNeasy Mini Kit (QIAGEN, Cat. no. 74104) according to the
184 manufacturer's instructions. RNA quantity and integrity were assessed by NanoDrop and Agilent

185 Bioanalyzer and 400 ng of total RNA per sample was submitted to Novogene (Beijing, China) for library
186 preparation and sequencing.

187 mRNA was purified from total RNA using poly-T oligo-attached magnetic beads. Following fragmentation,
188 first-strand cDNA was synthesized using random hexamer primers, followed by second-strand cDNA
189 synthesis. Libraries were completed through end repair, A-tailing, adapter ligation, size selection,
190 amplification and purification, and were quantified by Qubit and real-time PCR, with size distribution
191 assessed on a bioanalyzer. Libraries were pooled according to their effective concentration and target data
192 output and sequenced on an Illumina platform in paired-end mode.

193 **Reverse transcription quantitative polymerase chain reaction**

194 SUPM2 parental and SUPM2-LR1000 lorlatinib cell lines, were seeded in six-well plates up to 48 h. RNA
195 isolation and DNase treatment were performed according to the kit protocol (Qiagen #74104, #79254). The
196 RNA concentration was measured, and 1 µg was used for cDNA synthesis, which was performed with
197 SuperScript IV (Invitrogen #18091050). For the quantitative reverse transcription polymerase chain
198 reaction (qRT-PCR), 1 µL of cDNA was utilized. Each reaction contained: 1 µL of cDNA, 5 µL of
199 PowerUp™ SYBR™ Green Master Mix (Applied Biosystem, A25742), 0.5 µL of forward primer (from a
200 10 mM stock), 0.5 µL of reverse primer (from a 10 mM stock), and 3 µL of dH2O. Each condition was
201 tested in technical triplicate. Primers used are as follows.

202 Primer sequence 5′ to 3’

203 *ACSS1*, Forward- TTG AGA GCA CCC CAG TTT ATC; Reverse- GCA TCA CCG TAT TTC AGC AAC.

204 *ACSS2*, Forward- GGA TCA CTG GTC ATT CCT AC; Reverse- GTG CTG TGT AGA ACT TGG TC.

205 *CAD*, Forward- AGT GGT GTT TCA AAC CGG CAT; Reverse- CAG AGG ATA GGT GAG CAC TAA

206 *DHODH*, Forward-CCACGGGAGATGAGCGTTTC; Reverse-CAGGGAGGTGAAGCGAACA.

207 *PPP1R15A/GADDA34*,Forward-ATGATGGCATGTATGGTGAGC; Reverse- AACCTTGCAGTGTCCTTATCAG

208 *NLRP3*, Forward- GATCTTCGCTGCGATCAACAG; Reverse- CGTGCATTATCTGAACCCCAC

209 **Kyoto Encyclopedia of Genes and Genomes Pathway Analysis (Gene Ontology and Pathway**
210 **Analysis)**

211 The RNA sequencing (RNA-seq) data for SUPM2 and SUPM2-LR1000 ALKi sensitive and resistant cell
212 lines were filtered for differentially expressed genes (DEG) (fold change >1; FDR < 0.05) and these datasets
213 were subjected to Kyoto Encyclopedia of Genes and Genomes (KEGG) pathway analysis using DAVID
214 platform.

215 **Bioinformatics analysis**

216 Raw reads in FASTQ format were processed with fastp to remove adapter-containing reads, poly-N reads
217 and low-quality reads, and Q20, Q30 and GC content of the resulting clean reads were calculated. All
218 downstream analyses were performed on high-quality clean reads. Genome hg38 was used as reference
219 genome. An index of the reference genome was built with HISAT2 (v2.2.1), which was used to align the
220 paired-end clean reads with splice-aware mapping. Read counts per gene were obtained with feature Counts
221 (v2.0.6), and gene expression levels were expressed as FPKM. Differential expression analysis between
222 two groups was performed using DESeq2 (v1.42.0), with adjusted p-values by the Benjamini–Hochberg
223 method; genes with an adjusted $P \leq 0.05$ and log2 (fold change) ≥ 1 were considered significantly
224 differentially expressed.

225 **ACLY activity assay**

226 ACLY enzyme activity was determined using the malate dehydrogenase (MDH)-coupled method as
227 described earlier with little modification(6, 30, 32). For the screening of potential ACLY inhibitors we used
228 purified human recombinant ACLY protein that was incubated with various concentrations of our novel
229 compounds (VCB1, VCB2 and VCB7 along with reference compound BMS). For ACLY activity, 500 ng
230 to 1 µg of recombinant human proteins for each condition in triplicate well (96 plate) were incubated in
231 reaction buffer containing 10 mM potassium citrate, 10 mM MgCl2, 1 mM DTT, 10 U malic
232 dehydrogenase, 0.3 mM CoASH, 0.1 mM NADH in 50 mMTris (pH 8.0) and the reaction was initiated by
233 adding 0.2mM ATP in a final volume of 100 ul, incubated at 37°C, and NADH oxidation was continuously
234 monitored every 2 min for 60 min using a BioTeK plate reader. To measure the effect of a small molecule
235 inhibitor of VCB1 and BMS on ALK+ALCL and MCL cell lines cells were pretreated with VCB1 and
236 BMS at 1 µM for 24 hours. For the control experiments, lysis buffer was used in place of cell lysates for
237 nonspecific NADH oxidation. The relative ACLY activities were calculated by normalization to the total
238 protein abundance of the extracts in triplicate. The relative activity was calculated using PRISM GraphPad
239 10.6.1.

240 **Immunoblotting analysis**

241 Proteins were extracted using Thermo Scientific™ Pierce™ IP Lysis Buffer (Catalog No. PI87788)
242 containing a cocktail of protease and phosphatase inhibitors. For western blotting, 50 µg of total cell
243 proteins were subjected to SDS-PAGE in 10 or 4-20 % NuPAGE gradient gels under reducing conditions
244 and transferred onto a nitrocellulose membrane. The blots were blocked in 5 % skimmed milk in TBST and
245 probed with primary antibodies overnight. The blots were developed using ECL western blotting detection
246 reagent (GE Healthcare).

247 **MTT enzymatic conversion assay**Cells were plated in 96-well plates ($3–5\times10^3$/well) and treated with
248 ACLY inhibitors VCB1, VCB2, VCB7 and BMS or the drug vehicle and labeled with MTT (Promega).
249 Well contents were solubilized and absorbance was determined using a BioTeK plate reader.

250 **Cell cycle analysis**

251 SUPM2 parental, SUPM2 LR1000 resistant to lorlatinib, Jeko-1 and Maver cells were treated with 1 μM
252 concentration of VCB1 or BMS for 48 h. After the treatment, cells were fixed in 70% ice-cold ethanol, and
253 PI staining was performed using the FxCycle PI/RNase Staining Solution (Thermo Fisher Scientific). Data
254 from the gated tumor cells were acquired by running the samples on a FACSCanto II instrument. Cell cycle
255 plots of quiescent (G0-phase) and actively cycling tumor cells (G1-, S-, G2M-phase) were generated with
256 FlowJo software.

257 **Metabolomics Analysis**

258 Metabolomics analyses were conducted at The Wistar Institute Proteomics and Metabolomics Shared
259 Resource with slight modifications as previously described(35-37). The Global metabolomic analysis was
260 performed on SUPM2 and SUPM2-LR1000 (SLR, lorlatinib resistant) cell lines were cultured in 5%
261 dialyzed FBS and RPMI media and treated with 1.0 μM ACLYi VCB1 or BMS for 24 hr. The cells were
262 spun down at 1000 rom and washed with cold PBS and snap frozen in liquid nitrogen. The pellets were sent
263 to Wistar Metabolomics core.

264 **Global Lipidomics Analysis**

265 The Global Lipidomics analysis was performed as described earlier with modification to our cell lines(38).
266 SUPM2 and SUPM2-LR1000 (SLR, lorlatinib resistant) cell lines were cultured in 5% dialyzed FBS and
267 RPMI media and treated with 1.0 μM ACLYi VCB1 or BMS for 24 hr. The cells were spun down at 1000
268 rpm and washed with cold PBS and snap frozen in liquid nitrogen. The pellets were sent to Wistar
269 Metabolomics core. Samples were spiked with EquiSplash LIPIDOMIX internal standards (Avanti Polar
270 Lipids), and lipids were extracted using a methyl tert-butyl ether (MTBE)-based method. The upper organic
271 phase was collected, dried, and reconstituted in 9:1 methanol before storage at −20°C. Lipid extracts (10
272 μL per injection) were analyzed in randomized order by LC–MS/MS using a Thermo Scientific Q Exactive

273 HF-X mass spectrometer coupled to a Vanquish UHPLC system. A pooled quality-control (QC) sample
274 was analyzed periodically throughout the sequence to monitor analytical performance. Data were acquired
275 separately in positive- and negative-ion modes following reversed-phase chromatographic separation on a
276 C30 column. Lipid species were identified by MS/MS fragmentation using Thermo Scientific LipidSearch
277 4.2 and quantified based on peak areas. Identification confidence, expected adducts, retention-time
278 windows, peak quality, QC reproducibility, and data completeness were used for quality filtering.
279 Deuterated internal standards, species outside expected retention-time windows, lipids with average peak
280 quality <0.7, QC coefficient of variation >30%, and species with fewer than 30/30 valid experimental
281 measurements were excluded. Relative lipid abundances were corrected using EquiSplash standards for the
282 corresponding lipid classes and quantified using TraceFinder 4.1. Where appropriate, data were additionally
283 normalized to total lipid signal or sample weight.For lipid species-level comparisons, log2-transformed data
284 were analyzed using Student's *t*-test, with Benjamini–Hochberg correction for multiple testing.
285 Differentially abundant lipids were defined as those exhibiting ≥1.5-fold change with $p<0.05$ or $q<0.05$.
286 Lipid class abundances were calculated by summing peak areas of individual species within each class and
287 were compared using Student's *t*-test. MS/MS analysis did not resolve acyl-chain positional isomers or
288 double-bond positions.

289 **Statistical analysis**

290 Statistical analysis was performed via GraphPad Prism 8. Quantitative data are presented as
291 mean ± standard deviation (SD) and all statistical tests were performed with a minimum of three biological
292 replicates. If not otherwise stated, statistical testing was conducted by a two-sided unpaired t test to
293 determine significant differences between the control and corresponding treatment conditions. A p-value
294 of < 0.05 was considered statistically significant (*, p <0.05; **, p < 0.01; ***, p < 0.001; ****, p < 0.0001).

295 **Data availability**

296 We confirm that all relevant data and methods are included in the main article, and the supplementary
297 material of RNA-seq, Metabolomics and lipidomics will be uploaded to the appropriate website.

298 **Results**

299 **Structure-based identification and validation of a novel ACLY inhibitor**

300 ACLY is a central enzyme linking citrate metabolism to acetyl-CoA production and downstream lipid
301 biosynthesis. We sought to identify novel small-molecule ACLY inhibitors using a structure-based drug
302 discovery approach as shown in silico screening schematic (Fig.1A). The human ACLY crystal
303 structure was utilized to perform both ligand-based and structure-based in silico screening of the National
304 Cancer Institute (NCI) chemical database to identify potential inhibitors targeting the ATP-binding site
305 within the ATP-grasp domain of ACLY as shown in the schematic (Fig.1B). To identify novel ATP-citrate
306 lyase (ACLY) inhibitors, a structure-based pharmacophore model was generated from the adenine
307 nucleoside-binding interactions of ADP within the human ACLY binding site (PDBID: 3PFF) as shown
308 (Fig.1C). The resulting five-point 3D pharmacophore comprised one hydrogen-bond donor (Don), three
309 hydrogen-bond acceptors (Acc), and one aromatic ring center (Ar), reflecting the key interactions
310 responsible for ligand recognition (Fig.1D). To identify the docking pocket of ATP binding pocket, we used
311 the "Site finder" module of MOE (Chemical Computing Group, Montreal, Canada) to identify the potential
312 pocket and filled with dummy atoms. The dummy atom locations in the ATP binding site of ACLY structure
313 were used to dock the matched and energetically favorable conformers. Location of Dummy "atoms"
314 (sphere) identified in the ATP binding pocket. Red sphere has contact with atom(s) of ACLY protein and
315 gray sphere does not have contact with ACLY protein. The amino acid residues forming the pocket are
316 shown by gray for carbon, red for oxygen and blue for nitrogen (Fig.1D). The docking of active ACLY
317 inhibitor VCB#1(magenta surface) into the ATP binding pocket of ACLY (khaki colored ribbon) and the
318 amino acids in ACLY lining the binding pocket of VCB11 are shown by cornflower blue for carbon; red
319 for oxygen and blue for nitrogen (Fig.1E). The docked VCB1 in the ATP binding site of ACLY forms five

320 favorable hydrogen bonds with the side chain atoms of amino acids of ACLY protein R66, E108, E201 and
321 D216. Two R66 forms two hydrogen bonds with the two nitrogens in the six-member ring as shown (Fig.1F)
322 Distance constraints between pharmacophoric features were incorporated to preserve the spatial
323 arrangement observed in the human ACLY–ADP crystal structure. The model accurately mapped the
324 critical binding determinants of the adenine-binding pocket and was subsequently employed as a query for
325 virtual screening to identify compounds with the potential to engage the ATP-binding site of ACLY. Our
326 3D pharmacophore search as described lead to 131 unique compounds. Based on the MOE docking scoring
327 of each conformation-ACLY complex, the rank ordering of the complexes was carried out, we selected the
328 top 100 ACLY compound conformation complexes for further reduced to a list of unique compounds.
329 Based on the availability in NCI repository, we received 11 compounds for ACLY activity screening assay.
330 The 2D chemical structure of three active compounds and reference compound are shown in (Fig.1G). The
331 other selected compound 2D chemical structures are shown (Supplementary Fig.1). Next, the three
332 active compounds were subsequently tested for their ability to inhibit recombinant human ACLY enzymatic
333 activity, using the previously reported ACLY inhibitor BMS-303141 as a reference compound. The results
334 showed that our lead compounds compound#1 (VCB1), compound#2 (VCB2) and compound#7 (VCB7)
335 demonstrated an IC_{50} of 0.91, 0.46 and 1.19 μM respectively, confirming direct inhibitory activity against
336 recombinant ACLY (Fig.1H). Whereas the reference compound BMS-303141 inhibited recombinant
337 human ACLY with an IC_{50} of 0.26 μM in our study.

338 **Genetic silencing of ACLY in ALK+ALCL cell line and xenograft model revealed ACLY as a**
339 **therapeutic target**

340 To investigate the requirement for ACLY in ALK-positive ALCL tumor growth, we initially focused on
341 SU-DHL-1 cells, which showed relatively high ACLY expression among ALK-positive ALCL cell lines
342 as confirmed in our previous study(6). ACLY is a central metabolic regulator implicated in tumor growth
343 across multiple malignancies, and genetic ACLY silencing has been shown to induce growth arrest and

344 apoptosis in cancer cells(2, 39). However, genetic validation of *ACLY* dependence in lymphoma xenograft
345 models remains comparatively limited. We therefore generated SUDHL-1 cells expressing control shRNA
346 (shControl) or *ACLY*-targeting shRNA (shACLY) and evaluated tumor formation following subcutaneous
347 flank injection. All six mice injected with shControl cells developed tumors and detectable tumors observed
348 64 days after implantation and subsequently exhibited rapid tumor growth (Supplementary Fig.2A). Mean
349 tumor volume increased from 291.8 ± 97.7 mm^3 on day 64 to 1271.9 ± 521.5 mm^3 by day 76 (n=6)
350 (Supplementary Fig.2B). At the experimental endpoint, excised shControl tumors weighed 0.6–3.2 g, with
351 a mean weight of 1.82 ± 0.99 g (Supplementary Fig.2C). In contrast, no palpable tumors were detected in
352 seven mice injected with shACLY cells throughout the observation period, indicating that ACLY depletion
353 markedly impaired detectable tumor establishment in vivo (Supplementary Fig.2D). Together with recent
354 genetic evidence of ACLY dependence in T-cell acute lymphoblastic leukemia(40). These findings
355 provided further support for investigating ACLY as a potential therapeutic target in ALK-positive ALCL.

356 **A novel ACLY inhibitor, VCB1 suppresses ACLY activity and promotes cell death**

357 Our xenograft study provided a rationale for pharmacologic targeting of ACLY in ALK-positive ALCL.
358 We therefore next evaluated three lead ACLY inhibitors, VCB1, VCB2, and VCB7, together with the
359 reference ACLY inhibitor BMS-303141 (BMS), using the paired SUP-M2 parental and lorlatinib-resistant
360 SUP-M2-LR1000 cell lines. To evaluate the cellular activity of our lead ACLY inhibitors (VCB1, VCB2,
361 and VCB7) along with the reference inhibitor BMS, we examined their effects on lymphoma cell viability
362 and apoptotic signaling. ALK inhibitor (ALKi)-sensitive SUPM2 parental (S) cells, as well as crizotinib-
363 and lorlatinib-resistant lines (SUPM2 CR03 and SUPM2-LR1000 [SLR]), were treated with 1.0 μM of each
364 compound in medium containing 5% FBS for 48 hours. Immunoblot analysis revealed that among the three
365 novel compounds, VCB1 and VCB7 induced a marked increase in cleaved PARP1 and cleaved caspase-3,
366 indicating the activation of apoptotic cell death (Fig. 2A). Notably, this apoptotic response was most
367 pronounced in the parental SUPM2 cells, followed by the lorlatinib-resistant SLR cells, while the crizotinib-
368 resistant line exhibited the least sensitivity. We next investigated whether the activity of these lead

369 compounds extended to mantle cell lymphoma (MCL) models with differential sensitivity to the BTK
370 inhibitor ibrutinib. Ibrutinib-sensitive Jeko-1 and ibrutinib-resistant Maver cells were treated under the
371 same experimental conditions. Consistent with our observations in ALK+ ALCL, VCB1 induced robust
372 cleavage of PARP1 in both MCL cell lines, whereas VCB2, VCB7 and the reference compound BMS-
373 303141 elicited minimal apoptotic activation (Fig. 2B). These results demonstrate that the cytotoxic activity
374 of the ACLY inhibitor VCB1 extends across genetically and therapeutically distinct lymphoma models.
375 Based on these collective findings, VCB1 was selected as the primary lead compound for subsequent
376 mechanistic studies and direct comparison with BMS-303141. We next investigated whether VCB1 altered
377 ACLY expression and the expression of key metabolic enzymes associated with the ACLY-dependent
378 lipogenic pathway. SLR cells were treated with VCB1 or BMS at 1.0 μM for 24 h, followed by RNA
379 isolation and gene-expression analysis. VCB1 significantly reduced the expression of *ACLY* as well as the
380 downstream lipogenic enzymes *ACACA* and *FASN* and the acetate-utilizing enzyme *ACSS2* (Fig. 2C–F). In
381 contrast, BMS did not produce a comparable reduction in these metabolic genes. These findings suggested
382 that VCB1 produces a broader suppression of the *ACLY*-dependent metabolic transcriptional program than
383 the reference compound. Our previous studies demonstrated that NPM-ALK directly phosphorylates ACLY
384 at Y682, thereby enhancing ACLY activity and supporting lipid biosynthesis in ALK+ lymphoma cells.
385 Thus, ACLY represents a metabolic effector downstream of oncogenic NPM-ALK signaling, linking
386 tyrosine kinase signaling to de novo lipid synthesis (Fig. 2G). To determine whether the cellular effects of
387 VCB1 were associated with inhibition of ACLY enzymatic activity, we measured cellular ACLY activity
388 following treatment with VCB1 or BMS in sensitive (SUPM2 parental and SUDHL1) and ALKi-resistant
389 ALK+ ALCL and in MCL cell lines. VCB1 treatment produced a substantial reduction in cellular ACLY
390 activity compared with BMS across the lymphoma models examined (Fig. 2H–M). Collectively, these
391 results demonstrate that VCB1 inhibits ACLY activity in lymphoma cells, suppresses expression of key
392 lipogenic enzymes, and induces apoptotic cell death. The substantially greater cellular activity of VCB1
393 compared with VCB2, VCB7 and BMS provided a rationale for selecting VCB1 as the lead compound for
394 subsequent transcriptomic, metabolomic, and lipidomic studies.

395 **ACLY inhibition suppresses lipogenesis and induces metabolic and proliferative reprogramming**

396 To define the transcriptional consequences of ACLY inhibition, we performed RNA sequencing (RNA-
397 seq) in SUPM2 parental and SLR cells following treatment with VCB1 or BMS. Cells were treated with
398 1.0 μM compound for 24 h, and RNA from three biological replicates per condition was subjected to RNA-
399 seq. The distribution of differentially expressed genes (DEGs) across the comparisons is summarized
400 (Supplementary Fig. 3A). VCB1 induced a substantially stronger transcriptional response than BMS in both
401 cell lines. The largest transcriptional response occurred in S-VCB1 versus S-DMSO cells, whereas S-BMS
402 versus S-DMSO produced relatively few DEGs (Supplementary Fig. 3B–E). A similar pattern was observed
403 in SLR cells, in which VCB1 produced substantially more transcriptional changes than BMS. Baseline
404 comparison of untreated SLR and parental cells also demonstrated extensive transcriptional reprogramming
405 associated with acquired ALKi resistance (Supplementary Fig. 3F). Using a threshold of log2 FC ≥1 and
406 P<0.05, VCB1 treatment in parental S cells resulted in 793 upregulated and 209 downregulated genes,
407 whereas 24,781 genes remained unchanged (Supplementary Fig. 3D). In comparison, BMS treatment
408 resulted in only 42 upregulated and 65 downregulated genes, with 25,435 genes unchanged (Supplementary
409 Fig. 2E). Many genes uniquely altered by BMS were non-coding RNAs, pseudogenes, or poorly
410 characterized loci, whereas VCB1 produced a broader response involving protein-coding genes.

411 The more pronounced transcriptional response to VCB1 was retained in SLR cells, demonstrating that
412 VCB1 engages a strong cellular response despite acquired ALKi resistance. Baseline comparison of
413 untreated SLR and S cells identified 3,318 upregulated and 2,979 downregulated genes in SLR cells, with
414 21,183 genes remaining unchanged. Thus, acquired ALKi resistance was associated with extensive
415 transcriptional reprogramming, creating a metabolically distinct cellular state in which ACLY inhibition
416 produced a broad adaptive and stress response. To capture moderate but potentially biologically important
417 transcriptional changes, we subsequently applied a threshold of log2 FC ≥0.5 and P<0.05. This analysis
418 identified 1,427 DEGs in TKI-sensitive cells and 3,712 DEGs in TKI-resistant SLR cells. Venn analysis
419 identified 561 genes unique to S cells, 2,839 unique to SLR cells, and 866 commonly regulated genes (Fig.

420 3A). Thus, the transcriptional consequences of VCB1 were substantially broader in resistant cells,
421 consistent with greater metabolic and stress adaptation in the resistant state. To identify molecular pathways
422 affected by VCB1 mediated ACLY inhibition, a pathway enrichment analysis was carried out using the
423 Database for Annotation, Visualization and Integrated Discovery (DAVID) focusing on the Gene Ontology
424 Biological Processes (GO_BP), Kyoto Encyclopedia of Genes and Genomes (KEGG), Reactome, and Wiki
425 Pathways(41). KEGG pathway analysis using NIH-DAVID demonstrated enrichment of ribosome
426 biogenesis, amino-acid biosynthesis, HIF-1 signaling, TNF signaling, carbon metabolism, and broader
427 metabolic pathways (Fig. 3B, C). Among the 866 genes commonly regulated by VCB1 in sensitive and
428 resistant cells, VCB1 suppressed key components of the lipogenic program, including *ACLY, ACACA,*
429 *FASN, GPAM, and HACD2*, together with genes involved in lipid remodeling and homeostasis, including
430 *INSIG1, INSIG2, PLIN2, STARD4,* and *SLC27A4*. These changes were consistent with suppression of
431 ACLY-dependent de novo lipid synthesis. VCB1 simultaneously altered genes involved in glycolysis,
432 hypoxia, and metabolic stress, including *SLC2A1, SLC2A3, PFKFB3, PFKFB4, PGK1, CA9, BNIP3,*
433 *BNIP3L*, and *DDIT4. PFKFB4* was induced in both cellular states, with a stronger induction in sensitive
434 cells, consistent with a compensatory response to altered glycolytic and energetic demands. In parallel,
435 genes involved in cell-cycle progression and mitosis, including *CCNB1, CDC20, PLK1, CENPE, CENPF,*
436 *KIF20A, KIF23*, and *PTTG1*, were predominantly downregulated (Fig. 3D–F). These findings indicate that
437 ACLY inhibition couples metabolic stress to suppression of proliferative programs. The response was more
438 pronounced in SLR cells, whereas VCB1 suppressed genes involved in fatty-acid synthesis, elongation,
439 cholesterol metabolism, and lipid remodeling, including *FASN, ACACA, HACD2, HACD3, LPCAT3,*
440 *LPCAT4, DHCR24, MECR, MCAT, CPT1A*, and *PPARGC1B. PPARGC1B*, which regulates oxidative and
441 lipid metabolic programs, was particularly reduced in resistant cells. In contrast, genes associated with
442 fatty-acid oxidation, lipid uptake, and lipoprotein metabolism, including *ACADS, ACADVL, PPARA, LPL,*
443 *LRP1, LDLR, VLDLR, HMGCL*, and *OSBPL5*, were increased (Fig. 3G). Thus, ACLY inhibition
444 suppressed endogenous lipid synthesis while inducing a compensatory transcriptional program favoring
445 lipid uptake and oxidative metabolism. Basal comparison of S and SLR cells revealed further metabolic

446 differences. SLR cells preferentially expressed genes involved in cholesterol biosynthesis, lipid storage,
447 remodeling, and uptake, including *DHCR24, FDFT1, MSMO1, FADS2, DGAT2, MOGAT2, APOC1,*
448 *APOE, LIPE, HILPDA, and LDLRAP1*, whereas parental S cells showed greater expression of genes
449 involved in glycerophospholipid synthesis and remodeling (Fig. 3H,I). Examination of SREBP-associated
450 genes further supported suppression of lipid biosynthesis. VCB1 reduced *HMGCR, GPAM, SLC27A4,*
451 *ACLY, DHCR7, ACACA, HMGCS1, FASN,* and *PPARGC1A*, while increasing *OSBPL3, OSBPL6, INSIG1,*
452 *INSIG2, DHCR24, HMGCL*, and *LRP1* (Fig. 3J). Next, we performed STRING-protein analysis and results
453 demonstrated an interconnected ACLY-associated metabolic network (Fig. 3K). VCB1 also increased
454 expression of cell-cycle checkpoint and stress-response genes, including *CDKN1A, E2F7, SESN2, DDIT4,*
455 *BNIP3,* and *BTG1*, while reducing mitotic regulators such as *CDC20 and KIF20A* (Fig. 3L). To further,
456 STRING-protein pathway analysis revealed enrichment of DEGs involved in TNFα and IL-17 related genes
457 (Fig.3M).

458 To better visualize the interactions among the common differentially expressed genes (DEGs) across both
459 cell lines, we performed a network analysis using the STRING database. First, we mapped all common
460 DEGs meeting the threshold of log2 fold change (FC) +/- 1.0 and ($P < 0.05$), irrespective of their functional
461 classification (Supplementary Fig. 4). Using the same statistical criteria, we specifically isolated and
462 mapped the network of common DEGs involved in metabolic pathways (Supplementary Fig. 5A). Because
463 ACLY inhibition alters lipid levels and remodels gene expression in response to lipid-mediated stress, we
464 next performed a Gene Ontology (GO) biological process analysis. This analysis revealed a significant
465 enrichment of DEGs involved in the cellular response to lipids (Supplementary Fig. 5B). Furthermore,
466 network analysis highlighted distinct signaling clusters related to both TNF and HIF-1 signaling pathways
467 (Supplementary Fig. 5C and D).

468 **VCB1 induces DEGs involved in Metabolic and transcriptional reprogramming in TKI-sensitive and**
469 **TKI-resistant cells**

470 To define metabolic function associated with DEGs, cells were analyzed using a log2 fold-change threshold
471 of ≥ +0.5 or ≤ −0.5. RNA-seq identified a distinct set of common metabolic DEGs shared between two cell
472 lines (Table-1). These genes revealed coordinated alterations in glycolysis, lipid metabolism, mitochondrial
473 function, and amino-acid metabolism, including induction of glycolytic genes such as PFKFB4 and PFKL,
474 together with suppression of key lipogenic and mitochondrial genes including *ACACA, FASN, CS, DLAT*,
475 and *PPARGC1B*. Notably, *PPARGC1B* suppression was substantially greater in resistant cells, suggesting
476 enhanced impairment of mitochondrial oxidative and lipid metabolic programs during TKI resistance. In
477 contrast, SUPM2 parental, specific DEGs displayed a metabolic signature characterized by increased
478 glycolysis, lipid uptake/storage, amino-acid biosynthesis, and nutrient-stress signaling, exemplified by
479 *PFKFB4, ANGPTL4, VLDLR, HILPDA, GPT2, ASNS, SESN2*, and *DDIT4* (Supplementary Table-1). These
480 changes suggest that TKI-sensitive cells respond to metabolic perturbation by activating alternative
481 nutrient-utilization and metabolic stress-adaptation pathways. The SLR specific DEGs revealed a broader
482 and more complex metabolic phenotype, characterized by enhanced glucose uptake and glycolytic
483 adaptation, glutamine metabolism, redox/glutathione metabolism, and stress responses, including induction
484 of *SLC2A1, PDK1, PDK3, GLUL, CHAC1*, and *SOD2*. At the same time, resistant cells showed extensive
485 suppression of mitochondrial oxidative metabolism, TCA-cycle activity, fatty-acid metabolism,
486 phospholipid synthesis, and nucleotide biosynthesis, including *CAD, CPT1A, IDH3A, OGDH, FH,*
487 *DHODH*, and multiple mitochondrial respiratory-chain genes (Supplementary Table-2). Collectively, the
488 shared and group-specific metabolic DEGs define distinct metabolic signatures associated with TKI
489 sensitivity versus resistance. While both populations exhibit suppression of key lipogenic and
490 mitochondrial pathways, TKI-sensitive cells preferentially activate metabolic stress, nutrient uptake, and
491 biosynthetic adaptation, whereas TKI-resistant cells display a more extensive metabolic reprogramming
492 characterized by glycolytic dependence, glutamine/redox adaptation, and broad mitochondrial and anabolic
493 metabolic suppression.

494 **VCB1 treatment and cancer hallmark analysis on DEGs revealed metabolic reprogramming and**
495 **inflammatory adaptation**

496 Analysis of cell-line-specific DEGs revealed distinct biological responses to ACLY inhibition. At the log2
497 FC ≥0.3 threshold, VCB1-treated SLR cells showed enrichment of cancer hallmarks associated with
498 genome instability, reprogramming energy metabolism, replicative immortality, and resistance to cell death
499 (Fig. 4A). When downregulated genes were analyzed separately at the log2 FC ≥0.7 threshold,
500 reprogramming energy metabolism was significantly enriched, involving 27 genes (P=0.00257; FDR-
501 adjusted P=0.0231) (Fig. 4B). The enriched genes included *ACLY, ACACA, FASN, PPARG, PFKM, IDH1,*
502 *IDH3A, CS,* and *DLAT*, together with mitochondrial respiratory-chain and TCA-cycle genes. These findings
503 indicate that VCB1 suppresses a broad tumor-associated energy-metabolic program rather than affecting
504 lipid synthesis alone. In contrast, upregulated DEGs in SLR cells were enriched for the sustained
505 angiogenesis hallmark (Fig. 4C). At a log2 FC threshold of 0.7, the strongest enrichment was driven by
506 *TNF, THBS1, TGFBR1, CXCR3, MMP1, ITGA5, IL6, SDC4, CSF3*, and *CXCL10*. Tumor-promoting
507 inflammation and immune-evasion programs were also represented by genes including *TNF, TNFSF13B,*
508 *PDCD1, IL6, LY96, FCGR1A, CD247, IL2RG, CXCL10*, and *BCL6*. These data indicate that ACLY
509 inhibition elicits an inflammatory and immune-associated transcriptional response in addition to metabolic
510 suppression. Analysis of genes commonly upregulated in S-VCB1 and SLR-VCB1 cells at log2 FC ≥0.7
511 revealed enrichment for sustained angiogenesis, resistance to cell death, and reprogrammed energy
512 metabolism (Fig. 4D). Similar analysis using a log2 FC ≥0.5 cutoff demonstrated enrichment of
513 reprogramming energy metabolism and sustained angiogenesis among common DEGs (Supplementary Fig.
514 6A, B). Common upregulated genes were additionally enriched for sustained angiogenesis, sustained
515 proliferative signaling, resistance to cell death, and reprogrammed energy metabolism, whereas
516 downregulated genes were significantly enriched for reprogrammed energy metabolism (Supplementary
517 Fig. 6C–F). Collectively, these analyses demonstrate that VCB1 produces a conserved metabolic response

518 across TKI-sensitive and TKI-resistant cells, while the resistant state additionally engages stronger
519 inflammatory, angiogenic, and adaptive stress programs.

520 **VCB1 induces extensive metabolic remodeling characterized by citrate accumulation and nucleotide**
521 **depletion**

522 To determine whether the transcriptional consequences of ACLY inhibition were accompanied by
523 metabolic changes, we performed integrated untargeted metabolomic analysis. Untargeted metabolomics
524 of TKI-sensitive SUPM2 cells treated with DMSO, VCB1, or BMS identified 307 metabolites. Significance
525 was defined as a ≥1.5-fold change with adjusted $q<0.05$. Hierarchical clustering demonstrated a distinct
526 metabolic profile in VCB1-treated cells compared with DMSO controls (Fig. 5A). A stringent fourfold
527 cutoff was subsequently used to highlight the most strongly altered metabolites (Fig. 5B). VCB1 markedly
528 depleted metabolites associated with purine and pyrimidine metabolism. The most strongly decreased
529 metabolites with significant q-value of < 0.05 included with fold change are dADP (−34.06-fold), cytosine
530 (−29.36-fold), AMP (−20.61-fold), UMP (−16.26-fold), and TMP (−16.23-fold). These coordinated
531 changes revealed a broad disruption of nucleotide metabolism following ACLY inhibition. VCB1 also
532 induced marked accumulation of central-carbon metabolites, including D-myo-inositol 1,4-bisphosphate
533 (1810.66-fold), DHAP/GAP (151.54- and 33.37-fold), phosphoenolpyruvate (99.59-fold), and 3-
534 phosphoglyceric acid (20.93-fold), together with glucosamine-6-phosphate, mannose-6-phosphate, acetyl-
535 CoA, and Asp-Asp. These findings indicate extensive remodeling of glycolysis and central carbon
536 metabolism (Fig. 5B). Conversely, citrate, the direct substrate of ACLY, accumulated 2.64-fold following
537 VCB1 treatment ($q=0.0017$). Although citrate did not reach the fourfold cutoff used for the focused
538 heatmap, analysis of raw metabolite peak intensity confirmed its accumulation following VCB1 treatment
539 but not in BMS treated cells (Fig. 5C). Citrate accumulation therefore provided an important metabolic
540 signature consistent with intracellular inhibition of ACLY as clarified by the schematic conversion of citrate
541 and acetyl-CoA via ACLY shown in Fig.5C lower panel. On the other hand, it is possible to notice the
542 citrate in the volcano plots showing the deregulated metabolites (Fig.5D). Not surprisingly, we recorded an

543 increase of acetyl-CoA following VCB1 treatment, because untargeted metabolomics does not resolve
544 cytosolic, nuclear, and mitochondrial acetyl-CoA pools, and this finding does not necessarily indicate
545 preservation of the cytosolic acetyl-CoA pool required for ACLY-dependent lipogenesis. Acetyl-CoA may
546 also arise from acetate utilization through ACSS2(42, 43) or from mitochondrial fatty-acid oxidation(44).
547 Consistent with this interpretation, ACLY loss has previously been shown to increase acetate dependence
548 through ACSS2 in CD8 T cells(45). Thus, the increase in total acetyl-CoA may reflect compensatory
549 production from alternative metabolic sources rather than maintenance of ACLY-derived cytosolic acetyl-
550 CoA. On the other hand, BMS-303141 produced substantially fewer metabolic changes and did not induce
551 comparable citrate accumulation (Fig. 5E). Next, we performed Pathway enrichment and pathway impact
552 analysis by using MetaboAnalyst online tool as described earlier(35, 46). The results showed that
553 significantly altered metabolites identified purine and pyrimidine metabolism as the most strongly enriched
554 pathways (Fig. 5F). Pathway impact analysis further identified pyrimidine, purine, pyruvate, and citrate
555 metabolism as major affected pathways (Fig. 5G). SLR cells contained increased abundance of multiple
556 nucleotide metabolites, indicating a metabolically distinct state characterized by enhanced nucleotide
557 availability (Fig. 5H). Furthermore, the ACLYi VCB1 cell line produced an overall metabolic response in
558 resistant cells like that of the SUMP2 parental line (Fig. 5I). Together, these data demonstrate that
559 VCB1mediated ACLY inhibition produces coordinated remodeling of central carbon and nucleotide
560 metabolism.

561 **VCB1 produces extensive lipidomic remodeling distinct from BMS-303141**

562 We next performed global lipidomic profiling of SUPM2 parental, and SLR cells treated with VCB1, BMS,
563 or DMSO. Principal component analysis demonstrated clear treatment-dependent separation in both cell
564 lines. In parental cells, DMSO, VCB1, and BMS samples formed distinct clusters, with VCB1 separating
565 predominantly along PC1 and BMS along PC2 . A similar pattern was observed in SLR cells (Fig. 6A and
566 B). In parental cells, VCB1 induced pronounced changes in multiple lipid species. The results showed that
567 at using a stringent >15-fold-change threshold, the most prominent increased lipid species involved in

568 sphingolipids, particularly ceramides and hexosylceramides, together with SM(d41:0),
569 Hex2Cer(d18:0_24:0), LPE(16:0e), and PE(18:1p_20:4). Only three species PG(12:0_14:0),
570 PG(10:0_14:0), and SM(d39:6) were strongly decreased (Fig. 6C–E). A similar pattern was observed in
571 SLR cells, in which ceramides and related sphingolipids represented a major fraction of the most strongly
572 increased species (Fig. 6F). These changes were substantially weaker following BMS treatment.

573 **ACLY Inhibition by VCB1 Reprograms Lipid Metabolism and Mitochondrial Fatty-Acid**

574 The lipidomics analysis revealed that remodeling of lipid species across acylcarnitines, ceramides,
575 glycosphingolipids, PC, PE, PG, cardiolipin, PS, PI, SM, DG, cholesteryl esters, and TG (Fig. 7A). In
576 sensitive cells, numerous TG species containing oleate, very-long-chain fatty acids, and mixed unsaturated
577 chains were depleted, whereas selected saturated C16–C18, ether-linked, and PUFA-containing TGs
578 increased (Fig. 7B). PC species also shifted toward ether and PUFA-containing species, including
579 PC(16:0e/20:4), PC(18:0e/22:6), and PC(16:1e/20:4), with depletion of conventional diacyl PCs (Fig. 7C).
580 PE exhibited a particularly strong shift toward ether/plasmalogen- and PUFA-rich species, including
581 PE(18:0e/20:4), PE(16:0e/20:5), PE(18:1p/20:4), PE(18:0e/22:5), and PE(18:0e/22:6) (Fig. 7D). DG
582 species were extensively remodeled in both cell lines, whereas BMS produced comparatively weak changes
583 (Fig. 7E). Further, ChE species were also broadly altered, with different responses between sensitive and
584 resistant cells (Fig. 7F). VCB1 increased long-chain saturated acylcarnitines, including AcCa(17:0), (18:0),
585 (19:0), (20:0), (22:0), and (24:0), while decreasing shorter-chain and unsaturated species including
586 AcCa(9:0), (10:0), (12:1), (14:0), (16:1), (18:1), and (18:2) (Fig. 7G), consistent with altered mitochondrial
587 fatty-acid handling. Mitochondrial and membrane phospholipids were also remodeled, including
588 predominant depletion of identified cardiolipin and PS species. Acylcarnitines are intermediates required
589 to transport fatty acids into the mitochondria for energy production. The accumulation of very-long and
590 long-chain species, paired with the drop in shorter-chain species, indicates a "bottleneck" in mitochondrial
591 beta-oxidation. VCB1 likely blocks or overwhelms the enzymes responsible for breaking down long-chain
592 fatty acids, leading to mitochondrial congestion and severe bioenergetic stress. Collectively, these results

593 establish that VCB1 produces substantially broader lipid remodeling than BMS, encompassing neutral
594 lipids, membrane phospholipids, mitochondrial lipids, acylcarnitines, sphingolipids, and cholesterol-
595 associated species.

596 **ACLY inhibition induces metabolic remodeling, integrated stress response, redox stress, apoptosis,**
597 **and immune regulation**

598 To define the transcriptional consequences of VCB1-mediated ACLY inhibition, DEGs associated with
599 lipid metabolism were identified using a log2 FC ≥0.5 threshold and NIH-DAVID/KEGG pathway analysis.
600 VCB1, but not BMS-303141 at the same concentration, significantly altered lipid-metabolic pathways and
601 enzymes (Fig. 8A). These findings prompted analysis of the integrated stress response (ISR), which couples
602 translational control to metabolic and amino-acid adaptation through eIF2α kinase signaling(47-51). VCB1
603 induced a prominent ISR-associated transcriptional response in both ALKi-sensitive and -resistant cells,
604 including *ATF4, ATF3, SESN2, DDIT4, HILPDA, TRIB3, DDIT3, PPP1R15A,* and *CHAC1* (log2 FC +2.3
605 and +1.8 in S-VCB1 and SLR-VCB1), whereas ASNS was additionally induced only in sensitive cells (log2
606 FC = 1.25) and *BNIP3* (log2 FC +2.0 and +1.6) and *BNIP3L* (log2 FC +1.6 and +1.7) indicated
607 mitochondrial stress adaptation (Fig. 8B). VCB1 induced *BNIP3L* mRNA expression results showed
608 impaired lipid synthesis. Similarly, in another study confirmed *BNIP3L* protein, was significantly reduced
609 in patients with Diabetic cardiomyopathy compared to those with non-diabetic(52). BMS-303141 produced
610 no significant ISR-associated transcriptional response at 1 μM, although activation of the p-
611 eIF2α/ATF4/CHOP pathway has been reported at higher concentrations in hepatocellular carcinoma(53).
612 Furthermore, our results demonstrated a conserved ISR with distinct downstream stress-adaptation
613 programs in SUPM2 and SLR cells. RT-PCR confirmed VCB1-induced changes in *PPP1R15A/GADD34,*
614 *NLRP3,* and *CHAC1* observed by RNA-seq data (Fig. 8C-E). *PPP1R15A/GADD34* is a key regulator of
615 ISR termination(54), whereas CHAC1 promotes glutathione degradation and contributes to oxidative stress
616 and cell death(55). Consistent with this response, VCB1 increased CHAC1 by +2.26 and +1.77 log2 FC in
617 sensitive and resistant cells (Fig. 8E). Metabolomics analysis demonstrated corresponding disruption of

618 glutathione homeostasis, with reduced GSH and GSSG and a significantly decreased GSH/GSSG ratio
619 following VCB1 treatment, whereas BMS-303141 produced no significant change (Fig. 8F). VCB1 also
620 decreased γ-glutamylcysteine and S-lactoylglutathione (Fig. 8G-H). Thus, VCB1 treatment showed
621 concordant transcriptional and metabolic evidence of impaired glutathione homeostasis, supporting an
622 ACLY–ISR–CHAC1 axis linking metabolic stress to redox imbalance. Consistent with activation of cell-
623 death pathways, VCB1 also increased apoptosis/stress-associated genes including *ATF4, GADD45A,*
624 *GADD45B, DDIT3, DDIT4, GZMA, TRAF1,* and *TNF* (Fig. 8I). VCB1 also induced inflammatory and
625 immune-regulatory remodeling. *NLRC5* was reduced, whereas *NLRP1* and *NLRP3* were increased in both
626 sensitive and resistant cells, with strong *NLRP3* induction in the resistant state (Fig. 8J). The activating
627 immune receptor *CD226* increased in sensitive (+1.49 log2 FC) and resistant (+0.67 log2 FC) cells, while
628 *PDCD1* (PD-1) particularly increased in resistant cells (+1.19 log2 FC). *PDCD4* was also induced (+0.89
629 log2 FC), accompanied by increased *EIF4EBP1* and reduced *EIF4A1*, consistent with suppression of
630 eIF4A-dependent translation during metabolic stress. Although PD-L1 was not differentially expressed in
631 our RNA-seq dataset, previous studies reported increased PD-L1 following ACLY inhibition by bempedoic
632 acid or genetic ACLY knockdown(56). Together, these findings indicate that ACLY inhibition alters
633 inflammatory, immune-checkpoint, and translational regulatory pathways. The relationship between
634 *PDCD1* and *NLRP3* involved in ISR, and ER stress further supports a link between metabolic stress and
635 immune regulation(57). Finally, integration of VCB1-responsive RNA-seq and metabolomics data using
636 MetaboAnalyst 6.0 identified significant gene-metabolite interactions involving lipid metabolic pathways
637 in sensitive cells (Fig. 8K), with a corresponding network observed in resistant cells (Supplementary Fig.
638 7). The integrated model summarizes VCB1-mediated ACLY inhibition as a coordinated response
639 involving altered central-carbon metabolism, glycolytic and amino-acid metabolic genes (*PFKFB3/4,*
640 *ENO2, ASNS*), suppression of ACLY-dependent lipogenesis (*ACACA, FASN*), and lipid-remodeling
641 pathways (*HILPDA, DGKG*), accompanied by lipid-species remodeling, ISR activation, glutathione/redox
642 stress, apoptosis, and inflammatory and T-cell regulatory signaling (Fig. 8L).

643 **VCB1 shows potent antiproliferative activity in tyrosine kinase inhibitor-resistant lymphoma**

644 We next evaluated the antiproliferative activity of VCB1, VCB2, VCB7, and BMS-303141 in SUPM2
645 parental and lorlatinib-resistant SUPM2-LR1000 cells. Cells were treated with increasing concentrations
646 of each compound for 72 h in 5% FBS. VCB1 showed the strongest growth-inhibitory activity in SUPM2
647 parental cells, with an IC50 of 0.299 μM, compared with 22.0 μM for VCB2, 1.21 μM for VCB7, and 17.46
648 μM for BMS. In SLR cells, VCB1 retained substantial activity, although its potency was reduced, with an
649 IC50 of 1.62 μM. VCB2, VCB7, and BMS showed IC50 values of 9.98, 3.60, and 22.07 μM, respectively
650 (Fig. 9A, B). VCB1 also displayed potent activity in MCL models. In Jeko-1 and Maver cells, VCB1
651 showed IC50 values of 0.28 and 0.278 μM, respectively. In contrast, VCB2 showed IC50 values of 15.0
652 and 10.4 μM, VCB7 showed values of 2.26 and 1.84 μM, and BMS showed substantially weaker activity,
653 with IC50 values of 30.5 and 37.01 μM, respectively (Fig. 9C, D). Thus, VCB1 was consistently the most
654 potent compound tested and retained activity in lymphoma models with acquired resistance to ALK or BTK
655 inhibition. These findings indicate that ACLY inhibition represents a therapeutically distinct vulnerability
656 that can be maintained despite resistance to kinase-targeted therapy. Next, we investigated the RNA-seq
657 data to determine whether the transcriptional and metabolic alterations translated into functional effects on
658 proliferation, we examined cell-cycle progression related DEGs in cells treated with VCB1. The results
659 showed significant changes in both ALKi sensitive and resistant cell lines (Fig.9E). Further, we performed
660 cell cycle analysis on these cell lines treated with 0.5 μM VCB1 for 48 h resulted in significant accumulation
661 of cells in the G0/G1 phase compared with BMS-treated cells (Fig. 9F–H). These findings are consistent
662 with the RNA-seq suppression of CCNB1, CDC20, PLK1, CENPE, CENPF, KIF20A, KIF23, and PTTG1
663 and induction of cell-cycle checkpoint genes such as CDKN1A, GADD45A, and BTG2. Because
664 metabolomics revealed substantial disruption of pyrimidine metabolism, we examined key enzymes within
665 this pathway. RNA-seq demonstrated reduced expression of DHODH and CAD following VCB1 treatment,
666 (Fig. 9I, J). RNA-seq further demonstrated coordinated disruption of pyrimidine biosynthesis DEGs
667 following VCB1, whereas BMS produced substantially weaker changes (Fig. 9K). Further analysis on

668 RNA-seq identified DEGs involved in phospholipid, LPCAT1 (Fig.9L), cholesterol synthesis pathway
669 DEGs, HMGCR, INSIG1 and INSIG2 (Fig.9L-O). In summary, Integration of RNA-seq and metabolomic
670 datasets further demonstrated coordinated disruption of pyrimidine biosynthesis following VCB1, whereas
671 BMS produced substantially weaker changes (Fig. 9P). Together, these findings indicate that VCB1-
672 mediated ACLY inhibition disrupts interconnected lipid, nucleotide, central-carbon, redox, and stress
673 pathways, resulting in cell-cycle arrest and ultimately apoptotic cell death.

674 **Discussion**

675 ACLY occupies a central metabolic position by converting citrate to cytosolic acetyl-CoA, thereby linking
676 glucose-derived carbon to fatty-acid and cholesterol synthesis. However, therapeutic targeting of ACLY
677 remains challenging. Bempedoic acid (also known as ETC-1002) has been recently approved by U.S. Food
678 and Drug Administration (FDA) for lowering low-density lipoprotein cholesterol(27, 58). Bempedoic acid
679 targeting ACLY- requires activation by SLC27A2/ACSVL1, is predominantly active in the liver, and
680 activates AMPK pathway(59, 60). Like this other ACLY inhibitor, EVT0185 shows anticancer activity but
681 requires metabolic activation and has additional activity against ACSS2(60, 61). In our studies, the
682 reference ACLY inhibitor BMS-303141 inhibited recombinant ACLY but showed limited cellular activity
683 in ALCL and MCL models. These limitations highlight the need for potent, selective, cell-active ACLY
684 inhibitors.

685 Building on our previous demonstration that NPM-ALK phosphorylates ACLY at Y682 to promote lipid
686 metabolism and ALCL progression(6, 30, 31) and that ACLY is regulated downstream of the
687 PI3K/PIP2/PIP3–LYN axis(32), we identified VCB1 as a novel, cell-active ACLY inhibitor. Our xenograft
688 findings provide genetic *in-vivo* evidence supporting the role of ACLY in ALK-positive ALCL tumor
689 establishment. Although ACLY is an established regulator of cancer metabolism and tumor growth, genetic
690 validation of ACLY dependence in lymphoma xenograft models remains limited. In the SU-DHL-1 model,
691 control cells eventually established substantial tumors, whereas ACLY-depleted cells failed to produce
692 detectable tumors during the observation period. Thus, ACLY depletion was associated with a marked

693 impairment of tumor establishment rather than simply a modest reduction in tumor growth and provide a
694 rationale for pharmacologic targeting of ACLY in ALK-positive ALCL. We subsequently evaluated our
695 novel ACLY inhibitor VCB1 in the paired SUP-M2 parental and lorlatinib-resistant SUP-M2-LR1000
696 models, which provided a common cellular background for investigating ACLY inhibition across ALK-
697 inhibitor-sensitive and resistant states and for subsequent transcriptomic, metabolomic, and lipidomic
698 analyses. VCB1 inhibited recombinant ACLY with an IC_{50} of ~0.9 μM and exhibited potent
699 antiproliferative activity in ALK+ lymphoma, including TKI-resistant ALCL and BTK inhibitor-resistant
700 MCL models. In SUPM2 cells, VCB1 showed a growth IC_{50} of 0.299 μM and induced apoptosis, whereas
701 BMS-303141 displayed substantially weaker cellular activity. Notably, BMS-303141 has generally been
702 evaluated at relatively high micromolar concentrations in published cellular studies, including 10 μM in B-
703 ALL(62), 5–15 μM in T-cell lymphoma(63), 10 μM in T-ALL(18), breast cancer(64), prostate cancer(12),
704 and 25–50 μM in osteosarcoma models(53, 65). Similarly, the classical ACLY inhibitor SB-204990(22,
705 66) has generally required 10–100 μM concentrations in cellular studies, including 30 μM in HepG2 cells,
706 25 μM in human macrophages, 10–30 μM in ovarian cancer, 10–20 μM in lung cancer, 40 μM in KRAS-
707 driven HCT116 cells, and 100 μM in pancreatic β-cells and other models(67). Although differences in
708 permeability, intracellular exposure, and experimental systems preclude direct potency comparisons, VCB1
709 produced a growth IC_{50} of 0.299 μM in SUPM2 cells and robust apoptotic signaling at 1 μM, supporting its
710 characterization as a highly cell-active ACLY inhibitor and providing a rationale for further development
711 in TKI-resistant lymphoma.

712 VCB1-mediated ACLY inhibition extended beyond de novo lipogenesis. Suppression of ACACA, FASN,
713 HMGCR, and PPARGC1B, together with changes in SLC27A4 and CPT1A, was accompanied by
714 induction of metabolic-adaptation genes including PPARA, ACADS, ACADVL, HMGCL, LPL, LDLR,
715 VLDLR, and OSBPL5. PPARGC1B, encoding PGC-1β, regulates lipid and energy metabolism through
716 SREBP and ChREBP(68) and has been implicated in glycolytic regulation and tumor-supportive
717 macrophage phenotypes(69). PPARGC1B stronger downregulation in resistant cells (−2.5 versus −0.75

718 log2 FC in sensitive cells) is consistent with impaired mitochondrial and oxidative metabolic programs,
719 similar observations in ACLY knockdown conditions(70). Hallmark analysis further identified activation
720 of glycolytic and metabolic-stress programs, including SLC2A1, SLC2A3, PDK1, PGK1, PFKFB4, CA9,
721 DDIT4, BNIP3L, and HILPDA. Together with changes in acetyl-CoA, citrate, acetylcarnitines, and TCA
722 intermediates, these findings indicate that ACLY inhibition induces broad metabolic rewiring rather than
723 simply suppressing fatty-acid synthesis.

724

725 Integrated transcriptomic, metabolomic, and lipidomic analyses revealed that SUPM2 and SLR lymphoma
726 cells share a core response to ACLY inhibition but engage distinct metabolic adaptations. Thus, SLR
727 appears to represent metabolic rewiring that changes how cells respond to ACLY blockade rather than
728 simply a generalized increase in metabolism. In SUPM2 cells, VCB1 predominantly induced an acute
729 biosynthetic and metabolic-stress response involving glycolysis, lipid metabolism, amino-acid metabolism,
730 and mTOR/AMPK signaling. Suppression of ACACA, FASN, HMGCR, CS, DLAT, and PPARGC1B
731 together with induction of PFKFB4 and PFKL suggests increased reliance on alternative energy-generating
732 pathways following loss of ACLY-derived acetyl-CoA. In contrast, SLR cells exhibited more extensive
733 metabolic remodeling, including increased expression of genes associated with glucose and glutamine
734 utilization, lipid uptake and storage, cholesterol metabolism, and fatty-acid utilization, including LDLR,
735 APOC1, DGAT2, FADS2, and DHCR24, while mitochondrial, TCA-cycle, fatty-acid, and nucleotide
736 metabolic programs were broadly suppressed. Importantly, sensitive and resistant cells shared induction of
737 the integrated stress response (ISR), including ATF4, ATF3, DDIT3/CHOP, DDIT4, SESN2, TRIB3,
738 PPP1R15A, and CHAC1. Thus, despite distinct basal metabolic states, both populations recognize effective
739 ACLY inhibition as metabolic stress and activate a conserved ISR. This is consistent with the established
740 role of ATF4 as a central ISR effector coordinating amino-acid, redox, and metabolic adaptation and
741 inducing CHAC1-dependent glutathione depletion. In previous studies by others showed that ATF4 also
742 regulates nucleotide synthesis and DNA replication in leukemia cells(71).

743 The conserved ISR produced distinct downstream adaptations. Sensitive cells showed greater acute
744 ER/UPR and metabolic-stress responses, whereas resistant cells exhibited stronger PERK–ATF4,
745 glutathione/redox, autophagy, and apoptotic programs. This suggests that the consequences of ACLY
746 inhibition are shaped by pre-existing metabolic state. In resistant cells, extensive metabolic flexibility may
747 permit survival following kinase inhibition but simultaneously limit compensation for disruption of lipid
748 synthesis, mitochondrial metabolism, and redox homeostasis. Lipidomics analysis further demonstrated
749 that VCB1 does not simply suppress lipid production but reorganizes lipid metabolism and membrane
750 composition. VCB1 altered triglycerides, phospholipids, cholesteryl esters, sphingolipids, cardiolipins, and
751 acylcarnitines, with changes in DGK, GPAT, LPCAT, PLD, CHKA/E, PTDSS1, CDS, and DGAT2
752 indicating remodeling across multiple lipid pathways. Ceramide and hexosylceramide accumulation in both
753 cellular states, together with cardiolipin and phosphatidylglycerol alterations and increased acylcarnitines,
754 suggests disruption of mitochondrial lipid homeostasis. These findings extend previous observations
755 linking ACLY inhibition to mitochondrial dysfunction, including impaired membrane potential and
756 oxidative phosphorylation(21, 72). A particularly important, shared consequence was disruption of
757 glutathione homeostasis. CHAC1 was strongly induced in sensitive (+2.26 log2 FC) and resistant (+1.77
758 log2 FC) cells, accompanied by reduced γ-glutamylcysteine, glutathione, and GSH/GSSG ratio. Because
759 ATF4 can induce CHAC1 and promote GSH degradation, these findings provide a mechanistic link
760 between the ISR and redox stress, supporting an ACLY–ISR–CHAC1–redox axis as a potential mechanism
761 underlying oxidative vulnerability following ACLY inhibition. VCB1 also disrupted nucleotide
762 metabolism. Metabolomics revealed depletion or alteration of AMP, dAMP, dADP, UMP, TMP, cytosine,
763 GMP, IMP, GTP, CMP, and CTP, accompanied by transcriptional changes in CAD, DHODH, PPAT,
764 GMPS, ADSL, ATIC, CTPS, and UMPS. Reduced aspartate and altered orotic acid and orotidine further
765 support impaired de novo pyrimidine synthesis. The convergence of transcriptional and metabolite changes
766 indicates that ACLY inhibition disrupts nucleotide supply in addition to lipid synthesis, potentially limiting
767 the biosynthetic capacity of rapidly proliferating lymphoma cells. Consistent with this, VCB1 induced
768 G0/G1 accumulation and increased CDKN1A, GADD45A, and BTG2 while suppressing proliferation-

769 associated genes. Thus, VCB1-mediated growth inhibition likely reflects coordinated disruption of lipid,
770 nucleotide, and redox homeostasis rather than lipogenesis blockade alone. Lipid metabolism also influences
771 immune-cell function and innate and adaptive immune responses(73). In this context, VCB1 induced
772 inflammatory and stress-associated genes in both cell lines, including increased NLRP1 and NLRP3 and
773 reduced NLRC5, with particularly strong NLRP3 induction in resistant cells (+2.50 log2 FC). Because
774 NLRP3 responds to metabolic and cellular stress, its greater induction may reflect the increased metabolic
775 burden of resistant cells, although its contribution to VCB1-mediated cytotoxicity remains to be established.
776 Changes in PDCD4, CD226, and PDCD1 (PD-1), together with altered EIF4-associated factors, further
777 indicate translational and immune-associated remodeling. The results showed that VCB1 induced PD-1
778 expression in SLR cells (+1.2 log2 FC). The previous study showed that the association of PD-1 signaling
779 suppressing ACLY-acetyl-CoA production and acts as tumor suppressor(63). Similarly, VCB1 treatment
780 consistently induced PDCD4 level (+0.89 log2 FC), accompanied by increased EIF4EBP1 and reduced
781 EIF4A1, supporting suppression of protein synthesis during metabolic stress. PDCD4 is a recognized tumor
782 suppressor involved in translational control, apoptosis, and inflammatory signaling(74, 75), and its loss
783 promotes B-cell lymphoma development in mice(76). Translational repression may therefore reinforce the
784 ISR-associated reduction in anabolic growth. These findings support a model in which ACLY inhibition
785 produces a conserved core stress response superimposed on distinct metabolic programs determined by TKI
786 sensitivity or resistance. Common VCB1-responsive DEGs reflect suppression of anabolic metabolism,
787 activation of the ATF4/ATF3/CHOP ISR, CHAC1-associated glutathione depletion, inflammatory
788 signaling, and translational repression. In contrast, sensitivity-specific responses reflect acute biosynthetic
789 and metabolic stress, whereas resistance-specific responses reveal compensatory dependence on glycolysis,
790 glutamine utilization, exogenous lipid acquisition, fatty-acid utilization, and redox metabolism. Thus, TKI
791 resistance appears to be remodeled rather than simply increasing cellular metabolism. This rewiring may
792 permit survival during kinase inhibition while constraining the capacity of resistant lymphoma cells to
793 compensate for ACLY blockade. VCB1 therefore targets a metabolic node that remains important despite
794 loss of kinase dependence, while resistance-associated adaptations may create additional vulnerabilities.

795 The shared ISR/redox stress together with resistance-specific metabolic dependence provides a mechanistic
796 framework for ACLY inhibition as a resistance-bypass strategy in lymphoma.

797 **Conclusion**

798 Collectively, our findings extend the biological consequences of ACLY inhibition beyond lipid synthesis.
799 We identify VCB1 as a novel, cell-active ACLY inhibitor with sub micromolar antiproliferative activity in
800 TKI-sensitive lymphoma cells (IC_{50} = 0.299 μM) and retained activity against lorlatinib-resistant cells (IC_{50}
801 1.62 μM), whereas BMS-303141 showed limited cellular activity in our models. Integrated transcriptomic,
802 metabolomic, and lipidomic analyses demonstrate that VCB1 induces broad metabolic remodeling
803 involving lipid and nucleotide metabolism, mitochondrial homeostasis, and redox balance. VCB1 also
804 activates a robust ISR characterized by ATF4-associated stress genes, including CHAC1, ATF3, DDIT3,
805 DDIT4, SESN2, and TRIB3. Notably, the stronger transcriptional response in TKI-resistant cells suggests
806 that resistance-associated metabolic rewiring may increase dependence on ACLY-linked metabolic
807 programs. Together, these findings define an ACLY–nucleotide metabolism–ISR axis connecting
808 metabolic disruption with impaired biosynthetic and redox homeostasis and support ACLY inhibition,
809 particularly with cell-active compounds such as VCB1, as a potential therapeutic strategy for TKI-resistant
810 lymphoma.

811 **Acknowledgments**

812 We thank the Proteomics and Metabolomics Shared Resource at the Wistar Institute, Philadelphia, for
813 providing metabolomics and proteomics analysis services and for their support. The figures in this
814 manuscript were created using the Biorender program. L.M., is supported by Italian Association for Cancer
815 Research grant n. 24828 funding. H.Y.T is supported by R50CA221838. Funding support for The Wistar
816 Institute's Proteomics and Metabolomics Shared Resource was provided by Cancer Center Support Grant
817 P30 CA010815. No NIH or other US federal funds were used to support co-authors with foreign affiliations.

818

819 **Author Contributions**

820 J.B. conceived the project, designed and performed the research, analyzed the data, supervised the project,
821 and wrote the manuscript. N.P., in-silico screening of ACLY inhibitors, performed molecular docking. C.L.,
822 D.R., and S.W., investigation, A.R.G. and W.Z., conducted metabolomics and lipidomics and data analysis.
823 L.M., H.B., resources., K.N. contributed to xenograft study, R.N. contributed to the resources and M.W.
824 obtained funding and provided resources. All authors have approved the manuscript and agree with its
825 submission.

826 **Ethics declarations:** Not applicable

827 **Funding declaration**: This research received no external funding.

828 **Competing interests**

829 The provisional U.S. patent application No. 63/870,711, Title, **ACLY INHIBITORS AND USES**
830 **THEREOF** has been filed, listing N.P. and J.B. as the inventors.

831 **References:**

832 1. Wellen KE, Hatzivassiliou G, Sachdeva UM, Bui TV, Cross JR, Thompson CB. ATP-Citrate Lyase Links
833 Cellular Metabolism to Histone Acetylation. Science. 2009;324(5930):1076-80.
834 2. Icard P, Wu Z, Fournel L, Coquerel A, Lincet H, Alifano M. ATP citrate lyase: A central metabolic
835 enzyme in cancer. Cancer Lett. 2020;471:125-34.
836 3. Zaidi N, Swinnen JV, Smans K. ATP-citrate lyase: a key player in cancer metabolism. Cancer Res.
837 2012;72(15):3709-14.
838 4. Potapova IA, El-Maghrabi MR, Doronin SV, Benjamin WB. Phosphorylation of recombinant human
839 ATP : citrate lyase by cAMP-dependent protein kinase abolishes homotropic allosteric regulation of the
840 enzyme by citrate and increases the enzyme activity. Allosteric activation of ATP : citrate lyase by
841 phosphorylated sugars. Biochemistry-Us. 2000;39(5):1169-79.
842 5. Basappa J, Citir M, Zhang Q, Wang HY, Liu XB, Melnikov O, et al. ACLY is the novel signaling target
843 of PIP2/PIP3 and Lyn in acute myeloid leukemia. Heliyon. 2020;6(5).
844 6. Basappa J, ElAzzouny MA, Rolland DCM, Sahasrabuddhe AA, Ma K, Bazilevsky GA, et al. Tyrosine
845 phosphorylation is critical for ACLY activity in lipid metabolism and cancer. bioRxiv.
846 2020:2020.01.20.910752.
847 7. Xie Z, Zhang M, Song Q, Cheng L, Zhang X, Song G, et al. Development of the novel ACLY inhibitor
848 326E as a promising treatment for hypercholesterolemia. Acta Pharm Sin B. 2023;13(2):739-53.
849 8. Morrow MR, Batchuluun B, Wu J, Ahmadi E, Leroux JM, Mohammadi-Shemirani P, et al. Inhibition
850 of ATP-citrate lyase improves NASH, liver fibrosis, and dyslipidemia. Cell Metab. 2022;34(6):919-36 e8.

851 9. Convertini P, Santarsiero A, Todisco S, Gilio M, Palazzo D, Pappalardo I, et al. ACLY as a modulator
852 of liver cell functions and its role in Metabolic Dysfunction-Associated Steatohepatitis. J Transl Med.
853 2023;21(1):568.
854 10. Migita T, Narita T, Nomura K, Miyagi E, Inazuka F, Matsuura M, et al. ATP Citrate Lyase: Activation
855 and Therapeutic Implications in Non-Small Cell Lung Cancer. Cancer Research. 2008;68(20):8547-54.
856 11. Chen Y, Li K, Gong D, Zhang J, Li Q, Zhao G, et al. ACLY: A biomarker of recurrence in breast cancer.
857 Pathol Res Pract. 2020;216(9):153076.
858 12. Shah S, Carriveau WJ, Li J, Campbell SL, Kopinski PK, Lim HW, et al. Targeting ACLY sensitizes
859 castration-resistant prostate cancer cells to AR antagonism by impinging on an ACLY-AMPK-AR feedback
860 mechanism. Oncotarget. 2016;7(28):43713-30.
861 13. Wang Y, Su K, Wang C, Deng T, Liu X, Sun S, et al. Chemotherapy-induced acetylation of ACLY by
862 NAT10 promotes its nuclear accumulation and acetyl-CoA production to drive chemoresistance in
863 hepatocellular carcinoma. Cell Death Dis. 2024;15(7):545.
864 14. Carrer A, Trefely S, Zhao S, Campbell SL, Norgard RJ, Schultz KC, et al. Acetyl-CoA Metabolism
865 Supports Multistep Pancreatic Tumorigenesis. Cancer Discov. 2019;9(3):416-35.
866 15. Wen J, Min X, Shen M, Hua Q, Han Y, Zhao L, et al. ACLY facilitates colon cancer cell metastasis by
867 CTNNB1. J Exp Clin Cancer Res. 2019;38(1):401.
868 16. Greenwood DL, Ramsey HE, Nguyen PTT, Patterson AR, Voss K, Bader JE, et al. Acly Deficiency
869 Enhances Myelopoiesis through Acetyl Coenzyme A and Metabolic-Epigenetic Cross-Talk.
870 Immunohorizons. 2022;6(12):837-50.
871 17. Andrieu GP, Hypolite G, Latiri M, Balducci E, Costa C, Verhoeyen E, et al. ATP citrate lyase is an
872 essential player in the metabolic rewiring induced by PTEN loss during T-ALL development. Blood Adv.
873 2025;9(7):1670-91.
874 18. da Silva-Diz V, Singh A, Aleksandrova M, Kim O, Thai C, Lancho O, et al. A feedforward loop
875 between ACLY and MYC supports T-ALL progression in vivo. Blood Neoplasia. 2025;2(2):100069.
876 19. Wang J, Ye W, Yan X, Guo Q, Ma Q, Lin F, et al. Low expression of ACLY associates with favorable
877 prognosis in acute myeloid leukemia. J Transl Med. 2019;17(1):149.
878 20. Hatzivassiliou G, Zhao FP, Bauer DE, Andreadis C, Shaw AN, Dhanak D, et al. ATP citrate lyase
879 inhibition can suppress tumor cell growth. Cancer Cell. 2005;8(4):311-21.
880 21. Hatzivassiliou G, Zhao F, Bauer DE, Andreadis C, Shaw AN, Dhanak D, et al. ATP citrate lyase
881 inhibition can suppress tumor cell growth. Cancer Cell. 2005;8(4):311-21.
882 22. Pearce NJ, Yates JW, Berkhout TA, Jackson B, Tew D, Boyd H, et al. The role of ATP citrate-lyase in
883 the metabolic regulation of plasma lipids. Hypolipidaemic effects of SB-204990, a lactone prodrug of the
884 potent ATP citrate-lyase inhibitor SB-201076. Biochem J. 1998;334 (Pt 1)(Pt 1):113-9.
885 23. Ma Z, Chu CH, Cheng D. A novel direct homogeneous assay for ATP citrate lyase. J Lipid Res.
886 2009;50(10):2131-5.
887 24. Wei J, Leit S, Kuai J, Therrien E, Rafi S, Harwood HJ, Jr., et al. An allosteric mechanism for potent
888 inhibition of human ATP-citrate lyase. Nature. 2019;568(7753):566-70.
889 25. Liang JJ, Zhou XF, Long H, Li CY, Wei J, Yu XQ, et al. Recent advance of ATP citrate lyase inhibitors
890 for the treatment of cancer and related diseases. Bioorg Chem. 2024;142:106933.
891 26. Thompson PD, Rubino J, Janik MJ, MacDougall DE, McBride SJ, Margulies JR, et al. Use of ETC-
892 1002 to treat hypercholesterolemia in patients with statin intolerance. J Clin Lipidol. 2015;9(3):295-304.
893 27. Nissen SE, Lincoff AM, Brennan D, Ray KK, Mason D, Kastelein JJP, et al. Bempedoic Acid and
894 Cardiovascular Outcomes in Statin-Intolerant Patients. N Engl J Med. 2023;388(15):1353-64.
895 28. Gautam J, Wu J, Lally JSV, McNicol JD, Fayyazi R, Ahmadi E, et al. ACLY inhibition promotes tumour
896 immunity and suppresses liver cancer. Nature. 2025.
897 29. Verschueren KHG, Blanchet C, Felix J, Dansercoer A, De Vos D, Bloch Y, et al. Structure of ATP
898 citrate lyase and the origin of citrate synthase in the Krebs cycle. Nature. 2019;568(7753):571-5.

30. Basappa J, ElAzzouny MA, Rolland DC, Velusamy T, Hwang S, Basrur V, et al. NPM-ALK Mediated Tyrosine Phosphorylation of ATP Citrate Lyase Regulates Lipid Metabolism and Promotes Oncogenesis of Anaplastic Large Cell Lymphoma. Blood. 2015;126(23):465-.
31. Pattabiraman N, Lobello C, Rushmore D, Nejati R, Mologni L, Wasik M, et al. Structure-guided discovery of potent acly inhibitors with therapeutic potential in ALK plus anaplastic large cell lymphoma and other hematologic malignancies. Blood. 2025;146:6815-.
32. Basappa J, Citir M, Zhang Q, Wang HY, Liu X, Melnikov O, et al. ACLY is the novel signaling target of PIP(2)/PIP(3) and Lyn in acute myeloid leukemia. Heliyon. 2020;6(5):e03910.
33. Ceccon M, Mologni L, Bisson W, Scapozza L, Gambacorti-Passerini C. Crizotinib-resistant NPM-ALK mutants confer differential sensitivity to unrelated Alk inhibitors. Mol Cancer Res. 2013;11(2):122-32.
34. Pattabiraman N, Lobello C, Rushmore D, Mologni L, Wasik M, Basappa J. A Novel Allosteric Inhibitor Targeting IMPDH at Y233 Overcomes Resistance to Tyrosine Kinase Inhibitors in Lymphoma. Cancers (Basel). 2025;17(20).
35. Basappa J, Goldman AR, Lobello C, Wang S, Rushmore D, Melnikov O, et al. Mitochondrial ACSS1 links acetate metabolism to pyrimidine biosynthesis in nutrient-stressed B-cell lymphomas. Cancer Lett. 2026;649:218488.
36. Di Marcantonio D, Martinez E, Kanefsky JS, Huhn JM, Gabbasov R, Gupta A, et al. ATF3 coordinates serine and nucleotide metabolism to drive cell cycle progression in acute myeloid leukemia. Mol Cell. 2021;81(13):2752-64 e6.
37. Li J, Agarwal E, Bertolini I, Seo JH, Caino MC, Ghosh JC, et al. The mitophagy effector FUNDC1 controls mitochondrial reprogramming and cellular plasticity in cancer cells. Sci Signal. 2020;13(642).
38. Lombardi S, Goldman AR, Tang HY, Kossenkov AV, Liu H, Zhou W, et al. Targeting Fatty Acid Reprogramming Suppresses CARM1-expressing Ovarian Cancer. Cancer Res Commun. 2023;3(6):1067-77.
39. Zaidi N, Royaux I, Swinnen JV, Smans K. ATP citrate lyase knockdown induces growth arrest and apoptosis through different cell- and environment-dependent mechanisms. Mol Cancer Ther. 2012;11(9):1925-35.
40. da Silva-Diz V, Singh A, Aleksandrova M, Kim O, Thai C, Lancho O, et al. Therapeutic targeting of ACLY in T-ALL in vivo. bioRxiv. 2024.
41. Huang da W, Sherman BT, Zheng X, Yang J, Imamichi T, Stephens R, et al. Extracting biological meaning from large gene lists with DAVID. Curr Protoc Bioinformatics. 2009;Chapter 13:Unit 13 1.
42. Wellen KE, Hatzivassiliou G, Sachdeva UM, Bui TV, Cross JR, Thompson CB. ATP-citrate lyase links cellular metabolism to histone acetylation. Science. 2009;324(5930):1076-80.
43. Zhao S, Torres A, Henry RA, Trefely S, Wallace M, Lee JV, et al. ATP-Citrate Lyase Controls a Glucose-to-Acetate Metabolic Switch. Cell Rep. 2016;17(4):1037-52.
44. Chen Q, Du J, Cui K, Fang W, Zhao Z, Chen Q, et al. Acetyl-CoA derived from hepatic mitochondrial fatty acid beta-oxidation aggravates inflammation by enhancing p65 acetylation. iScience. 2021;24(11):103244.
45. Kaymak I, Watson MJ, Oswald BM, Ma S, Johnson BK, DeCamp LM, et al. ACLY and ACSS2 link nutrient-dependent chromatin accessibility to CD8 T cell effector responses. J Exp Med. 2024;221(9).
46. Pang Z, Lu Y, Zhou G, Hui F, Xu L, Viau C, et al. MetaboAnalyst 6.0: towards a unified platform for metabolomics data processing, analysis and interpretation. Nucleic Acids Res. 2024;52(W1):W398-W406.
47. Ben-Sahra I, Hoxhaj G, Ricoult SJH, Asara JM, Manning BD. mTORC1 induces purine synthesis through control of the mitochondrial tetrahydrofolate cycle. Science. 2016;351(6274):728-33.
48. Donnelly N, Gorman AM, Gupta S, Samali A. The eIF2alpha kinases: their structures and functions. Cell Mol Life Sci. 2013;70(19):3493-511.
49. Labbe K, LeBon L, King B, Vu N, Stoops EH, Ly N, et al. Specific activation of the integrated stress response uncovers regulation of central carbon metabolism and lipid droplet biogenesis. Nat Commun. 2024;15(1):8301.

947 50. Ryoo HD. The integrated stress response in metabolic adaptation. J Biol Chem.
948 2024;300(4):107151.
949 51. Thomas-Jardin S, Suresh S, Arce A, Novaresi N, Deng Q, Stein E, et al. The Integrated Stress
950 Response Pathway Coordinates Translational Control of Multiple Immune Checkpoints in Lung Cancer.
951 Cancer Res. 2025;85(14):2574-90.
952 52. Lu Q, Tang S, Fang S, Wu Y, Chen L, Liang M, et al. Multi-omics profiling of the diabetic human
953 heart reveals coupled dysregulation in lipid metabolism, mitophagy, and extracellular matrix remodeling.
954 Genome Med. 2026;18(1).
955 53. Zheng Y, Zhou Q, Zhao C, Li J, Yu Z, Zhu Q. ATP citrate lyase inhibitor triggers endoplasmic
956 reticulum stress to induce hepatocellular carcinoma cell apoptosis via p-eIF2alpha/ATF4/CHOP axis. J Cell
957 Mol Med. 2021;25(3):1468-79.
958 54. Oliveira MM, Mohamed M, Elder MK, Banegas-Morales K, Mamcarz M, Lu EH, et al. The integrated
959 stress response effector GADD34 is repurposed by neurons to promote stimulus-induced translation. Cell
960 Rep. 2024;43(2):113670.
961 55. Sun J, Ren H, Wang J, Xiao X, Zhu L, Wang Y, et al. CHAC1: a master regulator of oxidative stress
962 and ferroptosis in human diseases and cancers. Front Cell Dev Biol. 2024;12:1458716.
963 56. Xiang W, Lv H, Xing F, Sun X, Ma Y, Wu L, et al. Inhibition of ACLY overcomes cancer
964 immunotherapy resistance via polyunsaturated fatty acids peroxidation and cGAS-STING activation. Sci
965 Adv. 2023;9(49):eadi2465.
966 57. Jia H, Ma L, Liu J, Gao M, Liang X, Zhang F, et al. Organelle stress in NLRP3 inflammasome: a central
967 mediator of neurodegenerative diseases. Mol Neurodegener. 2026;21(1):8.
968 58. Ray KK, Bays HE, Catapano AL, Lalwani ND, Bloedon LT, Sterling LR, et al. Safety and Efficacy of
969 Bempedoic Acid to Reduce LDL Cholesterol. N Engl J Med. 2019;380(11):1022-32.
970 59. Pinkosky SL, Newton RS, Day EA, Ford RJ, Lhotak S, Austin RC, et al. Liver-specific ATP-citrate lyase
971 inhibition by bempedoic acid decreases LDL-C and attenuates atherosclerosis. Nat Commun.
972 2016;7:13457.
973 60. Gautam J, Wu J, Lally JSV, McNicol JD, Fayyazi R, Ahmadi E, et al. ACLY inhibition promotes tumour
974 immunity and suppresses liver cancer. Nature. 2025;645(8080):507-17.
975 61. Di Pastena F, Gautam J, Lally JSV, Fayyazi R, Grasset E, Bhattacharya D, et al. Dual inhibition of
976 ACLY and ACSS2 by EVT0185 reduces steatosis, hepatic stellate cell activation, and fibrosis in mouse
977 models of MASH. Cell Metab. 2026;38(1):33-49 e10.
978 62. Piktel D, Nair RR, Rellick SL, Geldenhuys WJ, Martin KH, Craig MD, et al. Pitavastatin Is Anti-
979 Leukemic in a Bone Marrow Microenvironment Model of B-Lineage Acute Lymphoblastic Leukemia.
980 Cancers (Basel). 2022;14(11).
981 63. Wartewig T, Daniels J, Schulz M, Hameister E, Joshi A, Park J, et al. PD-1 instructs a tumor-
982 suppressive metabolic program that restricts glycolysis and restrains AP-1 activity in T cell lymphoma. Nat
983 Cancer. 2023;4(10):1508-25.
984 64. Petovari G, Danko T, Tokes AM, Vetlenyi E, Krencz I, Raffay R, et al. In Situ Metabolic
985 Characterisation of Breast Cancer and Its Potential Impact on Therapy. Cancers (Basel). 2020;12(9).
986 65. Hart ML, Quon E, Vigil ABG, Engstrom IA, Newsom OJ, Davidsen K, et al. Mitochondrial redox
987 adaptations enable alternative aspartate synthesis in SDH-deficient cells. Elife. 2023;12.
988 66. Sola-Garcia A, Caliz-Molina MA, Espadas I, Petr M, Panadero-Moron C, Gonzalez-Moran D, et al.
989 Metabolic reprogramming by Acly inhibition using SB-204990 alters glucoregulation and modulates
990 molecular mechanisms associated with aging. Commun Biol. 2023;6(1):250.
991 67. Granchi C. ATP citrate lyase (ACLY) inhibitors: An anti-cancer strategy at the crossroads of glucose
992 and lipid metabolism. Eur J Med Chem. 2018;157:1276-91.

993 68. Chambers KT, Chen Z, Lai L, Leone TC, Towle HC, Kralli A, et al. PGC-1beta and ChREBP partner to
994 cooperatively regulate hepatic lipogenesis in a glucose concentration-dependent manner. Mol Metab.
995 2013;2(3):194-204.
996 69. Zhang H, Li L, Chen Q, Li M, Feng J, Sun Y, et al. PGC1beta regulates multiple myeloma tumor
997 growth through LDHA-mediated glycolytic metabolism. Mol Oncol. 2018;12(9):1579-95.
998 70. Korobkina ED, Calejman CM, Haley JA, Kelly ME, Li H, Gaughan M, et al. Brown fat ATP-citrate
999 lyase links carbohydrate availability to thermogenesis and guards against metabolic stress. Nat Metab.
1000 2024;6(11):2187-202.
1001 71. Huhn JM, Valin L, Basse M, Sokei J, Gabriel N, Martinez E, et al. ATF4 coordinates amino acid and
1002 nucleotide synthesis with selective protein translation to ensure proper DNA replication timing in
1003 leukemia cells. Nat Commun. 2026;17(1).
1004 72. Watanabe A, Tipgomut C, Totani H, Yoshimura K, Iwano T, Bashiri H, et al. Noncanonical TCA cycle
1005 fosters canonical TCA cycle and mitochondrial integrity in acute myeloid leukemia. Cancer Sci.
1006 2025;116(1):152-63.
1007 73. Li Z, Deng W, Yang L, Tang C, Yue JM, Monteiro O, et al. Lipid metabolism in homeostasis and
1008 disease. Signal Transduct Target Ther. 2026;11(1):55.
1009 74. Wang Q, Yang HS. The role of Pdcd4 in tumour suppression and protein translation. Biol Cell. 2018.
1010 75. Matsuhashi S, Manirujjaman M, Hamajima H, Ozaki I. Control Mechanisms of the Tumor
1011 Suppressor PDCD4: Expression and Functions. Int J Mol Sci. 2019;20(9).
1012 76. Hilliard A, Hilliard B, Zheng SJ, Sun H, Miwa T, Song W, et al. Translational regulation of
1013 autoimmune inflammation and lymphoma genesis by programmed cell death 4. J Immunol.
1014 2006;177(11):8095-102.

1015

1016 **Figure legends:**

1017 **Figure 1. Structure-based identification and biochemical validation of novel ACLY inhibitors.**

1018 (A) Schematic overview of the structure-based drug discovery workflow used to identify novel small-
1019 molecule inhibitors targeting the ATP-binding site of human ACLY. (B) Generation of a structure-based
1020 pharmacophore model using the adenine nucleoside-binding interactions of ADP in the human ACLY
1021 crystal structure (PDB: 3PFF). (C) Five-point 3D pharmacophore model comprising one hydrogen-bond
1022 donor (Don), three hydrogen-bond acceptors (Acc), and one aromatic ring center (Ar), with spatial distance
1023 constraints derived from the ACLY–ADP structure. (D) Identification of the putative ATP-binding pocket
1024 using the MOE Site Finder module; dummy atoms within the pocket are shown as spheres, with protein-
1025 contacting and non-contacting sites indicated separately. (E) Docking pose of VCB1 within the ATP-
1026 binding pocket of human ACLY, showing the compound and surrounding pocket residues. (F) Predicted
1027 molecular interactions between VCB1 and ACLY, showing five favorable hydrogen bonds involving

1028 residues R66, E108, E201, and D216, including two interactions formed by R66 with nitrogen atoms of
1029 VCB1. (G) Chemical structures of the three active compounds identified from the NCI chemical database
1030 together with the reference ACLY inhibitor BMS-303141. (H) Biochemical validation of ACLY inhibition
1031 using recombinant human ACLY. BMS-303141 inhibited ACLY with an IC_{50} of approximately 250 nM,
1032 whereas VCB1 inhibited ACLY with an IC_{50} of approximately 560 nM, confirming direct enzymatic
1033 inhibition. Overall, the workflow identified VCB1 as a novel ATP-site-directed ACLY inhibitor for
1034 Furthermore cellular and mechanistic characterization.

1035 **Figure 2. Novel ACLY inhibitor decreases ACLY activity and promotes cell death**.

1036 (A) SUPM2 parental-ALKi sensitive and SUPM2-LR1000 ALKi-resistant ALK-positive ALCL cells
1037 were treated with ACLY inhibitors VCB1, VCB2, VCB7, or BMS-303141 (BMS) at 1.0 μM for 48 h in
1038 5% FBS medium. Cell lysates were analyzed by immunoblotting for cleaved PARP1 and cleaved caspase-
1039 3 as markers of apoptosis. (B) Ibrutinib-sensitive Jeko-1 and ibrutinib-resistant Maver MCL cells were
1040 treated with the indicated ACLY inhibitors under the same conditions, and apoptosis was assessed by
1041 immunoblotting for cleaved PARP1 and cleaved caspase-3. (C–F) TKI-resistant lymphoma cells were
1042 treated with VCB1 or BMS at 1.0 μM for 24 h, followed by analysis of ACLY, ACACA, FASN, and ACSS2
1043 expression. (G) Schematic representation of the proposed NPM-ALK–ACLY metabolic axis, in which
1044 NPM-ALK-mediated phosphorylation of ACLY at Y682 promotes ACLY activity and supports de novo
1045 fatty-acid synthesis. (H–M) Cellular ACLY activity was measured following treatment with VCB1 or BMS
1046 in S-sensitive and SLR-resistant ALK-positive ALCL cells and in MCL cell lines. Data are representative
1047 of independent experiments. Statistical significance was determined using the appropriate statistical test; P
1048 < 0.05 was considered significant.

1049 Figure 3. **RNA-sequencing reveals metabolic, proliferative, and inflammatory reprogramming**
1050 **following ACLY inhibition.**

1051 (A) Number of differentially expressed genes (DEGs) identified in TKI-sensitive (S-VCB1) and TKI-
1052 resistant (SLR-VCB1) cells following VCB1 treatment compared with DMSO controls. DEGs were defined
1053 using log2 FC ≥ 0.5 and $P < 0.05$. Venn diagram shows DEGs unique to each cellular context and genes
1054 commonly regulated by VCB1. (B) KEGG pathway enrichment analysis of DEGs identified following
1055 ACLY inhibition using NIH-DAVID, showing enrichment of ribosome biogenesis, amino-acid
1056 biosynthesis, HIF-1 and TNF signaling, carbon metabolism, and other metabolic pathways. (C) Distribution
1057 of metabolism-associated DEGs across major metabolic categories, highlighting carbon metabolism as a
1058 prominent transcriptionally affected pathway. (D,E) Volcano plots showing the transcriptional response to
1059 VCB1 in S-sensitive and SLR-resistant cells (F) Heatmap of representative DEGs in S-sensitive cells
1060 following VCB1 treatment. (G) Heatmap of lipid-metabolism-associated DEGs in SLR-resistant cells
1061 following VCB1 treatment. (H) Basal glycerophospholipid metabolism-associated gene expression in S-
1062 sensitive versus SLR-resistant cells, demonstrating distinct lipid synthesis and remodeling programs
1063 associated with S sensitivity and resistance. (I) Basal cholesterol- and lipid-metabolism-associated gene
1064 expression in parental SUP-M2 and SLR-resistant SLR-D cells. (J) SREBP-associated DEGs following
1065 VCB1 treatment in S-sensitive cells. (K) In schematic display showing ACLY networking genes by suing
1066 strin-protein interactome website. (L) Cell-cycle-associated DEGs following ACLY inhibition, showing
1067 induction of checkpoint and stress-response genes and suppression of mitotic regulators. (M) DEGs
1068 associated with TNF and IL-17 signaling pathways following ACLY inhibition in S-sensitive and SLR-
1069 resistant cells.

1070 Figure 4. **Cancer hallmark enrichment of common and cell-line-specific DEGs following ACLY**
1071 **inhibition**.

1072 (A) Cancer hallmark enrichment analysis of DEGs unique to SUPM2-LR1000 (SLR) cells following VCB1
1073 treatment using a log2 fold-change cutoff of ≥ 0.3 up and down regulated. The cancer hallmark pathways
1074 are shown on the table below. (B) Hallmark enrichment analysis of downregulated DEGs in SLR-VCB1
1075 cells using log2 fold-change of -0.7 down regulated. The significant DEGs related to each hallmark are

1076 shown below. (C) Hallmark analysis of upregulated DEGs in SLR-VCB1 cells demonstrating significant
1077 enrichment of sustained angiogenesis. The corresponding enriched genes are shown in the right panel. (D)
1078 Hallmark enrichment analysis of commonly upregulated DEGs shared between S-VCB1 and SLR-VCB1
1079 cells using a log2 fold-change cutoff of ≥0.7. Sustained angiogenesis, resisting cell death, and
1080 reprogramming energy metabolism were significantly enriched, with the corresponding genes shown in the
1081 right panel.

1082 Figure 5. **Untargeted metabolomics reveals distinct metabolic consequences of ACLY inhibition by**
1083 **VCB1.**

1084 (A) Hierarchical clustering heatmap of significantly altered metabolites identified by untargeted
1085 metabolomics in TKI-sensitive cells (SUPM2) treated with DMSO, VCB1, or BMS-303141. Metabolites
1086 were considered significant at $q<0.05$ and a minimum 1.5-fold change. (B) Heatmap showing the most
1087 strongly altered metabolites using a 4-fold change cutoff, highlighting marked depletion of purine and
1088 pyrimidine-related metabolites and accumulation of glycolytic and central-carbon intermediates following
1089 VCB1 treatment. (C) Citrate abundance based on metabolomics peak abundance quantification in TKI-
1090 sensitive, SUPM2 cells treated with DMSO, VCB1, or BMS-303141, the schematic of Citrate to acetyl-
1091 CoA conversion via ACLY shown in bottom panel. (D) Volcano plot shows significantly altered
1092 metabolites following VCB1 treatment. (E) Volcano plot showing metabolic changes following BMS-
1093 303141 treatment, demonstrating substantially fewer alterations and no significant accumulation of citrate.
1094 (F) Metabolic pathway enrichment analysis of significantly altered metabolites following VCB1 treatment
1095 using MetaboAnalyst. (G) Pathway impact analysis showing the major metabolic pathways affected by
1096 VCB1, including pyrimidine, purine, pyruvate, and citrate metabolism. (H) Comparison of basal metabolite
1097 abundance between TKI-sensitive and TKI-resistant cell lines, demonstrating increased abundance of
1098 multiple nucleotide metabolites in SLR cells. (I) Hierarchical clustering of significantly altered metabolites
1099 in SLR cells following VCB1 treatment, showing metabolic perturbations that overlap with those observed
1100 in SUPM2 cells but with lower magnitude. Statistical significance was defined as $q<0.05$.

1101 Figure 6. **ACLY inhibition revealed distinct lipid remodeling in TKI-sensitive and TKI-resistant**
1102 **lymphoma cell lines.**

1103 (A) PCA of untargeted lipidomic profiles from SUPM2 parental cells treated with DMSO, VCB1, or BMS-
1104 303141 (BMS), showing treatment-dependent separation of lipidomic profiles. (B) PCA of lipidomic
1105 profiles from SLR cells treated with DMSO, VCB1, or BMS. (C,D) Hierarchical clustering heat maps of
1106 significantly altered lipid species ($q \leq 0.05$) in SUPM2 parental (C) and SLR (D) cells. (E) Heatmap of lipid
1107 species showing the most pronounced changes in SUPM2 parental cells following VCB1 treatment using a
1108 stringent >15-fold-change threshold. VCB1 treatment predominantly increased ceramide, hexosylceramide,
1109 sphingomyelin, and selected phospholipid species, whereas PG(12:0_14:0), PG(10:0_14:0), and SM(d39:6)
1110 were markedly decreased. (F) Heatmap of the most strongly altered lipid species in SLR cells using the
1111 same >15-fold-change threshold, demonstrating prominent increases in ceramide and related sphingolipid
1112 species following VCB1 treatment. Comparable changes were not observed in BMS or DMSO-treated cells.
1113 Each point in the PCA represents an individual biological replicate.

1114 Figure 7. **VCB1-mediated ACLY inhibition induces extensive lipid species and transcriptional**
1115 **remodeling in lymphoma cells**.

1116 (A) Distribution of lipid classes identified by untargeted lipidomic profiling following ACLY inhibition.
1117 VCB1 induced broad remodeling across acylcarnitines, ceramides, glycosphingolipids, PC, PE, PG, CL,
1118 PS, PI, SM, DG, ChE, and TG classes. (B) Differential abundance of TG molecular species, demonstrating
1119 more pronounced remodeling in SUPM2 cells, with reciprocal changes in species containing saturated,
1120 unsaturated, very-long-chain, ether-linked, and PUFA-containing fatty acids. (C) Remodeling of PC
1121 species, characterized by enrichment of selected ether-linked and PUFA-containing PCs and depletion of
1122 multiple conventional diacyl PCs. (D) Remodeling of PE species, with preferential enrichment of
1123 ether/plasmalogen and PUFA-containing species and depletion of selected shorter-chain
1124 saturated/monounsaturated species. (E) Differential abundance of DG species following VCB1 treatment
1125 in SUPM2 and SLR cells. VCB1 produced broad, species-specific DG remodeling, whereas BMS induced

1126 comparatively weak changes. (F) Differential abundance of ChE species following VCB1 or BMS
1127 treatment, demonstrating broad remodeling of cholesterol ester species following VCB1 treatment. (G)
1128 Changes in acylcarnitine species, showing accumulation of several long-chain saturated species and
1129 depletion of shorter-chain and unsaturated species, consistent with altered mitochondrial fatty-acid
1130 handling.

1131 Figure 8. **VCB1 induces metabolic remodeling, integrated stress response, redox stress, apoptosis, and**
1132 **immune regulation**.

1133 (A) Heatmap based on the NIH-DAVID and KEGG pathway analysis of lipid-metabolism-associated DEGs
1134 following VCB1 treatment, demonstrating significant remodeling of lipid metabolic pathways that were not
1135 observed with BMS-303141 at the same concentration. (B) Heatmap of representative ISR/stress-associated
1136 DEGs induced by VCB1 (C-E) RT-PCR validation of representative ISR, inflammatory, and redox-
1137 associated genes, including PPP1R15A/GADD34, NLRP3, and CHAC1, respectively. (F-H) Effects of
1138 VCB1 and BMS-303141 on glutathione metabolism, including GSH/GSSG ratio, γ-glutamylcysteine, and
1139 S-lactoylglutathione levels. (I) Representative apoptosis- and stress-associated DEGs induced by VCB1.
1140 (J) Differential expressions of inflammatory and immune-regulatory genes, including NLRC5, NLRP1,
1141 NLRP3, CD226, PDCD1, and PDCD4. (K) Integrated gene-metabolite interaction network generated from
1142 VCB1-responsive transcriptomic and metabolomic datasets demonstrating enrichment of lipid-metabolic
1143 interactions in sensitive cells. (L) Schematic model summarizing the downstream consequences of VCB1-
1144 mediated ACLY inhibition, including metabolic remodeling, suppression of ACLY-dependent lipogenesis,
1145 ISR activation, CHAC1-associated glutathione depletion, redox and apoptotic stress, and
1146 inflammatory/immune-regulatory signaling. Unless otherwise indicated, differential expression was
1147 defined using a log2 FC threshold of ≥ 0.5 or ≤ -0.5.

1148 Figure 9. **VCB1 inhibits lymphoma cell proliferation through coordinated metabolic stress induced**
1149 **response and cell-cycle alteration.**

1150 (A,B) Dose–response analysis of VCB1, VCB2, VCB7, and BMS in TKI-sensitive, SUPM2 and TKI-
1151 resistant, SLR lymphoma cells following 72 h treatment in 5% FBS. (C,D) Antiproliferative activity of the
1152 indicated ACLY inhibitors in BTK inhibitor-sensitive Jeko-1 and BTK inhibitor-resistant Maver mantle
1153 cell lymphoma cells. (E) RNA-seq analysis of differentially expressed genes associated with cell-cycle
1154 progression and cell growth following VCB1 treatment. (F–H) Cell-cycle analysis of SUPM2 parental,
1155 SLR, and Jeko-1 cells treated with 0.5 μM VCB1 or BMS for 48 h, demonstrating increased G0/G1-phase
1156 accumulation following VCB1 treatment. (I, J) RNA-seq and RT-qPCR validation of DHODH and CAD
1157 expression following VCB1 treatment. (K) Differential expression of pyrimidine biosynthesis-related genes
1158 following VCB1 treatment compared with BMS-303141. (L–O) Expression of LPCAT1 and cholesterol
1159 biosynthesis-associated genes, including HMGCR, INSIG1, and INSIG2, following VCB1 treatment. (P)
1160 Integrated analysis of RNA-seq and metabolomics demonstrating coordinated disruption of pyrimidine
1161 biosynthesis by VCB1. Data are presented as mean ± SEM; statistical significance was determined using
1162 the graph prism software and performed t-test analysis. A p-value of < 0.05 was considered statistically
1163 significant (*, $p < 0.05$; **, $p < 0.01$; ***, $p < 0.001$; ****, $p < 0.0001$).

1164

1165 **Supplementary Figure legends:**

1166 **Supplementary Fig. 1**. Chemical structures of ACLY inhibitor candidates selected for activity screening.
1167 Two-dimensional chemical structures of the additional compounds selected from the NCI repository for
1168 ACLY activity screening.

1169 **Supplementary Fig.2.** Genetic silencing of ACLY in ALK+ALCL cell line and xenograft model revealed
1170 ACLY as a therapeutic target

1171 (A) Images of tumor bearing mice derived from shControl SUDHL-1 cells $2X10^6$ cells xenografted into SCID-
1172 beige mice. (B) Tumor volumes of xenografts derived from representative images in figure A. (C)

1173 Representative tumor weights at the endpoint of the experiment. (D) Images of non-tumor bearing mice
1174 derived from shACLY SUDHL-1 cells $2X10^6$ cells xenografted into SCID-beige mice.

1175 **Supplementary Fig. 3** RNA sequencing identifies distinct transcriptional responses to VCB1 and BMS-
1176 303141 in ALK+ ALCL cells.

1177 (A) Summary of the total number and direction of differentially expressed genes identified across the
1178 indicated comparisons. (B) Comparison of the number of DEGs identified following VCB1 and BMS-
1179 303141 treatment in ALKi-sensitive SUPM2 parental cells. (C) Representative global transcriptional
1180 comparison of VCB1- and BMS-treated parental cells. (D) Differential gene expression analysis of S-VCB1
1181 versus S-DMSO cells, identifying 793 upregulated and 209 downregulated genes using a threshold of log2
1182 FC ≥1 and P<0.05. (E) Differential gene expression analysis of S-BMS versus S-DMSO cells, identifying
1183 42 upregulated and 65 downregulated genes using the same criteria. (F) Differential gene expression
1184 analysis comparing untreated ALKi-resistant SUPM2-LR1000 (SLR) cells with parental SUPM2 cells,
1185 identifying 3,318 upregulated and 2,979 downregulated genes. Three biological replicates were analyzed
1186 per treatment group.

1187 **Supplementary Fig. 4**. STRING-network analysis of common differentially expressed genes (DEGs)
1188 following VCB1 treatment. STRING-network analysis of DEGs commonly altered in TKI-sensitive and
1189 TKI-resistant cells using a $\log_2$ fold-change (FC) threshold of ≥1.0 and P<0.05. The network illustrates
1190 functional interactions among common DEGs irrespective of biological function.

1191 **Supplementary Fig. 5.** Functional network and pathway enrichment analysis of common VCB1-
1192 responsive DEGs. (A) STRING-network analysis of common DEGs associated with metabolic pathways
1193 using a log2 FC threshold of ≥1.0 and P<0.05. (B) Biological process enrichment of common DEGs
1194 associated with cellular lipid responses. (C, D) Network analysis showing TNF and HIF-1 signaling-
1195 associated transcriptional changes among common VCB1-responsive DEGs.

1196 **Supplementary Fig. 6**. Hallmark cancer pathway enrichment among common VCB1-responsive DEGs.
1197 (A, B) Enrichment of reprogrammed energy metabolism and sustained angiogenesis among common DEGs
1198 identified using a log2 FC cutoff of ≥0.5. (C, D) Common upregulated DEGs were enriched for sustained
1199 angiogenesis, sustained proliferative signaling, resistance to cell death, and reprogrammed energy
1200 metabolism. (E, F) Common downregulated DEGs were predominantly enriched for reprogrammed energy
1201 metabolism.

1202 **Supplementary Fig.7** Gene-metabolite interaction network

1203 (A) Integrated gene-metabolite interaction network generated from VCB1-responsive transcriptomic and
1204 metabolomic datasets demonstrating enrichment of lipid-metabolic interactions in SLR cell line. (B) ACLY
1205 gene-metabolite specific network node highlighted from the above.

1206 **Table 1.** Common metabolic function related differentially expressed genes (DEGs) in TKI-sensitive,
1207 SUPM2 and TKI-resistant, SLR cells following VCB1 treatment. Metabolic function-associated
1208 differentially expressed genes (DEGs) were identified from RNA-seq data using a log2 fold-change (FC)
1209 threshold of ≥ +0.5 or ≤ −0.5 in both cells following VCB1 treatment.

1210 **Supplementary Table 1**. Metabolic differentially expressed genes (DEGs) specific to SUPM2 parental
1211 cells following VCB1 treatment. SUPM2 parental-specific metabolic DEGs were identified using a log2
1212 fold-change (FC) threshold of ≥ +0.5 or ≤ −0.5.

1213 **Supplementary Table 2.** Metabolic differentially expressed genes (DEGs) specific to SLR cells following
1214 VCB1 treatment. SLR cell-specific metabolic DEGs were identified using a log2 fold-change (FC)
1215 threshold of ≥ +0.5 or ≤ −0.5.

Fig.1

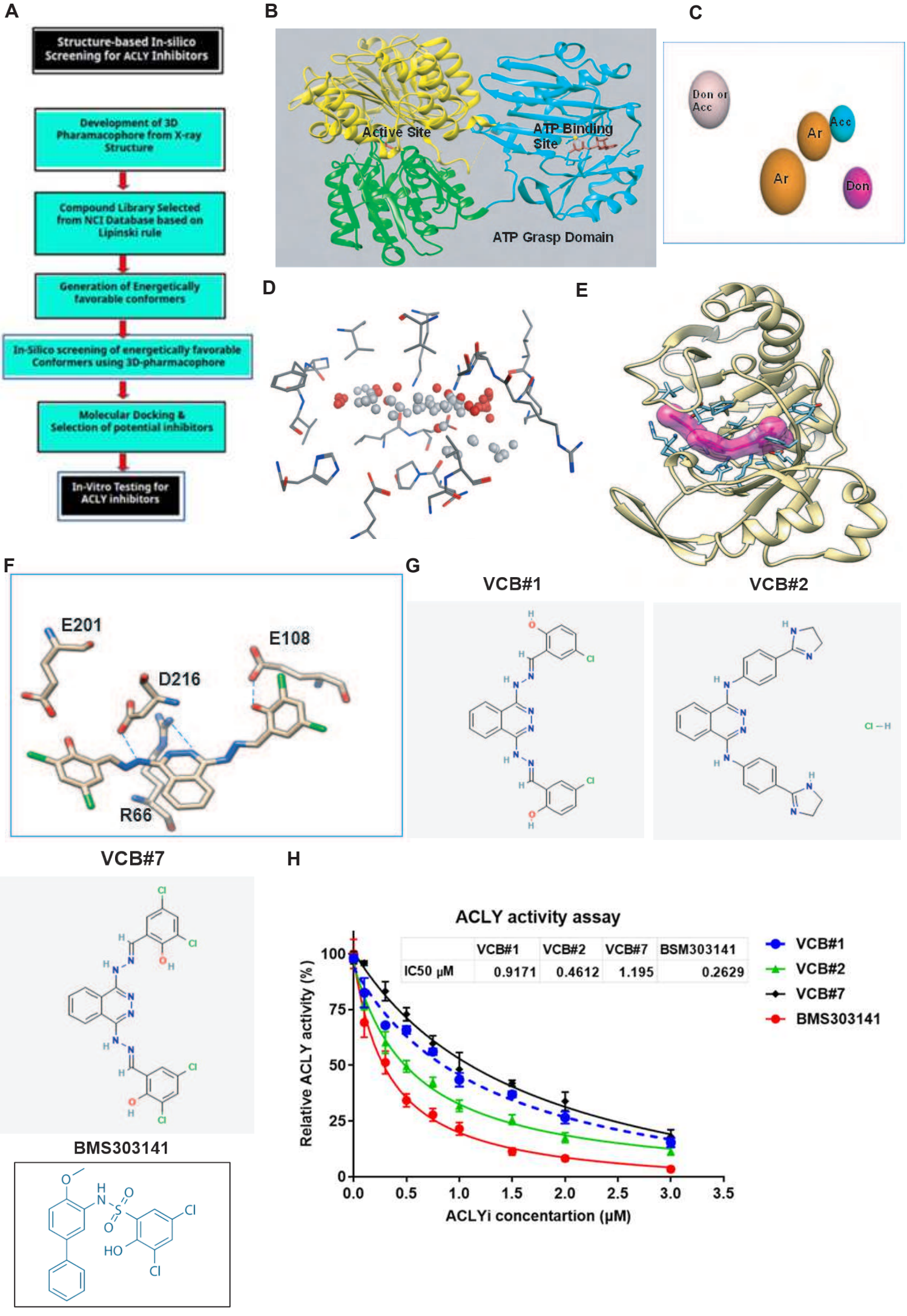
A
Structure-based In-silico Screening for ACLY Inhibitors
Development of 3D Pharamacophore from X-ray Structure
Compound Library Selected from NCI Database based on Lipinski rule
Generation of Energetically favorable conformers
In-Silico screening of energetically favorable Conformers using 3D-pharmacophore
Molecular Docking & Selection of potential inhibitors
In-Vitro Testing for ACLY inhibitors
B
Active Site
ATP Binding Site
ATP Grasp Domain
C
Don or Acc
Ar
Acc
Ar
Don
D
E
F
E201
E108
D216
R66
G
VCB#1
VCB#2
VCB#7
BMS303141
H
ACLY activity assay
VCB#1 VCB#2 VCB#7 BSM303141
IC50 μM 0.9171 0.4612 1.195 0.2629
Relative ACLY activity (%)
ACLYi concentartion (μM)
VCB#1
VCB#2
VCB#7
BMS303141

Fig.2

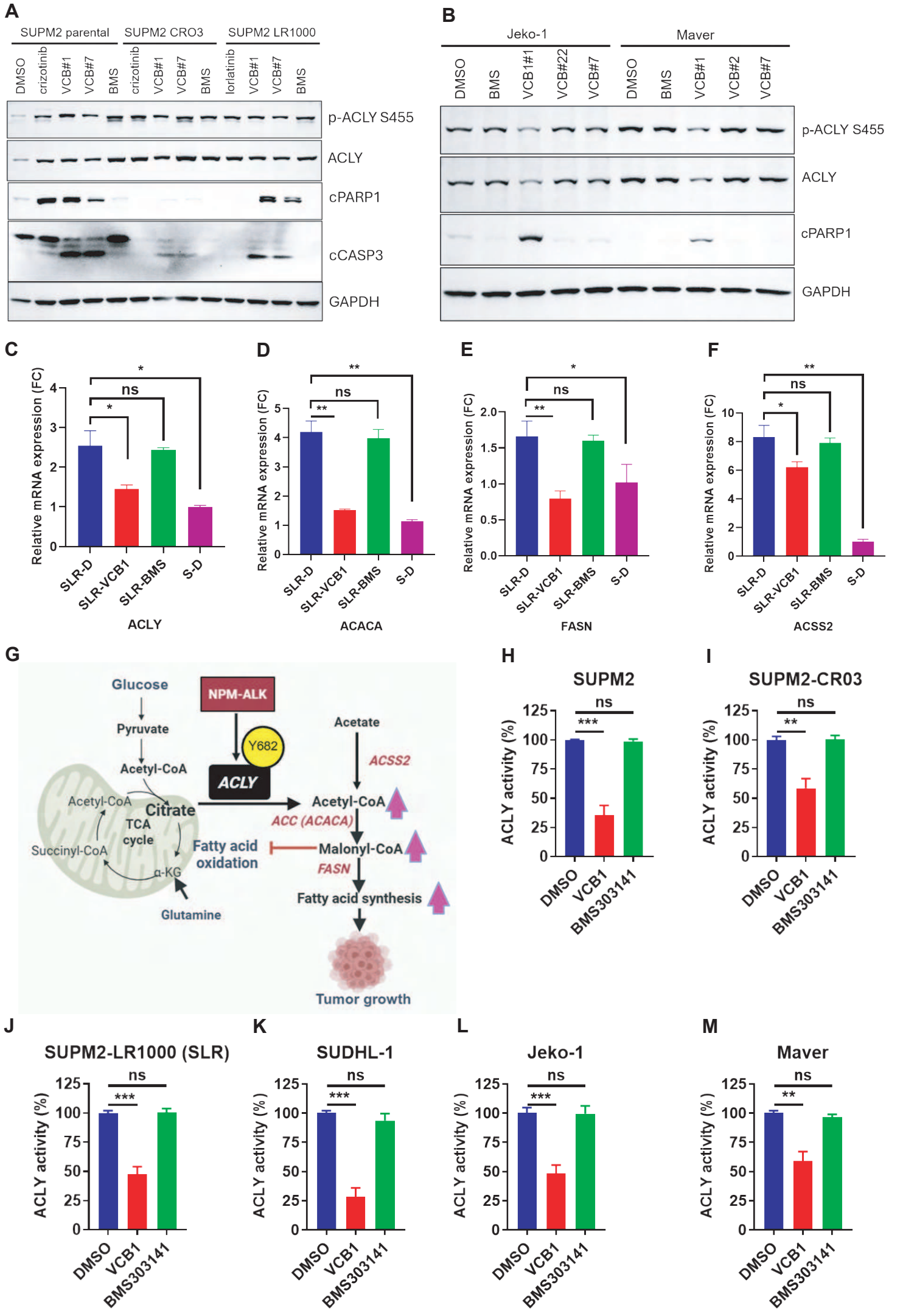
A
SUPM2 parental
SUPM2 CRO3
SUPM2 LR1000
DMSO
crizotinib
VCB#1
VCB#7
BMS
crizotinib
VCB#1
VCB#7
BMS
lorlatinib
VCB#1
VCB#7
BMS
p-ACLY S455
ACLY
cPARP1
cCASP3
GAPDH
B
Jeko-1
Maver
DMSO
BMS
VCB1#1
VCB#22
VCB#7
DMSO
BMS
VCB#1
VCB#2
VCB#7
p-ACLY S455
ACLY
cPARP1
GAPDH
C
Relative mRNA expression (FC)
SLR-D
SLR-VCB1
SLR-BMS
S-D
ACLY
D
Relative mRNA expression (FC)
ACACA
E
Relative mRNA expression (FC)
FASN
F
Relative mRNA expression (FC)
ACSS2
G
Glucose
Pyruvate
Acetyl-CoA
NPM-ALK
Y682
ACLY
Acetate
ACSS2
Acetyl-CoA
Citrate
TCA cycle
Succinyl-CoA
α-KG
Glutamine
Fatty acid oxidation
Acetyl-CoA
ACC (ACACA)
Malonyl-CoA
FASN
Fatty acid synthesis
Tumor growth
H
SUPM2
ACLY activity (%)
DMSO
VCB1
BMS303141
I
SUPM2-CR03
ACLY activity (%)
DMSO
VCB1
BMS303141
J
SUPM2-LR1000 (SLR)
ACLY activity (%)
DMSO
VCB1
BMS303141
K
SUDHL-1
ACLY activity (%)
DMSO
VCB1
BMS303141
L
Jeko-1
ACLY activity (%)
DMSO
VCB1
BMS303141
M
Maver
ACLY activity (%)
DMSO
VCB1
BMS303141

Fig.3

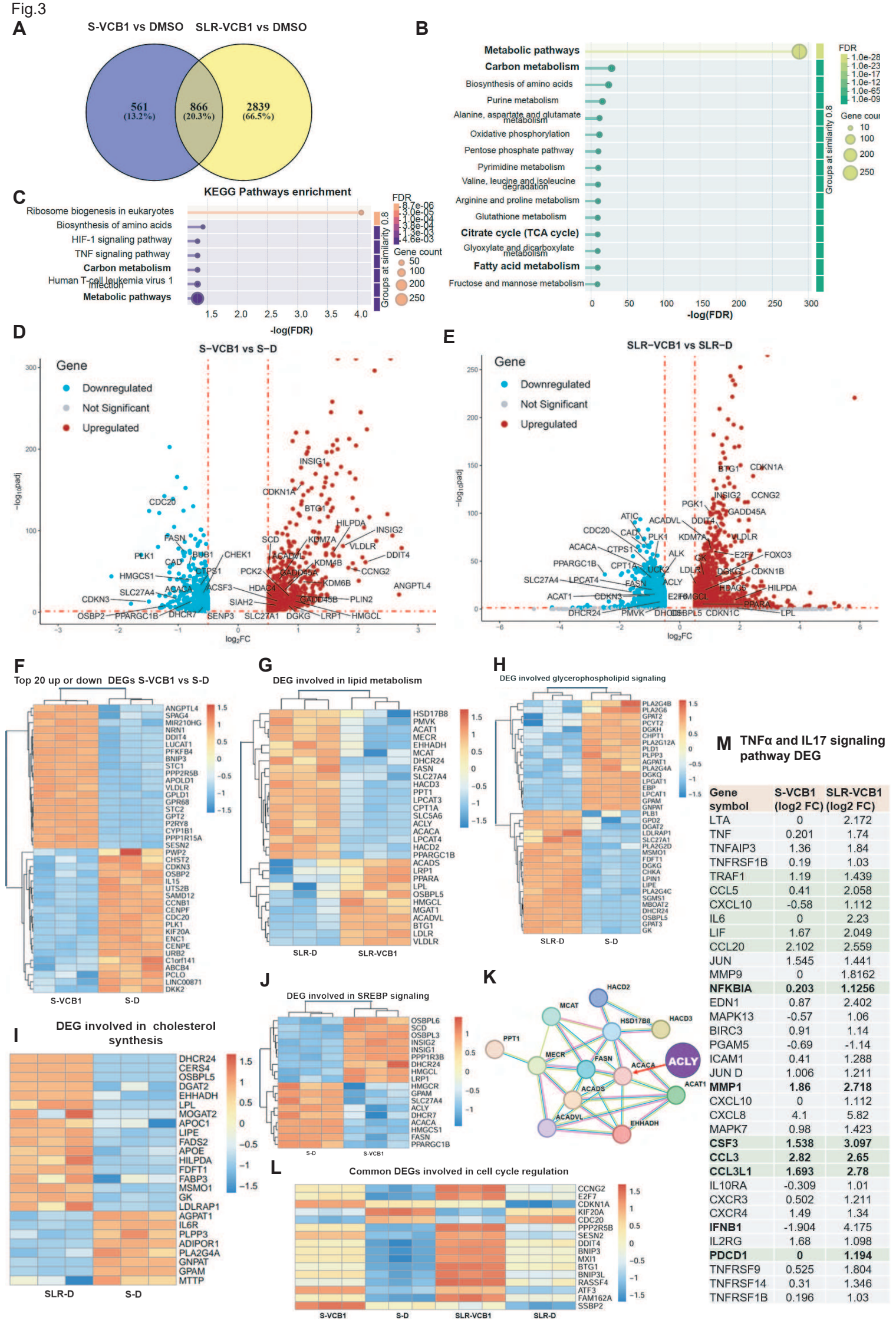

M TNFα and IL17 signaling pathway DEG

Gene symbol	S-VCB1 (log2 FC)	SLR-VCB1 (log2 FC)
LTA	0	2.172
TNF	0.201	1.74
TNFAIP3	1.36	1.84
TNFRSF1B	0.19	1.03
TRAF1	1.19	1.439
CCL5	0.41	2.058
CXCL10	-0.58	1.112
IL6	0	2.23
LIF	1.67	2.049
CCL20	2.102	2.559
JUN	1.545	1.441
MMP9	0	1.8162
NFKBIA	**0.203**	**1.1256**
EDN1	0.87	2.402
MAPK13	-0.57	1.06
BIRC3	0.91	1.14
PGAM5	-0.69	-1.14
ICAM1	0.41	1.288
JUN D	1.006	1.211
MMP1	**1.86**	**2.718**
CXCL10	0	1.112
CXCL8	4.1	5.82
MAPK7	0.98	1.423
CSF3	**1.538**	**3.097**
CCL3	**2.82**	**2.65**
CCL3L1	**1.693**	**2.78**
IL10RA	-0.309	1.01
CXCR3	0.502	1.211
CXCR4	1.49	1.34
IFNB1	**-1.904**	**4.175**
IL2RG	1.68	1.098
PDCD1	**0**	**1.194**
TNFRSF9	0.525	1.804
TNFRSF14	0.31	1.346
TNFRSF1B	0.196	1.03

Fig.4

A

SLR-VCB1 DEGs both up and down (log2 -/+ 0.3 FC)

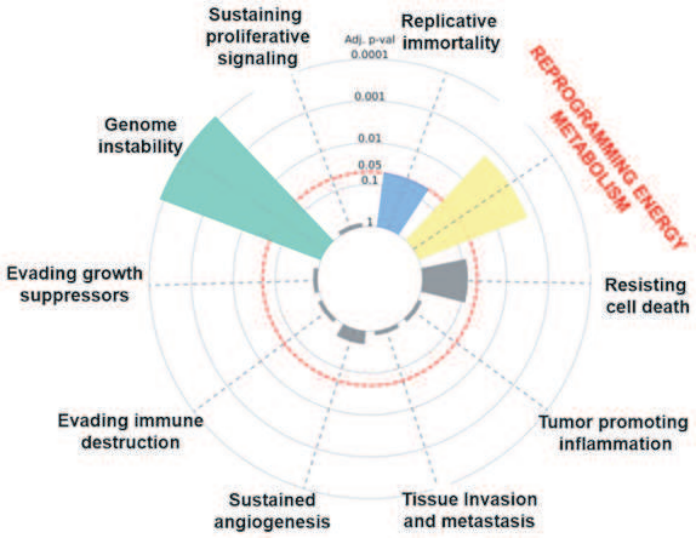

Cancer Hallmark	Overlap	P-value	Adjusted P-value
GENOME INSTABILITY	**112/178**	**0.00001**	**0.0001**
REPROGRAMMING ENERGY METABOLISM	**94/155**	**0.00034**	**0.00171**
REPLICATIVE IMMORTALITY	**55/94**	**0.01461**	**0.0487**
RESISTING CELL DEATH	217/423	0.03316	0.0829
SUSTAINED ANGIOGENESIS	59/117	0.24194	0.48388
TUMOR-PROMOTING INFLAMMATION	30/66	0.63242	0.99998
EVADING IMMUNE DESTRUCTION	47/106	0.72667	0.99998
EVADING GROWTH SUPPRESSORS	180/407	0.86439	0.99998
SUSTAINING PROLIFERATIVE SIGNALING	270/655	0.9985	0.99998
TISSUE INVASION AND METASTASIS	242/624	0.99998	0.99998

B

SLR-VCB1 DEGs down (log2 > - 0.7 FC)

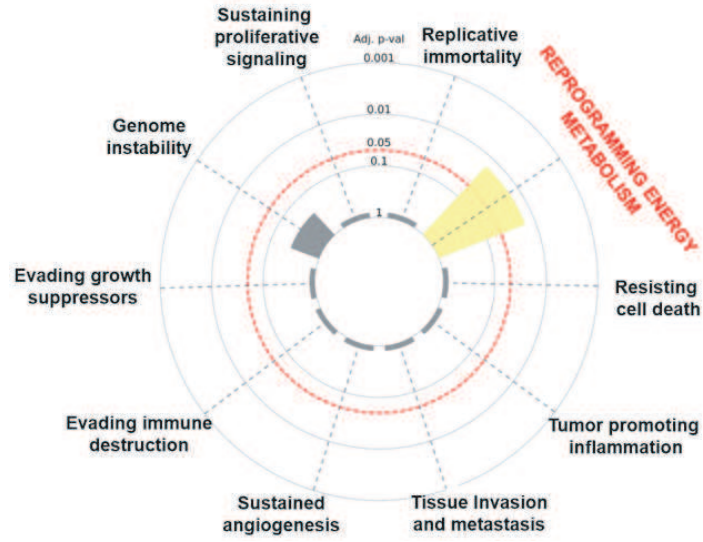

REPROGRAMMING ENERGY METABOLISM

FASN, PRPS2, PRKAG1, PHKA1, UQCRFS1, SUCLG2, IDH1, CS, PRPS1, IDH3A, PFKM, **ACLY**, NDUFS7, DLAT, SDHB, RPIA, NDUFS8, **ACACA**, MTOR, PPARG, BPGM, FH, NDUFS1, HIF1A, OGDH, LDHB, **MDH2**

GENOME INSTABILITY

PCNA, MCM5, CDC25A, PRKDC, FANCF, RAD50, UNG, TDG, ATR, CHEK1, LIG3, CLSPN, PMS1, TERT, NPM1, RAD1, ERCC2, POLE2, FANCE, NTHL1, PTTG1, EXO1, RAD51, PARP1

C

SLR-VCB1 DEGs up (log2 > + 0.7 FC)

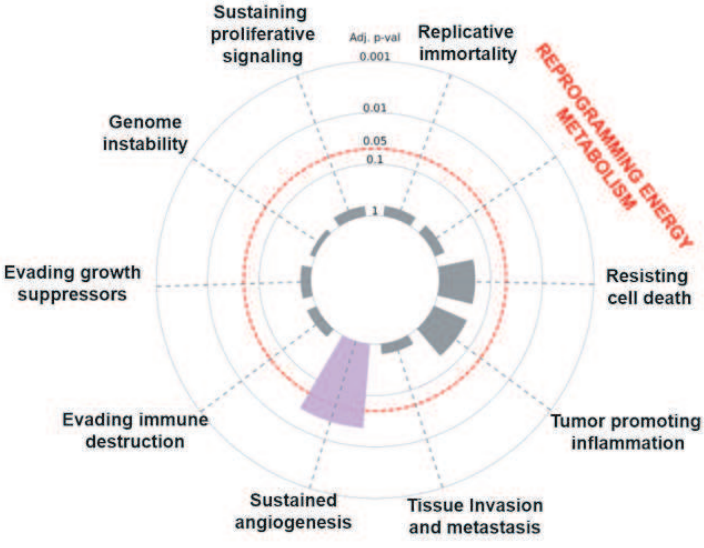

REPROGRAMMING ENERGY METABOLISM

EDN1, **PFKFB3,** ALDOA, BNIP3, **PDK1**, MAP2K1**, ENO2**, GYS1, RPTOR, CDKN1B, PGK1, PFKP, ALDOC, ERBB2, SLC16A3, PFKL, GAPDH

RESISTING CELL DEATH

KDR, ARF4, BNIP3, NOL3, ITGB4, CCND2, MAPK13, SGK1, TNFRSF21, EPO, TRADD, GRK5, JUN, TGFBR2, MAPK7, HBEGF, TNF, THBS1, BCL2L2, TNFRSF1B, CDKN1B, TNFRSF10D, EPAS1, ITGB3, BNIP3L, FOXO4, BIRC3, CDKN1A, TNFRSF9, TGFA, MAP3K8, NFKBIA, SPHK1, TGFBR1, APAF1, MAP2K1, IL2RG, LTA, MMP9, DDIT3, VEGFA, FOXO3, BCL2A1, IL2RB, BIRC2, BCL10, TRAF1, NFKB1, PIM1, BBC3, IL6ST, SOD2, IL6, FOS, RELA, ERBB2, BCL6, FAS

EVADING IMMUNE DESTRUCTION

PDCD1, FES, MAP2K1, **BCL6**, **CD247,** IL6, HLA-A, IL2RG, CXCL10, TIAM1, LYN, CXCR4

D

SLR-VCB1 and S-VCB1 DEGs common (log2 +0.7 FC)

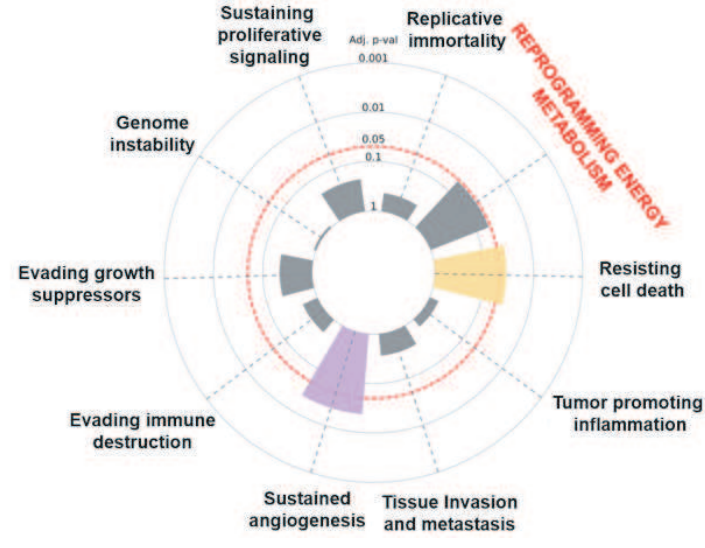

Cancer Hallmark	Overlap	P-value	Adjusted P-value
SUSTAINED ANGIOGENESIS	**10/117**	**0.00236**	**0.02359**
RESISTING CELL DEATH	**22/423**	**0.00715**	**0.03573**
REPROGRAMMING ENERGY METABOLISM	**10/155**	**0.01633**	**0.05444**
EVADING GROWTH SUPPRESSORS	17/407	0.09325	0.22031
SUSTAINING PROLIFERATIVE SIGNALING	25/655	0.11016	0.22031

REPROGRAMMING ENERGY METABOLISM

PFKFB3, PDK1, BNIP3, MAP2K1, ENO2, RPTOR, GYS1, PGK1, SLC16A3, PFKL

SUSTAINED ANGIOGENESIS

KDR, PLAUR, MAP2K1, CXCL8, RRAS, IL1A, EPAS1, ITGB3, VEGFA, CXCR4

RESISTING CELL DEATH

KDR, BNIP3, ITGB4, EPO, GRK5, JUN, MAPK7, EPAS1, ITGB3, BNIP3L, BIRC3, CDKN1A, TNFRSF9, MAP3K8, APAF1, MAP2K1, DDIT3, VEGFA, FOXO3, BCL2A1, TRAF1, BBC3

Fig.5

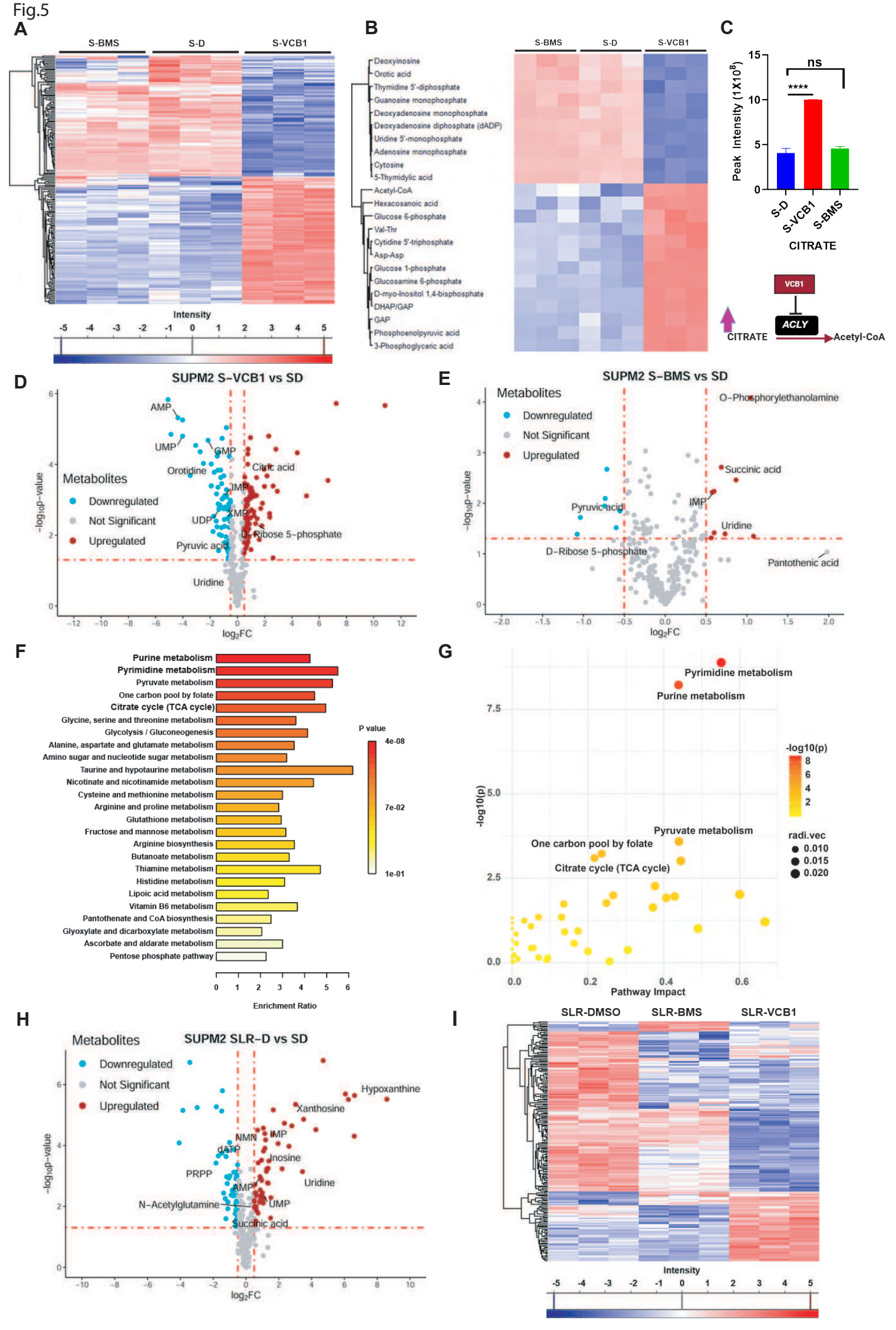
A
S-BMS
S-D
S-VCB1
Intensity
-5 -4 -3 -2 -1 0 1 2 3 4 5
B
S-BMS
S-D
S-VCB1
Deoxyinosine
Orotic acid
Thymidine 5'-diphosphate
Guanosine monophosphate
Deoxyadenosine monophosphate
Deoxyadenosine diphosphate (dADP)
Uridine 5'-monophosphate
Adenosine monophosphate
Cytosine
5-Thymidylic acid
Acetyl-CoA
Hexacosanoic acid
Glucose 6-phosphate
Val-Thr
Cytidine 5'-triphosphate
Asp-Asp
Glucose 1-phosphate
Glucosamine 6-phosphate
D-myo-Inositol 1,4-bisphosphate
DHAP/GAP
GAP
Phosphoenolpyruvic acid
3-Phosphoglyceric acid
C
Peak Intensity (1X10^8)
ns
****
S-D
S-VCB1
S-BMS
CITRATE
VCB1
ACLY
CITRATE
Acetyl-CoA
D
SUPM2 S-VCB1 vs SD
Metabolites
Downregulated
Not Significant
Upregulated
AMP
UMP
GMP
Orotidine
Citric acid
IMP
XMP
UDP
D-Ribose 5-phosphate
Pyruvic acid
Uridine
-log10p-value
log2FC
E
SUPM2 S-BMS vs SD
Metabolites
Downregulated
Not Significant
Upregulated
O-Phosphorylethanolamine
Succinic acid
IMP
Pyruvic acid
Uridine
D-Ribose 5-phosphate
Pantothenic acid
-log10p-value
log2FC
F
Purine metabolism
Pyrimidine metabolism
Pyruvate metabolism
One carbon pool by folate
Citrate cycle (TCA cycle)
Glycine, serine and threonine metabolism
Glycolysis / Gluconeogenesis
Alanine, aspartate and glutamate metabolism
Amino sugar and nucleotide sugar metabolism
Taurine and hypotaurine metabolism
Nicotinate and nicotinamide metabolism
Cysteine and methionine metabolism
Arginine and proline metabolism
Glutathione metabolism
Fructose and mannose metabolism
Arginine biosynthesis
Butanoate metabolism
Thiamine metabolism
Histidine metabolism
Lipoic acid metabolism
Vitamin B6 metabolism
Pantothenate and CoA biosynthesis
Glyoxylate and dicarboxylate metabolism
Ascorbate and aldarate metabolism
Pentose phosphate pathway
P value
4e-08
7e-02
1e-01
Enrichment Ratio
G
Pyrimidine metabolism
Purine metabolism
Pyruvate metabolism
One carbon pool by folate
Citrate cycle (TCA cycle)
-log10(p)
radi.vec
0.010
0.015
0.020
Pathway Impact
H
Metabolites
SUPM2 SLR-D vs SD
Downregulated
Not Significant
Upregulated
Hypoxanthine
Xanthosine
NMN
IMP
dATP
Inosine
PRPP
Uridine
AMP
N-Acetylglutamine
UMP
Succinic acid
-log10p-value
log2FC
I
SLR-DMSO
SLR-BMS
SLR-VCB1
Intensity
-5 -4 -3 -2 -1 0 1 2 3 4 5

Fig.6

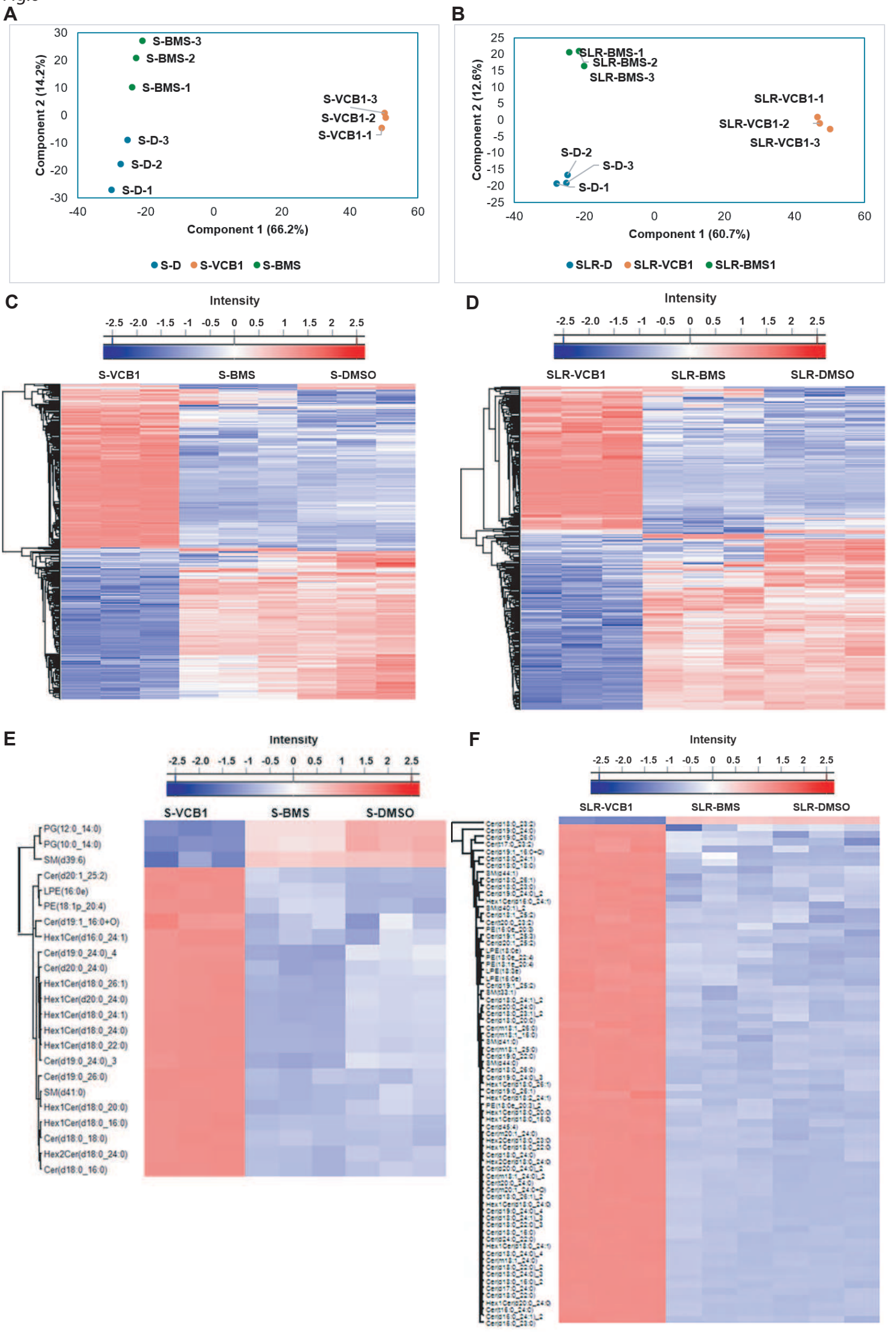
A
S-BMS-3
S-BMS-2
S-BMS-1
S-VCB1-3
S-VCB1-2
S-VCB1-1
S-D-3
S-D-2
S-D-1
Component 2 (14.2%)
Component 1 (66.2%)
S-D
S-VCB1
S-BMS
B
SLR-BMS-1
SLR-BMS-2
SLR-BMS-3
SLR-VCB1-1
SLR-VCB1-2
SLR-VCB1-3
S-D-2
S-D-3
S-D-1
Component 2 (12.6%)
Component 1 (60.7%)
SLR-D
SLR-VCB1
SLR-BMS1
C
Intensity
S-VCB1
S-BMS
S-DMSO
D
Intensity
SLR-VCB1
SLR-BMS
SLR-DMSO
E
Intensity
S-VCB1
S-BMS
S-DMSO
PG(12:0_14:0)
PG(10:0_14:0)
SM(d39:6)
Cer(d20:1_25:2)
LPE(16:0e)
PE(18:1p_20:4)
Cer(d19:1_16:0+O)
Hex1Cer(d16:0_24:1)
Cer(d19:0_24:0)_4
Cer(d20:0_24:0)
Hex1Cer(d18:0_26:1)
Hex1Cer(d20:0_24:0)
Hex1Cer(d18:0_24:1)
Hex1Cer(d18:0_24:0)
Hex1Cer(d18:0_22:0)
Cer(d19:0_24:0)_3
Cer(d19:0_26:0)
SM(d41:0)
Hex1Cer(d18:0_20:0)
Hex1Cer(d18:0_16:0)
Cer(d18:0_18:0)
Hex2Cer(d18:0_24:0)
Cer(d18:0_16:0)
F
Intensity
SLR-VCB1
SLR-BMS
SLR-DMSO

Fig.7

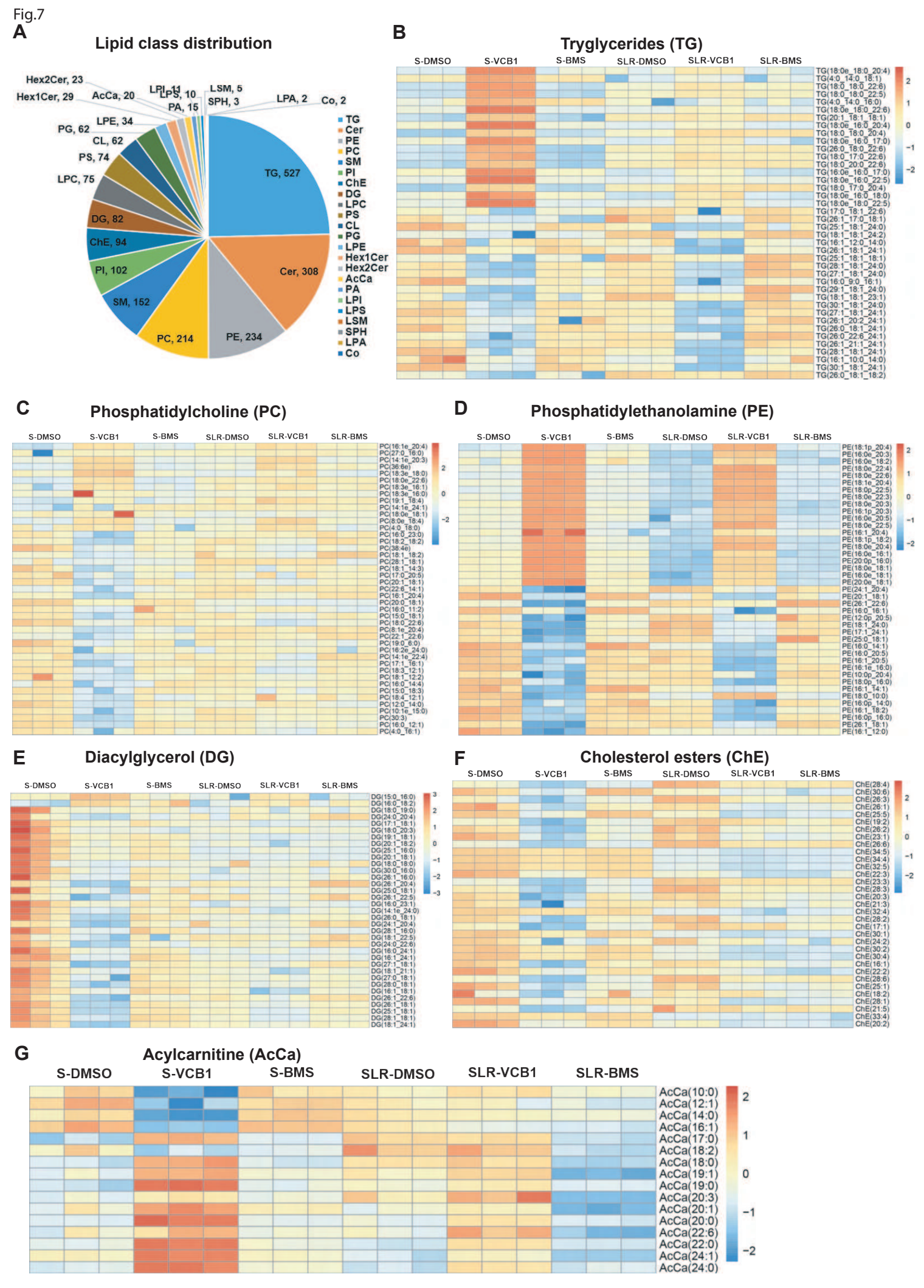
A
Lipid class distribution
Hex2Cer, 23
Hex1Cer, 29
AcCa, 20
LPI, 11
LPS, 10
PA, 15
LSM, 5
SPH, 3
LPA, 2
Co, 2
LPE, 34
PG, 62
CL, 62
PS, 74
LPC, 75
DG, 82
ChE, 94
PI, 102
SM, 152
PC, 214
PE, 234
Cer, 308
TG, 527
TG
Cer
PE
PC
SM
PI
ChE
DG
LPC
PS
CL
PG
LPE
Hex1Cer
Hex2Cer
AcCa
PA
LPI
LPS
LSM
SPH
LPA
Co
B
Tryglycerides (TG)
S-DMSO
S-VCB1
S-BMS
SLR-DMSO
SLR-VCB1
SLR-BMS
C
Phosphatidylcholine (PC)
D
Phosphatidylethanolamine (PE)
E
Diacylglycerol (DG)
F
Cholesterol esters (ChE)
G
Acylcarnitine (AcCa)
AcCa(10:0)
AcCa(12:1)
AcCa(14:0)
AcCa(16:1)
AcCa(17:0)
AcCa(18:2)
AcCa(18:0)
AcCa(19:1)
AcCa(19:0)
AcCa(20:3)
AcCa(20:1)
AcCa(20:0)
AcCa(22:6)
AcCa(22:0)
AcCa(24:1)
AcCa(24:0)

Fig. 8

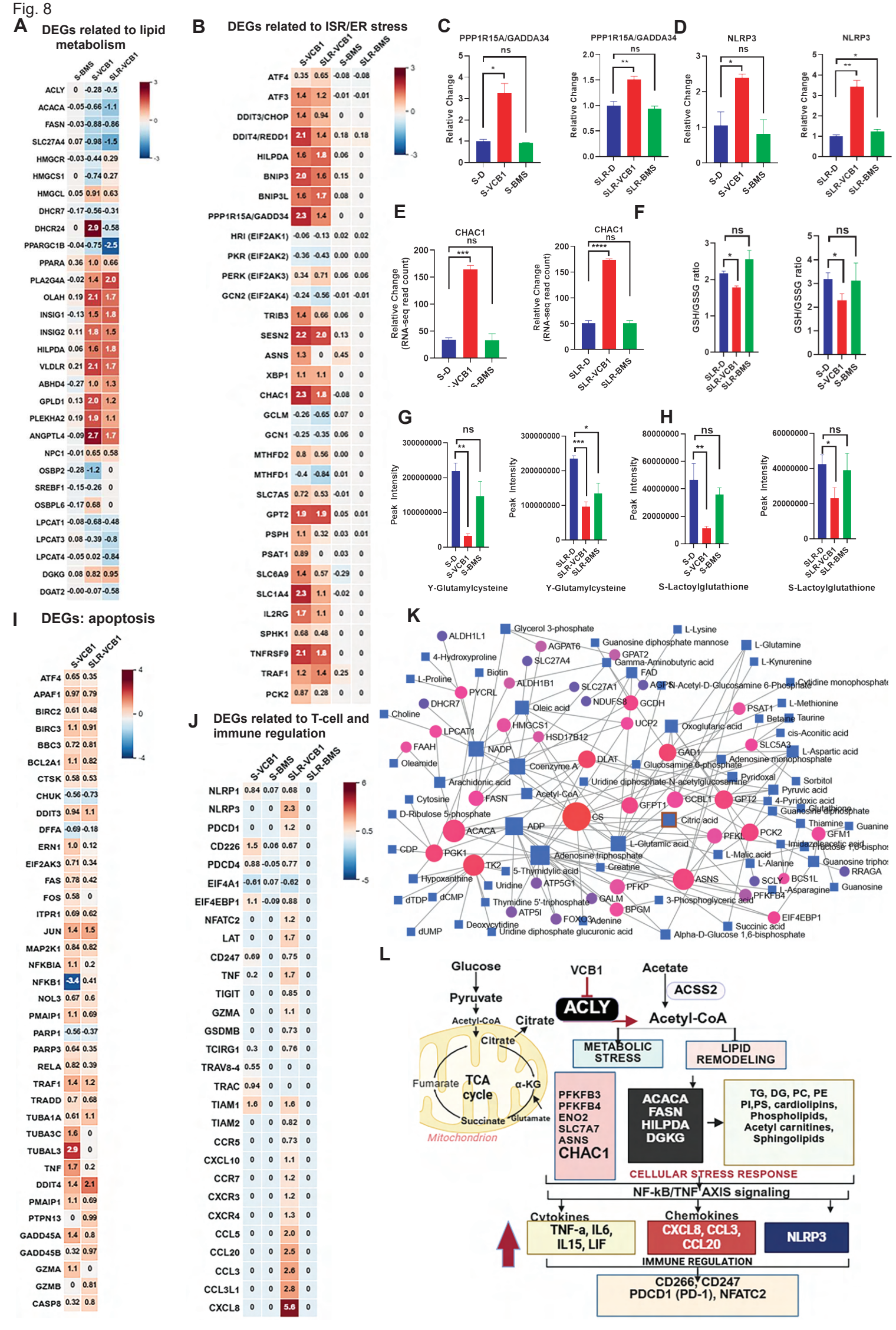
A
DEGs related to lipid metabolism
S-BMS S-VCB1 SLR-VCB1
ACLY 0 -0.28 -0.5
ACACA -0.05 -0.66 -1.1
FASN -0.03 -0.88 -0.86
SLC27A4 0.07 -0.98 -1.5
HMGCR -0.03 -0.44 0.29
HMGCS1 0 -0.74 0.27
HMGCL 0.05 0.91 0.63
DHCR7 -0.17 -0.56 -0.31
DHCR24 0 2.9 -0.58
PPARGC1B -0.04 -0.75 -2.5
PPARA 0.36 1.0 0.66
PLA2G4A -0.02 1.4 2.0
OLAH 0.19 2.1 1.7
INSIG1 -0.13 1.5 1.8
INSIG2 0.11 1.8 1.5
HILPDA 0.06 1.6 1.8
VLDLR 0.21 2.1 1.7
ABHD4 -0.27 1.0 1.3
GPLD1 0.13 2.0 1.2
PLEKHA2 0.19 1.9 1.1
ANGPTL4 -0.09 2.7 1.7
NPC1 -0.01 0.65 0.58
OSBP2 -0.28 -1.2 0
SREBF1 -0.15 -0.26 0
OSBPL6 -0.17 0.68 0
LPCAT1 -0.08 -0.68 -0.48
LPCAT3 0.08 -0.39 -0.8
LPCAT4 -0.05 0.02 -0.84
DGKG 0.08 0.82 0.95
DGAT2 -0.00 -0.07 -0.58
B
DEGs related to ISR/ER stress
S-VCB1 SLR-VCB1 S-BMS SLR-BMS
ATF4 0.35 0.65 -0.08 -0.08
ATF3 1.4 1.2 -0.01 -0.01
DDIT3/CHOP 1.4 0.94 0 0
DDIT4/REDD1 2.1 1.4 0.18 0.18
HILPDA 1.6 1.8 0.06 0
BNIP3 2.0 1.6 0.15 0
BNIP3L 1.6 1.7 0.08 0
PPP1R15A/GADD34 2.3 1.4 0 0
HRI (EIF2AK1) -0.06 -0.13 0.02 0.02
PKR (EIF2AK2) -0.36 -0.43 0.00 0.00
PERK (EIF2AK3) 0.34 0.71 0.06 0.06
GCN2 (EIF2AK4) -0.24 -0.56 -0.01 -0.01
TRIB3 1.4 0.66 0.06 0
SESN2 2.2 2.0 0.13 0
ASNS 1.3 0 0.45 0
XBP1 1.1 1.1 0 0
CHAC1 2.3 1.8 -0.08 0
GCLM -0.26 -0.65 0.07 0
GCN1 -0.25 -0.35 0.06 0
MTHFD2 0.8 0.56 0.00 0
MTHFD1 -0.4 -0.84 0.01 0
SLC7A5 0.72 0.53 -0.01 0
GPT2 1.9 1.9 0.05 0.01
PSPH 1.1 0.32 0.03 0.01
PSAT1 0.89 0 0.03 0
SLC6A9 1.4 0.57 -0.29 0
SLC1A4 2.3 1.1 -0.02 0
IL2RG 1.7 1.1 0 0
SPHK1 0.68 0.48 0 0
TNFRSF9 2.1 1.8 0 0
TRAF1 1.2 1.4 0.25 0
PCK2 0.87 0.28 0 0
C
PPP1R15A/GADDA34
Relative Change
S-D S-VCB1 S-BMS
D
PPP1R15A/GADDA34
NLRP3
SLR-D SLR-VCB1 SLR-BMS
E
CHAC1
Relative Change (RNA-seq read count)
F
GSH/GSSG ratio
G
Peak Intensity
Y-Glutamylcysteine
H
S-Lactoylglutathione
I
DEGs: apoptosis
S-VCB1 SLR-VCB1
ATF4 0.65 0.35
APAF1 0.97 0.79
BIRC2 0.61 0.48
BIRC3 1.1 0.91
BBC3 0.72 0.81
BCL2A1 1.1 0.82
CTSK 0.58 0.53
CHUK -0.56 -0.73
DDIT3 0.94 1.1
DFFA -0.69 -0.18
ERN1 1.0 0.12
EIF2AK3 0.71 0.34
FAS 0.78 0.42
FOS 0.58 0
ITPR1 0.69 0.62
JUN 1.4 1.5
MAP2K1 0.84 0.82
NFKBIA 1.1 0.2
NFKB1 -3.4 0.41
NOL3 0.67 0.6
PMAIP1 1.1 0.69
PARP1 -0.56 -0.37
PARP3 0.64 0.35
RELA 0.82 0.39
TRAF1 1.4 1.2
TRADD 0.7 0.68
TUBA1A 0.61 1.1
TUBA3C 1.6 0
TUBAL3 2.9 0
TNF 1.7 0.2
DDIT4 1.4 2.1
PMAIP1 1.1 0.69
PTPN13 0 0.99
GADD45A 1.4 0.8
GADD45B 0.32 0.97
GZMA 1.1 0
GZMB 0 0.81
CASP8 0.32 0.8
J
DEGs related to T-cell and immune regulation
S-VCB1 S-BMS SLR-VCB1 SLR-BMS
NLRP1 0.84 0.07 0.68 0
NLRP3 0 0 2.3 0
PDCD1 0 0 1.2 0
CD226 1.5 0.06 0.67 0
PDCD4 0.88 -0.05 0.77 0
EIF4A1 -0.61 0.07 -0.62 0
EIF4EBP1 1.1 -0.09 0.88 0
NFATC2 0 0 1.2 0
LAT 0 0 1.7 0
CD247 0.69 0 0.75 0
TNF 0.2 0 1.7 0
TIGIT 0 0 0.85 0
GZMA 0 0 1.1 0
GSDMB 0 0 0.73 0
TCIRG1 0.3 0 0.76 0
TRAV8-4 0.55 0 0 0
TRAC 0.94 0 0 0
TIAM1 1.6 0 1.6 0
TIAM2 0 0 0.82 0
CCR5 0 0 0.73 0
CXCL10 0 0 1.1 0
CCR7 0 0 1.2 0
CXCR3 0 0 1.2 0
CXCR4 0 0 1.3 0
CCL5 0 0 2.0 0
CCL20 0 0 2.5 0
CCL3 0 0 2.6 0
CCL3L1 0 0 2.8 0
CXCL8 0 0 5.6 0
K
Glycerol 3-phosphate
L-Lysine
ALDH1L1
AGPAT6
Guanosine diphosphate mannose
L-Glutamine
4-Hydroxyproline
SLC27A4
GPAT2
Gamma-Aminobutyric acid
L-Kynurenine
L-Proline
Biotin
FAD
ALDH1B1
SLC27A1
N-Acetyl-D-Glucosamine 6-Phosphate
Cytidine monophosphate
PYCRL
DHCR7
NDUFS8
GCDH
L-Methionine
Choline
Oleic acid
PSAT1
Betaine
Taurine
HMGCS1
UCP2
Oxoglutaric acid
LPCAT1
HSD17B12
cis-Aconitic acid
FAAH
NADP
GAD1
SLC5A3
L-Aspartic acid
Oleamide
Coenzyme A
DLAT
Glucosamine 6-phosphate
Adenosine monophosphate
Arachidonic acid
Uridine diphosphate-N-acetylglucosamine
Pyridoxal
Sorbitol
Cytosine
FASN
Acetyl-CoA
GFPT1
CCBL1
GPT2
Pyruvic acid
4-Pyridoxic acid
D-Ribulose 5-phosphate
CS
Citric acid
Guanosine diphosphate
ACACA
ADP
Thiamine
Guanine
PFKL
PCK2
GFM1
CDP
PGK1
L-Glutamic acid
Imidazoleacetic acid
Fructose 1,6-bisphos
Adenosine triphosphate
L-Malic acid
TK2
Creatine
L-Alanine
Guanosine tripho
RRAGA
Hypoxanthine
5-Thymidylic acid
Uridine
ATP5G1
ASNS
SCLY
BCS1L
L-Asparagine
Guanosine
dTDP
dCMP
PFKP
PFKFB4
Thymidine 5'-triphosphate
GALM
3-Phosphoglyceric acid
ATP5I
BPGM
FOXO3
Adenine
EIF4EBP1
dUMP
Deoxycytidine
Succinic acid
Uridine diphosphate glucuronic acid
Alpha-D-Glucose 1,6-bisphosphate
L
Glucose
Pyruvate
Acetyl-CoA
Citrate
VCB1
ACLY
Acetate
ACSS2
Acetyl-CoA
METABOLIC STRESS
LIPID REMODELING
Fumarate
TCA cycle
α-KG
Succinate
Glutamate
Mitochondrion
PFKFB3
PFKFB4
ENO2
SLC7A7
ASNS
CHAC1
ACACA
FASN
HILPDA
DGKG
TG, DG, PC, PE
PI,PS, cardiolipins,
Phospholipids,
Acetyl carnitines,
Sphingolipids
CELLULAR STRESS RESPONSE
NF-kB/TNF AXIS signaling
Cytokines
Chemokines
TNF-a, IL6, IL15, LIF
CXCL8, CCL3, CCL20
NLRP3
IMMUNE REGULATION
CD266, CD247
PDCD1 (PD-1), NFATC2

Fig.9

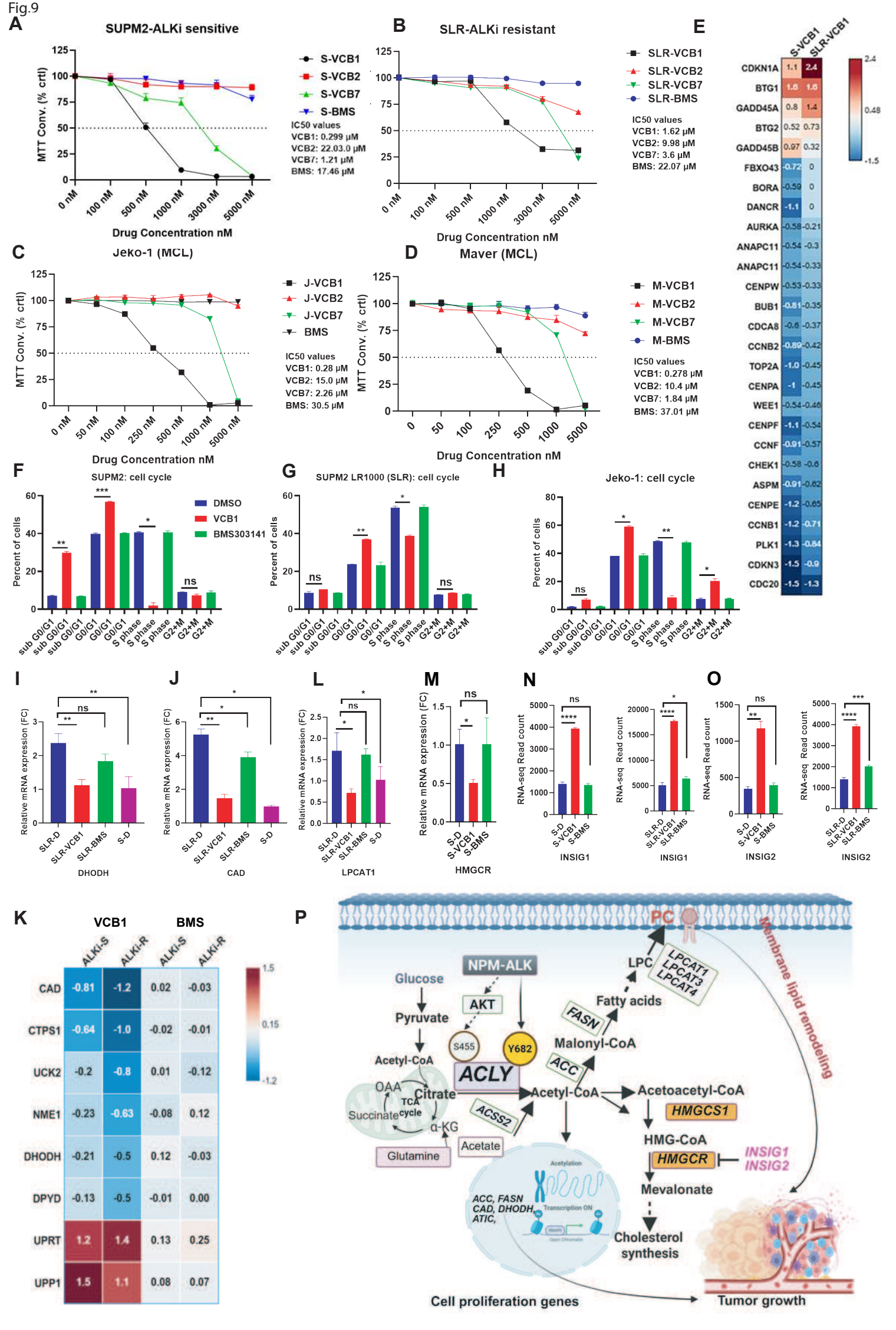
A
SUPM2-ALKi sensitive
MTT Conv. (% crtl)
Drug Concentration nM
S-VCB1
S-VCB2
S-VCB7
S-BMS
IC50 values
VCB1: 0.299 μM
VCB2: 22.03.0 μM
VCB7: 1.21 μM
BMS: 17.46 μM
B
SLR-ALKi resistant
SLR-VCB1
SLR-VCB2
SLR-VCB7
SLR-BMS
IC50 values
VCB1: 1.62 μM
VCB2: 9.98 μM
VCB7: 3.6 μM
BMS: 22.07 μM
C
Jeko-1 (MCL)
J-VCB1
J-VCB2
J-VCB7
BMS
IC50 values
VCB1: 0.28 μM
VCB2: 15.0 μM
VCB7: 2.26 μM
BMS: 30.5 μM
D
Maver (MCL)
M-VCB1
M-VCB2
M-VCB7
M-BMS
IC50 values
VCB1: 0.278 μM
VCB2: 10.4 μM
VCB7: 1.84 μM
BMS: 37.01 μM
E
S-VCB1
SLR-VCB1
CDKN1A
BTG1
GADD45A
BTG2
GADD45B
FBXO43
BORA
DANCR
AURKA
ANAPC11
ANAPC11
CENPW
BUB1
CDCA8
CCNB2
TOP2A
CENPA
WEE1
CENPF
CCNF
CHEK1
ASPM
CENPE
CCNB1
PLK1
CDKN3
CDC20
F
SUPM2: cell cycle
DMSO
VCB1
BMS303141
Percent of cells
G
SUPM2 LR1000 (SLR): cell cycle
H
Jeko-1: cell cycle
I
Relative mRNA expression (FC)
SLR-D
SLR-VCB1
SLR-BMS
S-D
DHODH
J
CAD
L
LPCAT1
M
HMGCR
N
RNA-seq Read count
INSIG1
O
INSIG2
K
VCB1
BMS
ALKi-S
ALKi-R
CAD
CTPS1
UCK2
NME1
DHODH
DPYD
UPRT
UPP1
P
Glucose
Pyruvate
Acetyl-CoA
OAA
Citrate
TCA cycle
Succinate
α-KG
Glutamine
Acetate
NPM-ALK
AKT
S455
Y682
ACLY
ACSS2
Acetyl-CoA
Acetoacetyl-CoA
HMGCS1
HMG-CoA
HMGCR
INSIG1
INSIG2
Mevalonate
Cholesterol synthesis
Malonyl-CoA
ACC
FASN
Fatty acids
LPC
LPCAT1
LPCAT3
LPCAT4
PC
Membrane lipid remodeling
ACC, FASN
CAD, DHODH,
ATIC,
Acetylation
Transcription ON
Cell proliferation genes
Tumor growth

Supplementary Fig.1

A

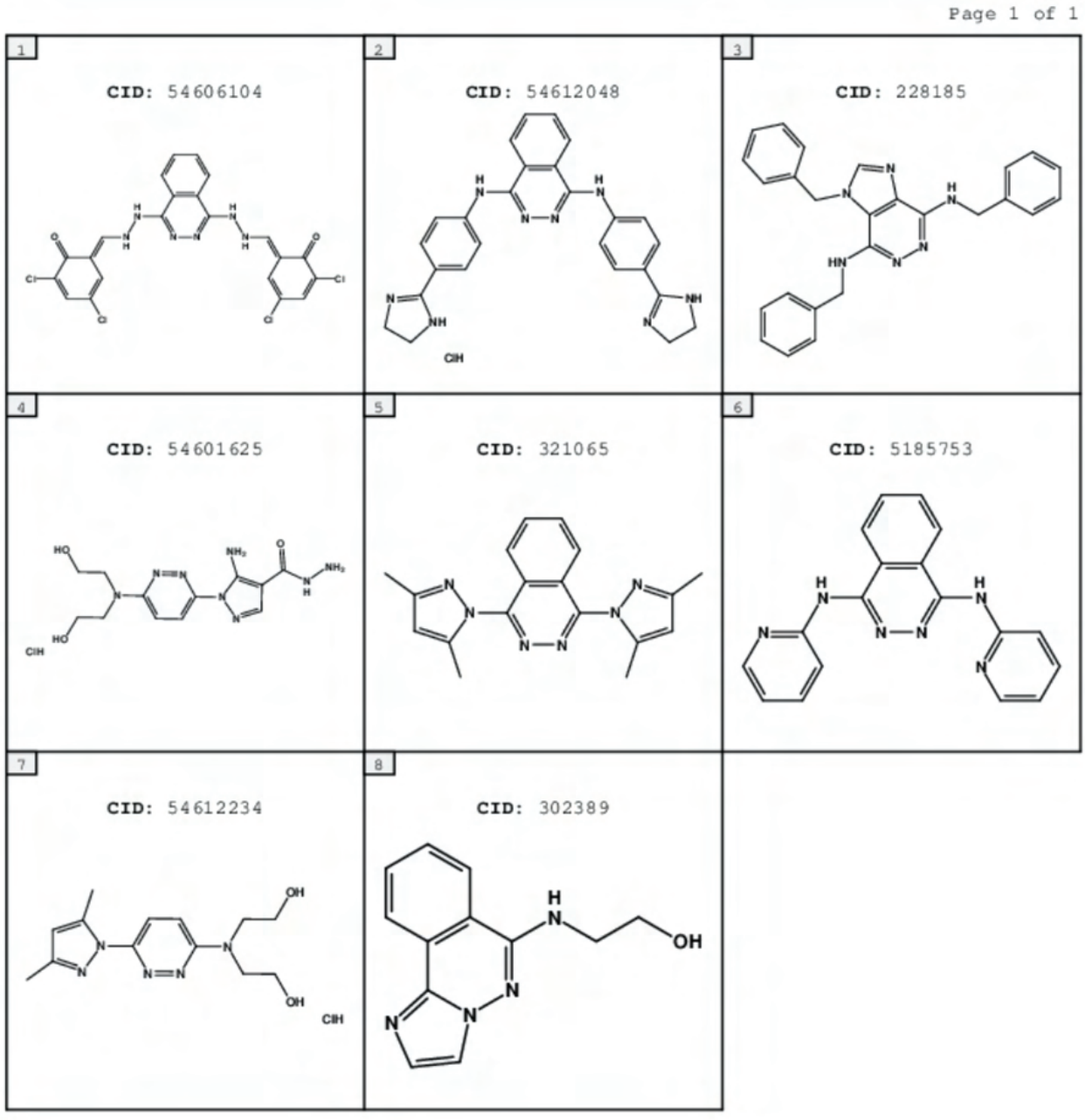

Supplementary Fig. 2

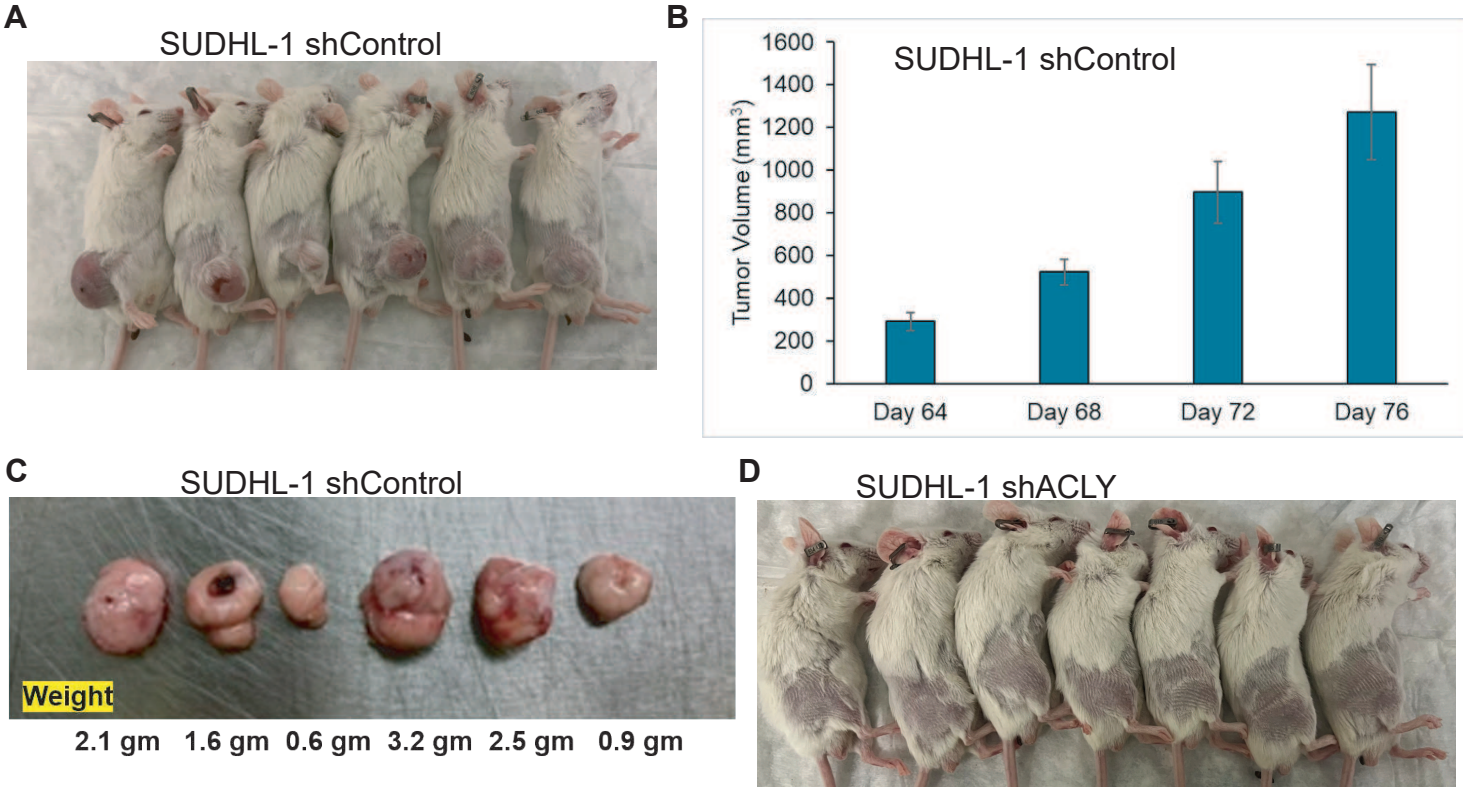

Supplementary Fig.3

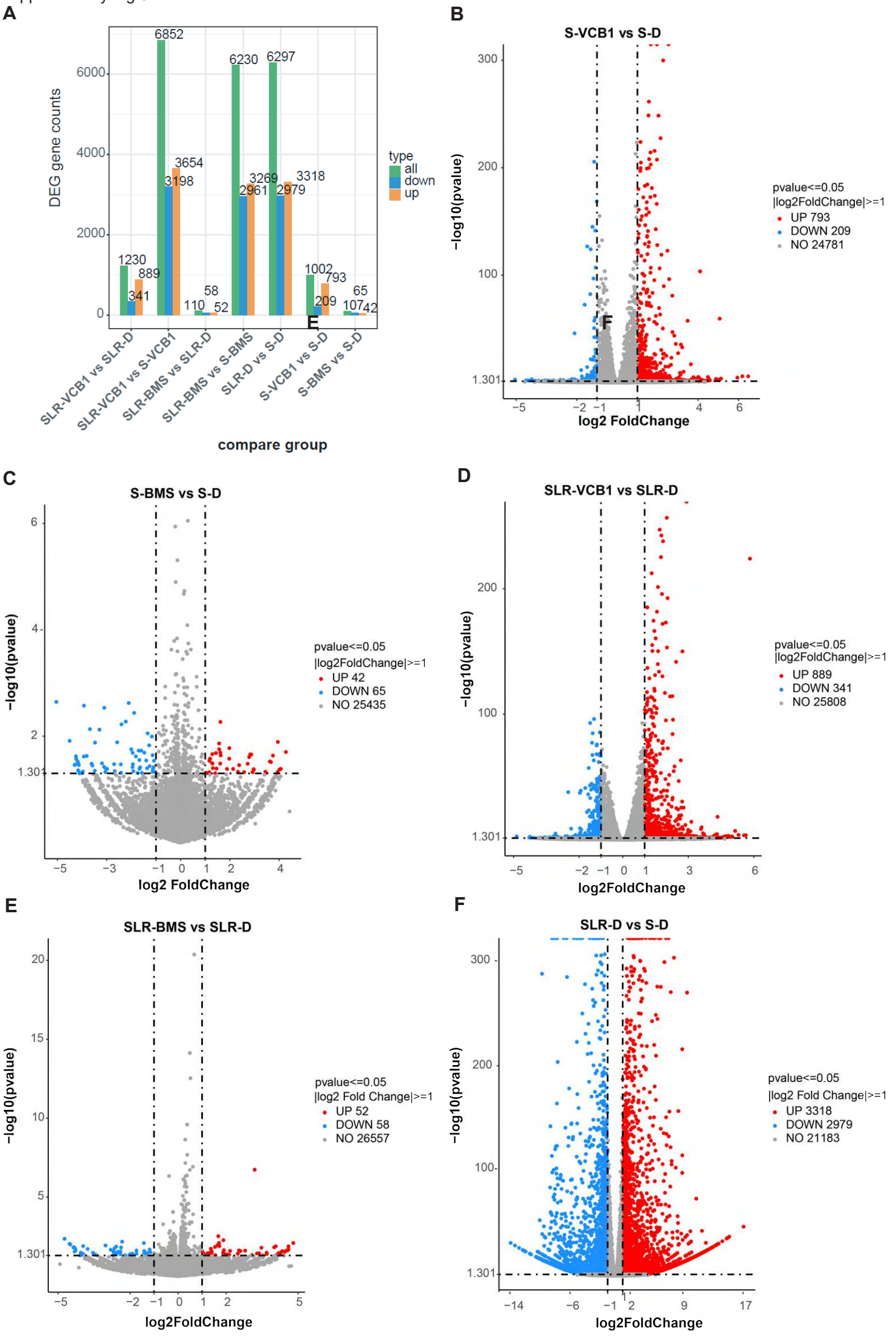

Supplementary Fig. 4

Based on the common DEGs in SLR-VCB1 and S-VCB1 (log2 FC + 1.0 up or - 1.0 down)

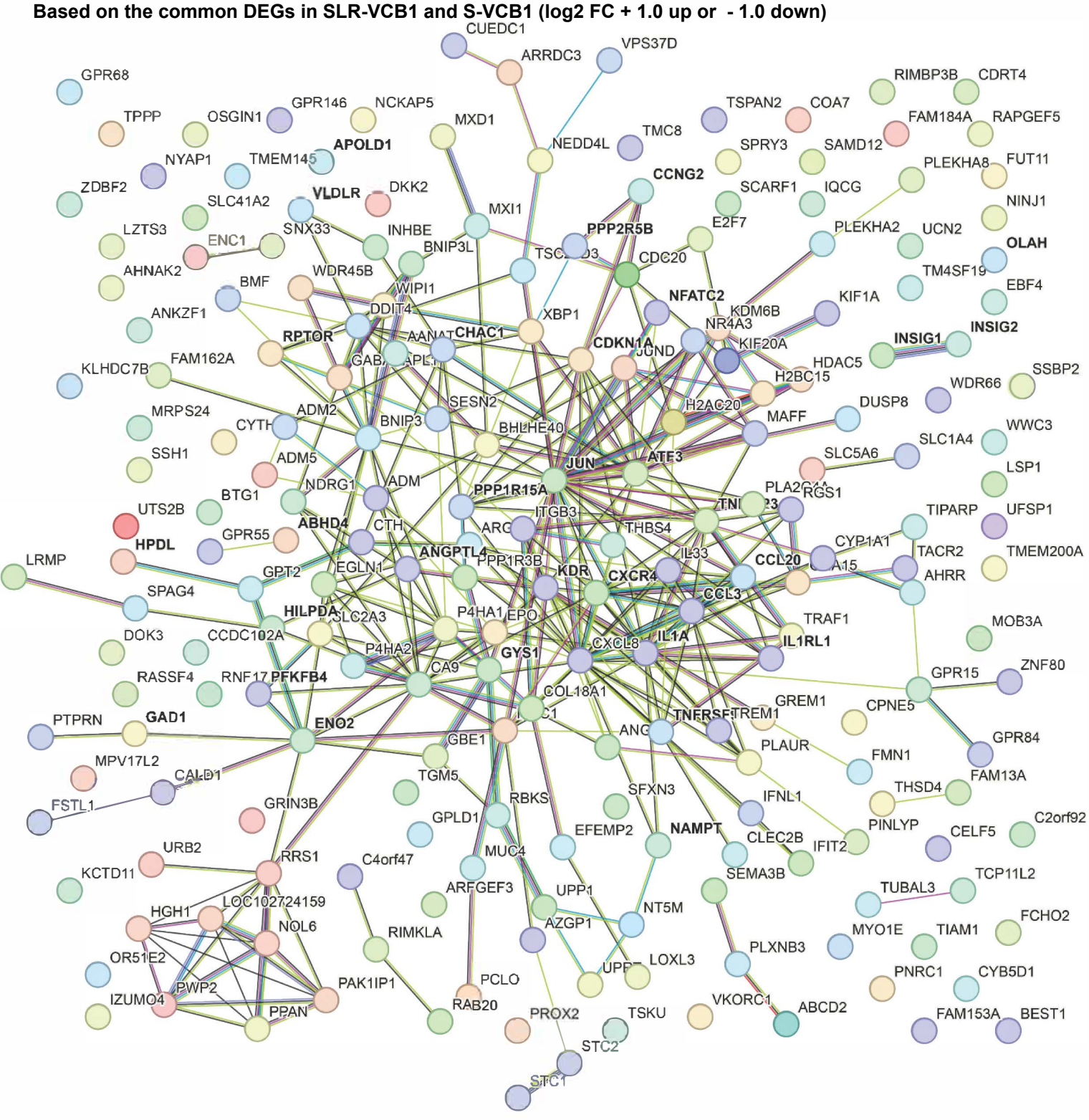

Supplementary Fig. 5

A **Metabolic pathways DEGs**

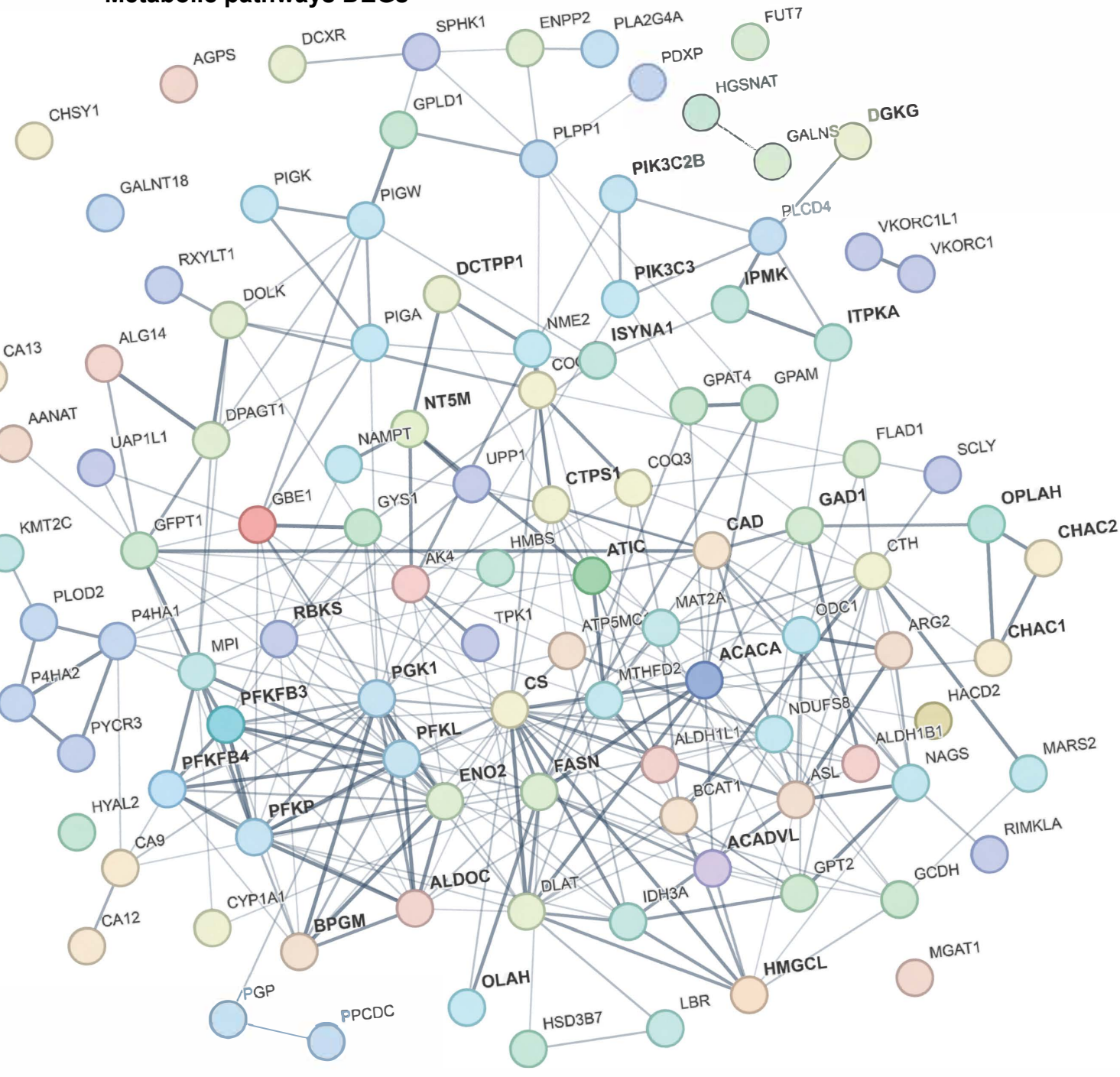

Supplementery Fig. 5

B **DEGs in cellular response to lipid (Based on Biological process-Gene Ontology)**

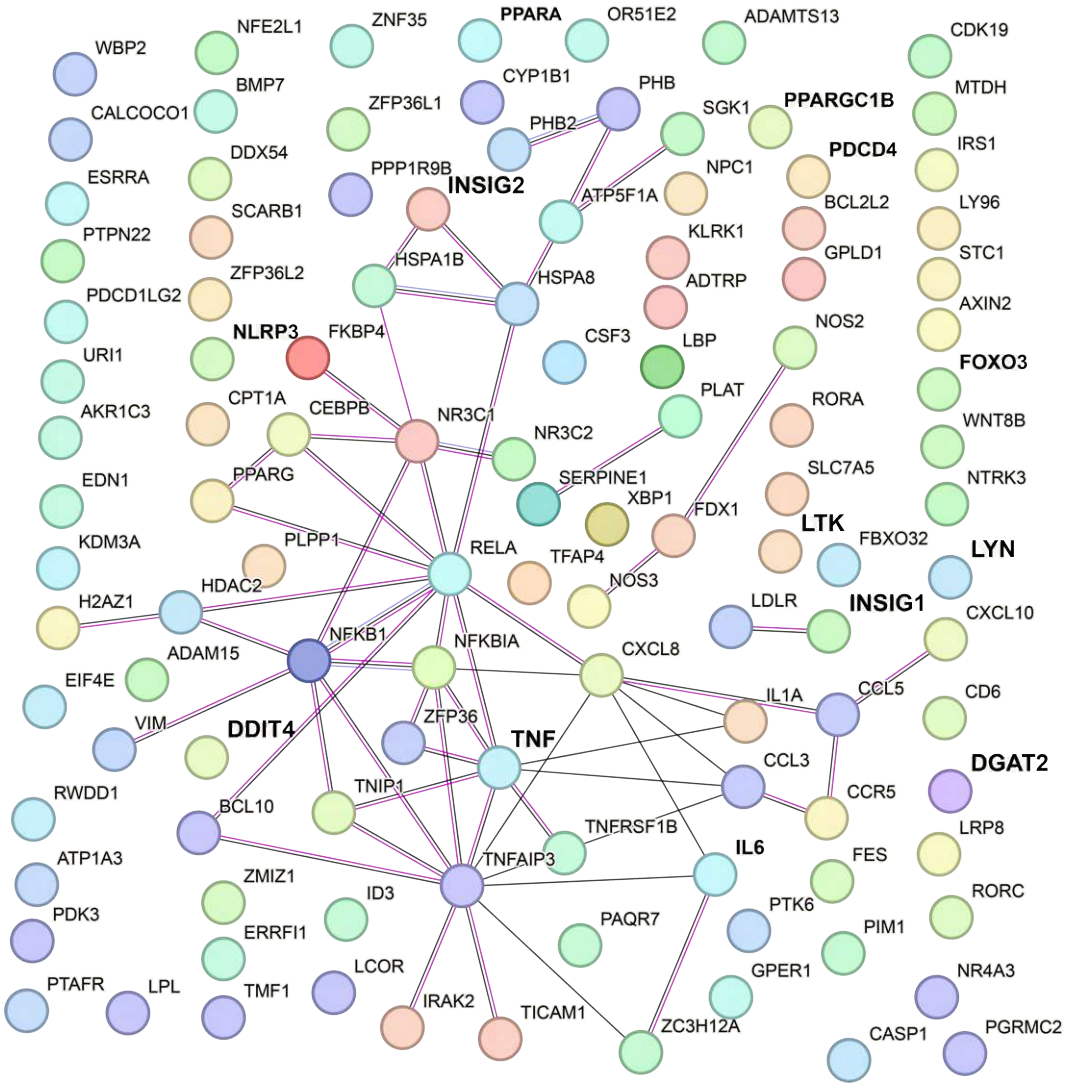

C

TNF signaling pathway

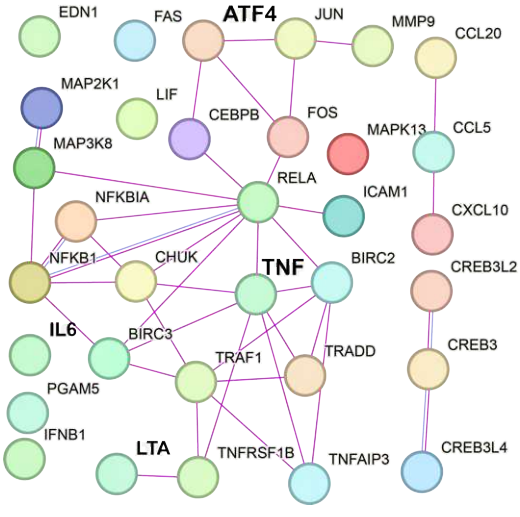

D

HIF1 signaling pathway

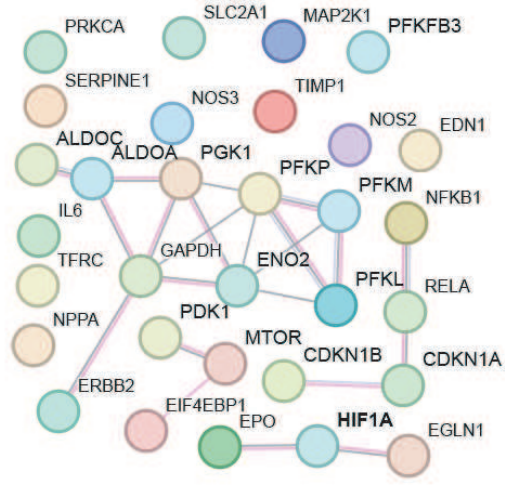

Supplementary Fig. 6

A

Based on the common DEGs in SLR-VCB1 and S-VCB1 (log2 FC + / - 0.5 up and down)

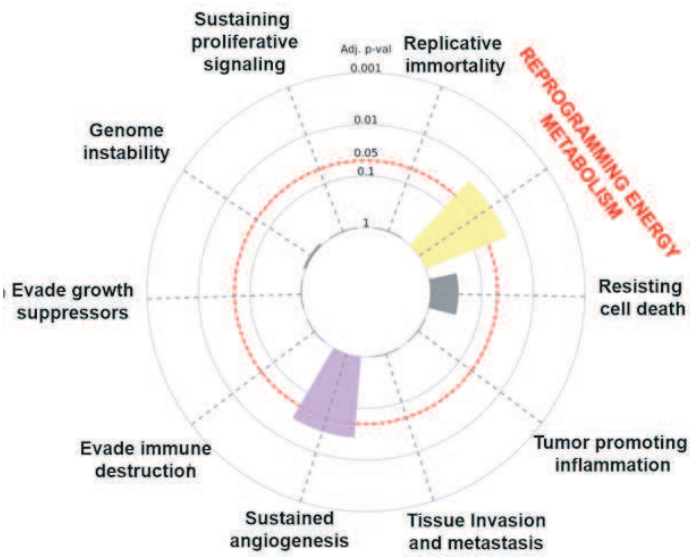

B

Hallmark DEGs enrichment

Cancer hallmark	Overlap	P-value	Adjusted P-value
REPROGRAMMING ENERGY METABOLISM	**30/155**	**0.00207**	**0.02069**
SUSTAINED ANGIOGENESIS	**23/117**	**0.00532**	**0.0266**
Resisting cell death	57/423	0.08556	0.2852
Genome instability	22/178	0.35426	0.88564
Sustaining proliferative signaling	74/655	0.5068	0.95973
Evading growth suppressors	43/407	0.6967	0.95973
Replicative immortality	Sep-94	0.74511	0.95973
Tumor-promoting inflammation	6/66	0.76778	0.95973
Tissue invasion and metastasis	57/624	0.96543	0.96543
Evading immune destruction	7/106	0.96173	0.96543

REPROGRAMMING ENERGY METABOLISM
FASN, PDK1, BNIP3, TPI1, PFKP, PGK1, PGM1, PRPS1, CS, IDH3A, MYC, GYS1, CDKN1B, ACACA NDUFS7, DLAT, ALDOA, PFKFB3, SUCLA2, MAP2K1, NDUFS8, ENO2, ACACA, MTOR, ALDOC, SLC16A3, PFKL, BPGM, FH, RPTOR, HIF1A

SUSTAINED ANGIOGENESIS
KDR, FES, IL1A, PDGFRA, TGFBR2, MYC, CAV1, IL10, RRAS, EPAS1, SDC4, ITGB3, SPHK1, MET, TGFBR1, MAP2K1, MTOR, VEGFB, VEGFA, CXCR4, PLAUR, CXCL8, HIF1A

C

Based on the common DEGs in SLR-VCB1 and S-VCB1 (log2 FC + 0.5 up regulated)

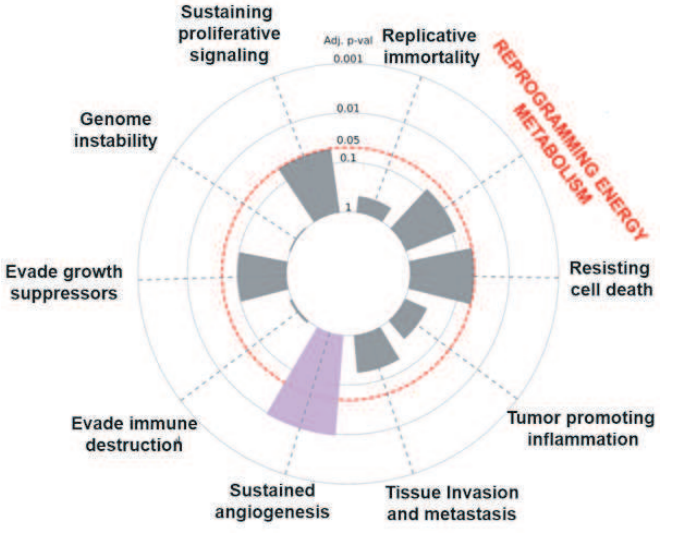

D

Hallmark DEGs enrichment

Cancer Hallmark	Overlap	P-value	Adjusted P-value
Sustained Angiogenesis	**17/117**	**0.00094**	**0.00939**
Sustaining Proliferative Signaling	**56/655**	**0.01024**	**0.05109**
Resisting Cell Death	**38/423**	**0.01533**	**0.05109**
Reprogramming Energy Metabolism	**16/155**	**0.03291**	**0.08227**
Evading Growth Suppressors	34/407	0.05124	0.10247
Tissue Invasion and Metastasis	47/624	0.10404	0.1734
Tumor-Promoting Inflammation	Jun-66	0.22932	0.3276
Replicative Immortality	Jul-94	0.3723	0.46537
Evading Immune Destruction	5/106	0.79954	0.88838
Genome Instability	7/178	0.93354	0.93354

REPROGRAMMING ENERGY METABOLISM
ALDOA, PFKFB3, PDK1, BNIP3, MAP2K1, TPI1, ENO2, RPTOR, PFKP, CDKN1B, SLC16A3, PGK1, GYS1, PGM1, ALDOC, PFI

SUSTAINED ANGIOGENESIS
SPHK1, KDR, MET, TGFBR1, FES, PLAUR, MAP2K1, CXCL8, RRAS, IL1A, EPAS1, SDC4, ITGB3, TGFBR2, VEGFB, VEGFA, CXCR4

E

Based on the common DEGs in SLR-VCB1 and S-VCB1 (log2 FC - 0.5 down regulated)

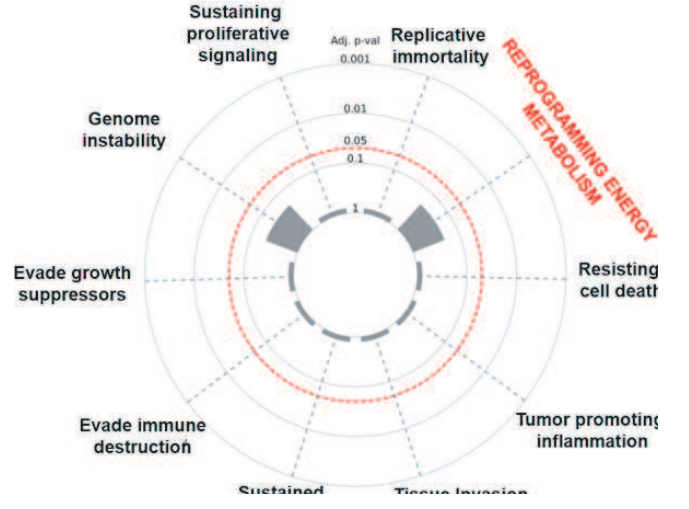

F

Hallmark DEGs enrichment

Cancer Hallmark	Overlap	P-value	Adjusted P-value
Reprogramming Energy Metabolism	**13/155**	**0.03483**	**0.20886**
Genome Instability	**14/178**	**0.04641**	**0.20886**
Resisting Cell Death	15/423	0.91193	1
Sustaining Proliferative Signaling	14/655	0.99989	1
Evading Growth Suppressors	7/407	0.99974	1
Evading Immune Destruction	2/106	0.96528	1
Sustained Angiogenesis	2/117	0.97805	1
Tissue Invasion and Metastasis	6/624	1	1
Tumor-Promoting Inflammation	0/1	—	1
Replicative Immortality	Jan-94	0.99014	1

Supplementary Fig. 7

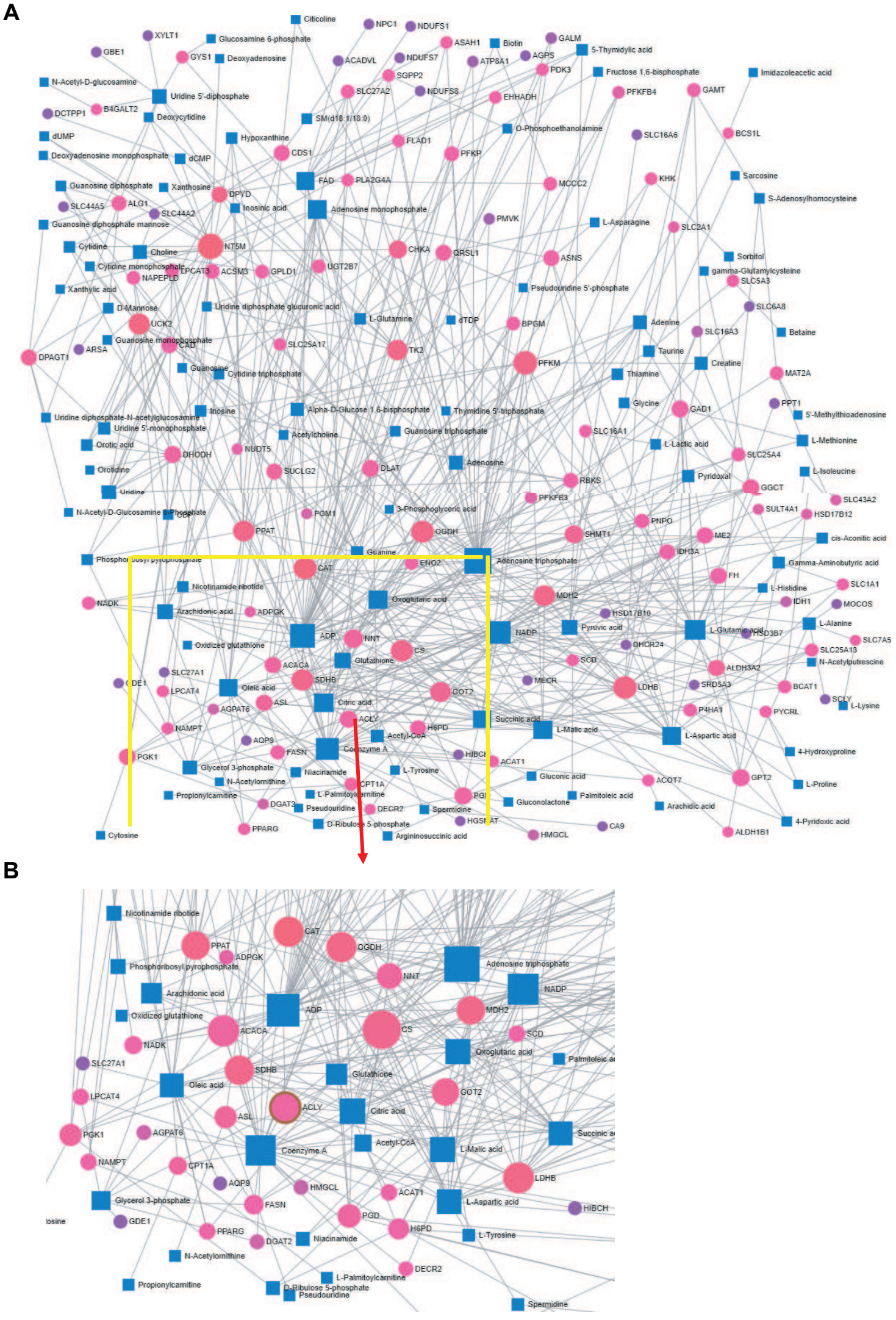

Table-1 Common DEGs in TKI sensitive and resistant cell lines

Gene symbol	S-VCB1 (log_2 FC)	SLR-VCB1 (log_2 FC)	Metabolic function
PFKFB4	2.73	2	Glycolysis; regulates fructose-2,6-bisphosphate and metabolic stress adaptation
PFKL	0.89	0.9	Glycolysis; rate-limiting phosphofructokinase activity
GPAT4	0.52	0.84	Glycerolipid/triglyceride synthesis
GAD1	1.15	1.25	Glutamate → GABA metabolism
PPARGC1B	−0.751	−2.497	PGC-1β; mitochondrial oxidative metabolism, fatty-acid oxidation and energy metabolism
ABCD2	−1.388	−1.239	Peroxisomal fatty-acid transport and β-oxidation
ALDH1B1	−0.683	−1.237	Aldehyde metabolism; mitochondrial metabolic/detoxification function
ACACA	−0.660	−1.149	Acetyl-CoA → malonyl-CoA; rate-limiting de novo fatty-acid synthesis
SCLY	−0.953	−1.128	Selenocysteine/selenium recycling; antioxidant metabolism
BCS1L	−0.586	−1.121	Mitochondrial complex III assembly and oxidative phosphorylation
FASN	−0.884	−0.859	De novo fatty-acid synthesis; converts acetyl-CoA/malonyl-CoA into fatty acids
CS	−0.543	−0.739	TCA cycle; citrate production from acetyl-CoA and oxaloacetate
BPGM	−0.906	−0.802	Glycolytic intermediate/2,3-BPG metabolism
AGPS	−0.506	−0.642	Ether phospholipid/plasmalogen biosynthesis
HACD2	−0.525	−0.597	Fatty-acid elongation; very-long-chain fatty-acid synthesis
PYCR3	−0.599	−0.539	Proline biosynthesis; NAD(P)H-dependent reduction of P5C
DLAT	−0.503	−0.599	Pyruvate dehydrogenase complex; pyruvate → acetyl-CoA
NDUFS8	−0.514	−0.508	Mitochondrial complex I/electron transport
COQ2	−0.563	−0.631	Coenzyme Q biosynthesis; mitochondrial respiration

Supplementary Table-1 Metabolic function DEGs specific in S-VCB1 condition

Gene symbol	S-VCB1 (log2 FC)	Metabolic function
ANGPTL4	2.68	Lipid metabolism; fatty-acid uptake/lipolysis regulation
SESN2	2.19	Metabolic stress; AMPK/mTOR regulation
DDIT4	2.12	Metabolic adaptation; mTOR inhibition
VLDLR	2.07	Lipoprotein and fatty-acid uptake
BNIP3	1.97	Mitochondrial metabolism; mitophagy
GPT2	1.91	Glutamate/glutamine and amino-acid metabolism
PLEKHA2	1.91	Phosphoinositide/lipid-associated metabolic signaling
HILPDA	1.57	Lipid storage; triglyceride metabolism
ASNS	1.25	Asparagine and amino-acid biosynthesis
UPRT	1.23	Pyrimidine salvage/nucleotide metabolism
PRELID2	1.19	Mitochondrial phospholipid transport
APOL1	1.17	Lipid transport/metabolism
AK4	1.17	Mitochondrial energy/nucleotide metabolism
SLC2A3	1.15	Glucose uptake
SLC2A13	1.14	Glucose/metabolite transport
EIF4EBP1	1.13	Nutrient/mTOR-dependent metabolic regulation
VKORC1	1.11	Vitamin K metabolism
RPTOR	1.08	mTORC1 nutrient/energy sensing
PSPH	1.06	Serine biosynthesis
NBR2	1.03	Energy stress/AMPK signaling
ABHD4	1.02	Phospholipid metabolism
PGK1	0.91	Glycolysis; ATP generation
PCK2	0.87	Mitochondrial gluconeogenesis/anaplerosis
MAP1LC3B	0.87	Autophagy/metabolic recycling
APOL2	0.85	Lipid transport/metabolism
FOXO3	0.84	Energy metabolism/autophagy regulation
PSAT1	0.82	Serine biosynthesis
SLC25A29	0.81	Mitochondrial amino-acid transport
ABCA2	0.81	Cholesterol/lipid transport
SIRT5	0.81	Mitochondrial metabolic regulation
ISYNA1	0.79	Inositol biosynthesis
ACSF3	0.7	Mitochondrial acyl-CoA metabolism
RRAGA	0.7	Amino-acid sensing/mTORC1 regulation
SLC27A1	0.69	Long-chain fatty-acid uptake
DIO2	0.59	Thyroid hormone metabolism
PTER	0.56	Phospholipid metabolism
NR1H3	0.56	Cholesterol/lipid metabolic regulation
SLC5A3	0.56	Myo-inositol transport
HSD17B12	0.55	Fatty-acid elongation/lipid metabolism

Gene symbol	S-VCB1 (log2 FC)	Metabolic function
TK2	0.54	Mitochondrial nucleotide metabolism
GALM	0.54	Galactose metabolism
ATG9A	0.54	Autophagy/metabolic recycling
FLCN	0.53	Energy and nutrient sensing
GDPD5	0.52	Glycerophospholipid metabolism
STARD4	0.52	Intracellular cholesterol transport
GLTP	0.52	Glycosphingolipid transport
NMRK1	0.52	NAD salvage metabolism
GFPT1	0.51	Hexosamine biosynthetic pathway
SCD	0.51	stearoyl-CoA desaturase
COA7	−1.135	Mitochondrial respiratory-chain function
SLC27A4	−0.984	Fatty-acid uptake/activation
CNR1	−0.879	Endocannabinoid signaling/metabolic regulation
HMGCS1	−0.737	Mevalonate/cholesterol biosynthesis
FAAH	−0.697	Endocannabinoid/fatty-acid metabolism
LPCAT1	−0.679	Phospholipid remodeling
GFM1	−0.636	Mitochondrial translation/respiratory metabolism
GPAT2	−0.625	Glycerolipid/triglyceride biosynthesis
DHCR7	−0.565	Cholesterol biosynthesis
MSTO1	−0.535	Mitochondrial dynamics/metabolic function
UCP2	−0.531	Mitochondrial metabolism and uncoupling
ATP5ME	−0.526	Oxidative phosphorylation
HACD2	−0.525	Fatty-acid elongation
ATP5MC1	−0.521	Oxidative phosphorylation/ATP synthesis

Supplementary Table-2 Metabolic function DEGs specific in SLR-VCB1 condition

Gene symbol	SLR-VCB1 (log2 FC)	Metabolic function
NT5M	−1.883	Mitochondrial 5′-nucleotidase; nucleotide metabolism
SLC43A2	−1.665	Large neutral amino-acid transporter
EEF2KMT	−1.641	Links protein synthesis to metabolic regulation
SULT4A1	−1.622	Sulfotransferase; small molecule/steroid metabolism
BCO2	−1.379	β-carotene/carotenoid metabolism
CHAC2	−1.373	Glutathione/cysteine metabolism
FXN	−1.348	Fe-S cluster metabolism and oxidative phosphorylation
ATP8A1	−1.327	Phospholipid membrane metabolism
NDUFAF4	−1.312	Mitochondrial complex I assembly
SLC16A14	−1.226	Monocarboxylate/metabolite transport
CAD	−1.196	De novo pyrimidine biosynthesis
DCTPP1	−1.152	dNTP metabolism
PGAM5	−1.140	Mitochondrial metabolism/stress signaling
SGPP2	−1.127	Sphingolipid metabolism
SLC16A9	−1.127	Monocarboxylate/carnitine-associated metabolite transport
FLAD1	−1.122	FAD/flavin metabolism
HSD17B8	−0.910	Steroid/lipid metabolism
CPT1A	−0.899	Mitochondrial fatty-acid β-oxidation
CLUH	−0.885	Mitochondrial protein/lipid metabolic homeostasis
NUDT5	−0.881	Nucleoside diphosphate/ADP-ribose metabolism
ALG1	−0.879	N-glycan/glycan metabolism
NT5DC3	−0.877	Nucleotide metabolism
ACSM3	−0.859	Fatty-acid activation to acyl-CoA
GOT2	−0.857	Amino-acid/TCA coupling
MTHFD1	−0.848	Folate-mediated one-carbon metabolism
LPCAT4	−0.837	Phospholipid remodeling
MAT2A	−0.826	Methionine/SAM and methylation metabolism
UCK2	−0.804	Pyrimidine salvage
LPCAT3	−0.803	Phospholipid remodeling
PPAT	−0.795	De novo purine biosynthesis
IDH3A	−0.779	TCA cycle; α-ketoglutarate production
LDHB	−0.765	Lactate ↔ pyruvate metabolism
CDS1	−0.755	CDP-diacylglycerol/phospholipid biosynthesis
OGDH	−0.749	TCA cycle
PFKM	−0.748	Glycolytic phosphofructokinase
ACAT1	−0.739	Acetyl-CoA, ketogenesis/cholesterol metabolism
FH	−0.734	TCA cycle
NNT	−0.726	Mitochondrial NADPH generation
MECR	−0.706	Mitochondrial fatty-acid synthesis
PTDSS1	−0.700	Phosphatidylserine biosynthesis
MYLIP	−0.690	Cholesterol homeostasis

NADK	−0.682	NADP(H) production/redox metabolism
GDE1	−0.680	Glycerophospholipid/phosphoinositide metabolism
ALDH3A2	−0.659	Fatty-aldehyde oxidation
ASAH1	−0.658	Ceramide/sphingolipid metabolism
ABCD3	−0.652	Peroxisomal fatty-acid transport
SLC27A2	−0.650	Long-chain fatty-acid transport/activation
ARV1	−0.641	Sterol/lipid homeostasis
NDUFAF6	−0.636	Complex I assembly
HSD17B10	−0.632	Mitochondrial β-oxidation
NDUFAF8	−0.630	Complex I assembly
KHK	−0.629	Fructose phosphorylation
EHHADH	−0.626	Peroxisomal fatty-acid β-oxidation
GAMT	−0.626	Creatine biosynthesis
MCAT	−0.625	Mitochondrial fatty-acid synthesis
DECR2	−0.624	Peroxisomal fatty-acid β-oxidation
NDUFS7	−0.624	Mitochondrial complex I
SUCLG2	−0.618	TCA cycle/substrate-level phosphorylation
NAPEPLD	−0.616	N-acyl-phosphatidylethanolamine/endocannabinoid metabolism
SHMT1	−0.612	Serine/one-carbon metabolism
SFXN4	−0.608	Mitochondrial metabolite/one-carbon transport
HACD3	−0.604	Fatty-acid elongation
CAT	−0.604	H_2O_2 detoxification/redox metabolism
ACOT7	−0.602	Acyl-CoA regulation
SDHB	−0.596	TCA cycle/complex II
CHKA	−0.591	Phosphatidylcholine synthesis
PMVK	−0.588	Mevalonate pathway
FECH	−0.587	Heme biosynthesis
DGAT2	−0.582	Triacylglycerol synthesis
DHCR24	−0.579	Cholesterol biosynthesis
IDH1	−0.574	Cytosolic isocitrate metabolism/NADPH
GPAM	−0.570	Glycerolipid synthesis
NEU3	−0.566	Ganglioside/sialic-acid and lipid metabolism
MDH2	−0.559	TCA metabolism
SLC25A17	−0.559	Peroxisomal CoA/ATP transport
NDUFS1	−0.557	Mitochondrial complex I
PPT1	−0.550	Lysosomal lipid/protein depalmitoylation
HSD3B7	−0.545	Bile acid/cholesterol metabolism
HIBCH	−0.543	Valine catabolism
MCCC2	−0.543	Branched-chain amino-acid metabolism
PGD	−0.541	Pentose-phosphate pathway/NADPH
SLC25A13	−0.540	Mitochondrial aspartate/glutamate transport
ME2	−0.537	NADPH generation from malate

PDP2	−0.534	Pyruvate dehydrogenase activation
QRSL1	−0.521	Glutamine-dependent purine biosynthesis
MIOS	−0.520	GATOR2/mTORC1 nutrient sensing
KLF16	−0.520	Metabolic/mitochondrial transcriptional regulation
STARD7	−0.518	Mitochondrial phospholipid transport
PAQR3	−0.518	Metabolic signaling/PI3K pathways
HTATIP2	−0.518	Mitochondrial/lipid metabolic stress regulation
RETSAT	−0.517	Retinol metabolism
PNPO	−0.515	Vitamin B6 metabolism
NIPA2	−0.514	Magnesium/metabolic regulation
PPARG	−0.513	Lipid storage/utilization regulation
LDAH	−0.513	Lipid droplet/lipid storage regulation
XYLT1	−0.512	Glycosaminoglycan biosynthesis
B4GALT2	−0.511	Glycan/galactose metabolism
DPAGT1	−0.510	N-glycosylation/carbohydrate metabolism
GGCT	−0.509	Glutathione metabolism
DHODH	−0.505	De novo pyrimidine synthesis
ACLY	−0.502	Citrate → cytosolic acetyl-CoA; central carbon/lipid metabolism
SCAP	−0.502	SREBP activation; cholesterol/lipid homeostasis
STOML2	−0.502	Mitochondrial membrane/metabolic signaling
DPYD	−0.500	Pyrimidine catabolism
CHAC1	1.77	Glutathione degradation/oxidative-stress response
GLUL	1.5	Glutamine synthesis/nitrogen metabolism
PDK1	0.99	Pyruvate dehydrogenase inhibition/metabolic reprogramming
DMGDH	0.93	Glycine/dimethylglycine metabolism
SLC2A1	0.9	Glucose uptake
SLC16A13	0.9	Monocarboxylate/lipid metabolic regulation
AMPD3	0.9	AMP/purine metabolism
STARD10	0.89	Intracellular lipid handling/signaling
MSRB1	0.88	Methionine/oxidative-redox metabolism
TCN2	0.85	Vitamin B12 transport/cofactor homeostasis
DNAJB9	0.84	ER proteostasis/metabolic stress
PFKFB3	0.82	Glycolytic flux/glucose metabolism
GK	0.81	Glucose phosphorylation
SLC16A3	0.81	Lactate export/glycolytic metabolism
AMPD2	0.8	Purine nucleotide metabolism
SOD2	0.79	Mitochondrial ROS detoxification
PDK3	0.76	Suppresses pyruvate oxidation; glycolytic adaptation
CRELD2	0.76	ER stress/metabolic adaptation
SLC25A36	0.74	Mitochondrial nucleotide transport
ERO1A	0.74	ER redox metabolism
EDEM1	0.74	ER-associated degradation

APOBR	0.72	Lipid uptake/metabolism
NAGK	0.72	Amino-sugar/amino-acid metabolism
OPLAH	0.71	Glutathione degradation
PGRMC2	0.69	Lipid/cholesterol-associated metabolism
FUCA1	0.5256	Glycan/carbohydrate degradation
GGCX	0.5248	Vitamin-K-dependent metabolic processing
C11orf54	0.5246	pH/metabolic homeostasis
CLN8	0.5236	ER–lysosome lipid trafficking
ARF4	0.5224	Membrane/lipid trafficking
TG	0.522	Thyroid hormone precursor metabolism
IP6K1	0.5215	Inositol phosphate/energy signaling
SLC24A1	0.521	Ion/metabolic homeostasis
LYPLAL1	0.5209	Lipid/lysophospholipid metabolism
CARS	0.5205	Cysteine/amino-acid utilization
AIFM2	0.5197	Redox metabolism/lipid-peroxidation regulation
BLOC1S6	0.5193	Endosomal/lysosomal trafficking; indirect lipid relevance
UGP2	0.5188	UDP-glucose/carbohydrate metabolism
ADAM19	0.5178	Extracellular protein processing; indirect metabolic relevance
GPR137	0.5172	Lysosomal/nutrient-dependent metabolism
SMAP2	0.5165	Membrane/lipid trafficking
SLC26A11	0.5113	Anion/pH homeostasis affecting metabolism
CACNA1C	0.5107	Calcium signaling influencing mitochondrial metabolism
ENTPD7	0.51	Extracellular nucleotide metabolism
PQLC1	0.5089	Lysosomal amino-acid transport
OGT	0.5088	Nutrient-sensitive glucose/hexosamine signaling
BCAT1	0.5086	Branched-chain amino-acid catabolism
PPM1K	0.5084	BCAA catabolism/BCKDH regulation
LACTB	0.5069	Mitochondrial/lipid metabolism
BCKDK	0.5068	BCAA oxidation regulation
HSPA13	0.5048	Metabolic/proteostasis stress
OSBPL5	0.5037	Oxysterol/lipid transport
TK1	0.5025	Thymidine salvage/dTTP production
RAB3A	0.5024	Vesicular trafficking; indirect metabolic relevance
AK2	0.5006	Mitochondrial ATP/ADP/AMP homeostasis